UNIVERSIDAD NACIONAL AUTÓNOMA DE MÉXICO
PROGRAMA DE MAESTRÍA Y DOCTORADO EN INGENIERÍA
INSTITUTO DE ENERGÍAS RENOVABLES

ANÁLISIS BIDIMENSIONAL DE UN ÁLABE DE AEROGENERADOR USANDO MÉTODOS NUMÉRICOS

TESIS

QUE PARA OPTAR POR EL GRADO DE:

MAESTRO EN INGENIERÍA (ENERGÍA)

P R E S E N T A:

JORGE EDUARDO CHAGOYA BELLO

TUTOR PRINCIPAL:

DR. EDUARDO RAMOS MORA - IER

COMITÉ TUTORIAL:

DR. SERGIO CUEVAS GARCÍA - IER
DR. MARTÍN SALINAS VÁZQUEZ - II
DR. RAFAEL CAMPOS AMEZCUA - IER
DR. OSVALDO RODRÍGUEZ HERNÁNDEZ - IER

TEMIXCO, MOR., JUNIO 2016

JURADO ASIGNADO:

Presidente: Dr. Sergio Cuevas García

Secretario: Dr. Martín Salinas Vázquez

Vocal: Dr. Eduardo Ramos Mora

1^{er} Suplente: Dr. Rafael Campos Amezcua

2^{do} Suplente: Dr. Osvaldo Rodríguez Hernández

Lugar donde se realizó la tesis:

INSTITUTO DE ENERGÍAS RENOVABLES - UNAM

DIRECTOR DE TESIS:

Dr. Eduardo Ramos Mora

_____

FIRMA

Contents

Abstract

The purpose of this work is to contribute to the research and development of the domestic design and manufacturing of horizontal wind turbine blades. The analysis consists on the description of the flow around two dimensional airfoils which in turn represents equally spaced sections along a hypothetical 3D blade, while keeping an optimum angle of attack. The study for each section was done by solving mass and momentum conservation equations by means of a finite volume method over a Cartesian domain. The study was conducted using a structured grid, with velocity central difference approximation and an implicit time integration scheme. The pressure coupling method used was SIMPLE-Consistent algorithm. The scope of the study is limited to a compressible laminar flow using low Reynolds numbers and validation scenarios that include the simulation of flow over circular and square shapes with mesh independence analysis and comparison with XFOIL pane-based results.

The blade sectioning method propose starting by computing a twist along the blade span, an optimal angle of attack computation, besides a domain size and parameter selection. A result monitor was developed in order to gauge main outputs of interest such as pressure and tangent velocities on surface as in the whole field. The results obtained show consistency and certain level of confidence, and they vary depending upon section location along the hypothetical blade, which meant to set a variation on apparent input velocity as well as on surface extension of each section. Blade section method gives a good approximation of results in practice and may be improved –though not considering 3D effects– and compare results to experimental data. As a final recommendation this code is not completely accurate or reliable to design or manufacture a wind turbine blade; instead, consider the methodolgy as a base work or starting point that may be used for pedagogical purposes.

Chapter 1

Introduction to wind turbine blade theory and literature review.

1.1 Fundamental concepts.

Among the various renewable energy sources, wind energy is one of the most promising and the fastest growing alternative energy technologies. Wind turbine design is an optimization problem where the solution should be found under a set of design constraint and specific targets[12]. However, many authors have proposed different objectives, methods of resolution, constraints, algorithms, tools and models in their quest to optimize the performance of wind turbines. In the past, some authors have reviewed the optimization algorithms, energy policies, economics, and environmental impacts of wind turbines but numerous researchers have proposed different optimization methodologies as well as resolution strategies. In the present chapter we will briefly review some of the most important concepts and ideas.

1.1.1 Introduction to wind energy production.

In this section, a brief summary of the fundamental concepts used in wind energy utilization is given. For comprehensive and authoritative reviews on the subject the reader is referred to Burton et al.[12], consider the kinetic energy E of air in motion contained in a volume V moving with velocity v_w as shown in figure 1.1, the available power per unit volume is then:

$$P = \frac{E}{t} = \frac{1}{2} A \varrho {v_w}^3 \tag{1.1}$$

where v_w the free wind speed. The previous expression indicates that the power density, i.e. the power per unit of normal area A to the wind direction from which the wind is blowing, can be defined as $P' = \frac{1}{2}\varrho_1 \cdot {v_w}^3$. Given that the power is proportional to the cube of the wind velocity, a small change in wind speed will have huge effect on power production.

1.1.2 Maximum theoretical efficiency.

The primary component of a wind turbine is the rotor (energy converter) which transforms the kinetic energy contained in the moving air into mechanical energy. The mechanical energy will be transformed into electrical energy by other means involving electrical generators specifically designed for this application. This last step of energy transformation is out of the scope of this work. The ultimate goal of a wind turbine is to continuously convert all the kinetic energy of the wind into mechanical energy of the blades but unfortunately, mass conservation prevents this possibility. Consequently, there must be an optimum reduction of the wind speed, to extract the maximum amount of energy.

Figure 1.2 depicts the situation, where streamlines, speed and pressure are shown as functions of position. The subscript *1* represents the far upstream rotor plane. Notice that $v_1 = v_w$. Subscript *3* indicates a position far downstream, and subscript *2* indicates the rotor plane position. The elementary momentum method establishes that the flow velocity past the position of the wind generator where energy is extracted, is reduced, from v_1 to v_3, while the cross sectional area is widening from A_1 to A_3 because of the mass flow balance. The pressure p_1 experiences an increase near the upstream side of the rotor to reach a maximum p^+. Then the pressure features a sudden drop Δp for a minimum p^-. Far downstream the pressure rises to $p_3 = p_1$.

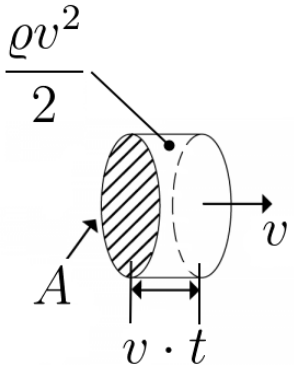

Figure 1.1. Sketch of the kinetic energy density $E = \frac{\varrho v^2}{2}$ contained in the volume $V = Avt$.

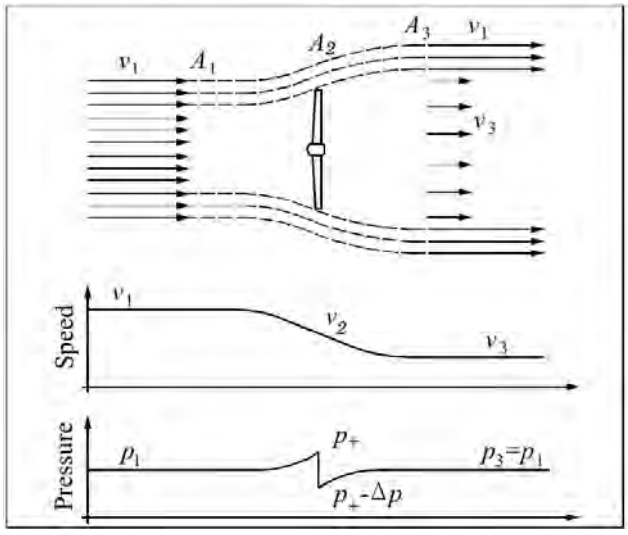

Figure 1.2. An Energy Extracting Actuator Disc and Stream-tube, and the effect over velocity and pressure.

The mass flow rate is the same everywhere along the stream-tube. Using the notation of

figure 1.2, the mass conservation reads as follows:

$$\varrho A_1 v_1 = \varrho A_2 v_2 = \varrho A_3 v_3.$$

The change in momentum of the wind at the position of the wind turbine can be obtained by applying Bernoulli's equation from the upstream position to the front of the wing turbine and from the back of the wind turbine to the downstream position. In symbols, as seen in the following equations:

$$p_2^+ - p_1 = \tfrac{1}{2}\varrho(v_1^2 - v_2^2) \qquad \text{and} \qquad p_2^- - p_3 = \tfrac{1}{2}\varrho(v_3^2 - v_2^2).$$

Assuming that the ambient atmospheric pressure is the same far away from the turbine, $p_1 = p_3 = p_\infty$. Subtracting the two previous expressions, we get:

$$p_2^+ - p_2^- = \tfrac{1}{2}\varrho(v_1^2 - v_3^2).$$

Using this expression, the force on the wind generator can be calculated,

$$F = (p_2^+ - p_2^-)A_2 = \tfrac{1}{2}\varrho A_2(v_1^2 - v_3^2). \tag{1.2}$$

The air passing through the rotor plane undergoes a change in velocity $\Delta v = v_1 - v_3$, then the force can be calculated as:

$$F = \dot{m}\,\Delta v = \varrho A_2 v_2(v_1 - v_3) \tag{1.3}$$

From equations (1.2) and (1.3), we get:

$$v_2 = \frac{v_1 + v_3}{2}. \tag{1.4}$$

We proceed to calculate the power extracted from the wind. The power is defined as $P = F\,v_2$, thus, using equation (1.2) for the force, the power is:

$$P = \tfrac{1}{2}\varrho A_2 v_2(v_1^2 - v_3^2).$$

Considering the conservation of momentum, the mechanical power output at the rotor can be deduced. The velocity v_2 can be eliminated from the previous equation with expression (1.4), and recalling v_1 and v_3 are the upward and downward velocities:

$$P_m = \tfrac{1}{4}\varrho A_2(v_1 + v_3)(v_1^2 - v_3^2)$$

where P_m is the mechanical power output, which is equal to the power of the rotor P. Arranging the terms, this expression can be specified directly as a function of the velocity ratio in terms of v_3/v_1:

$$P_m = \tfrac{1}{4}\varrho A_2 \left(1 + \frac{v_3}{v_1}\right)\left(1 - \left(\frac{v_3}{v_1}\right)^2\right) v_1^3.$$

It is convenient, to scale the power with the available wind power contained in the wind defined by $P_0 = \varrho A_2 v_1^3$, i.e. the power of the undisturbed free-air stream which flows through the cross sectional area A_2. The scaled power, also called power coefficient, denoted by C_P is,

$$C_P = \frac{P_m}{P_0} = \frac{1}{2}\left(1 + \frac{v_3}{v_1}\right)\left(1 - \left(\frac{v_3}{v_1}\right)^2\right) \tag{1.5}$$

P_m/P_0, is defined as the ratio of power extracted over the power available.

The result of equation 1.5 can be expressed in terms of axial flow induction factor $a = (v_1 - v_2)/v_1$. This variable represents the normalized velocity reduction as the wind meets the turbine. Note that the net stream-wise velocity at the rotor plane may be expressed as $v_2 = v_1(1 - a)$, so according to 1.4,

$$\frac{v_2}{v_1} = (1 - a) \qquad \text{and,} \qquad \frac{v_3}{v_1} = 1 - 2a \tag{1.6}$$

Then, from 1.5, the power coefficient is:

$$C_P = 4a(1 - a)^2$$

The maximum C_P may be obtained by taking

$$\frac{dC_P}{da} = 4(1 - a)3(1 - 3a) = 0$$

from where $a = v_3/v_1 = 1/3$, thus substituting in 1.5:

$$C_P^{max} = \tfrac{16}{27} = 0.593$$

The Betz theory assumes a constant linear velocity, but in practice, any rotational forces such as wake rotation, turbulence caused by drag or vortex shedding (tip losses) will further reduce the maximum efficiency. Efficiency losses are generally reduced by (1) avoiding low

tip speed ratios, (2) specialized tip geometries, (3) selecting aerofoils which have a high lift to drag ratio and others. The last of which will be analysed further on in this study.

Rotor designs also undergo an accumulation of minor losses resulting from blade shape simplification (simplified blades means reduced manufacturing cost). Lastly, total wind turbine power delivery will suffer losses due to many causes beyond the rotor, such as drive train and generator efficiency losses, and losses at the distribution grid.

The power actually captured by the wind turbine rotor, P_R, is a fraction of the available power P, defined by the rotor coefficient of performance, C_{PR}, which is essentially a type of power conversion efficiency $C_{PR} = P_R/P$. In other words, $P_R = C_{PR}\frac{\varrho}{2}v_w^3 A$. The aerodynamic rotor theory yields the interrelation between the geometrical shape of a real rotor configuration and its power characteristics. Power coefficient curves must be calculated for different pitch angles at certain r/R locations along the tip speed ratio variation[21].

1.2 Basic HAWT blade dynamic considerations.

The selected blade element for this work analysis corresponds to a typical Horizontal Axis Wind Turbine or *HAWT* configuration. Even though there are other power production devices such as VAWT (Vertical Axis Wind Turbine), which doesn't require to be aligned in regards to the wind's direction, the superiority of HAWT for large power production is well documented. The qualities of HAWT is mainly based on the following characteristics[21]:

(1) In propeller designs, rotor speed and power output can be controlled by pitching the rotor blades about their longitudinal axis, also useful as protection against over-speed and extreme wind (gusts), (2) the rotor blade shape can be aerodynamically optimised and it has been proven that it will achieve its highest efficiency when aerodynamic lift is maximum, and (3) the technological lead in the development of propeller design is a decisive factor.

1.2.1 Tip speed ratio.

The tip-speed ratio (λ), is a parameter used to describe the performance of the entire wind turbine, the influence of which extends far beyond rotor aerodynamics and is defined by aspects such as efficiency, torque, mechanical stress, aerodynamics and noise. These aspects should be considered in selecting the appropriate λ (see table 1.1).

$$\lambda = \frac{tangential\ velocity\ of\ the\ rotor\ blade\ tip}{free\ wind\ speed} = \frac{u_{tip}}{v_w} = \frac{\omega R}{v_w} \tag{1.7}$$

where ω is the angular speed and R is the radius of the wind turbine. Higher values of λ do not necessarily mean a higher C_{PR}. Wind turbines must be designed with optimal λ

to extract as much power out of the wind as possible. Common design values are 5-8 for 3-bladed rotors and 9-10 for 2-bladed rotors[21].

Table 1.1. Tip speed ratio design considerations[38].

TSR(λ)	Low($1-2$)	High(>10)
Torque ($T(r)$)	High	Low
Efficiency (C_P)	Decrease below 5(wake)	Insignificant increase after 8
Aerodynamic Stress	Decreases	Increases(linearly with ω)
Solidity	Increases(multiple blades)	Decreases significantly
Blade profile	Large	Significantly narrow
Aerodynamics	Simple	Critical
Noise	Increases to 10^6 order	

In table 1.1 several variables are cited, such as torque $T(r)$(power P transmitted by a shaft at ω tangential velocity), efficiency C_P (converted energy from the wind), aerodynamic stress (stress over the blade coming from aerodynamic loads), solidity (total blade planform area/rotor swept area), blade profile (airfoil size), aerodynamics (airfoil shape), noise (sound pressure level). Some of these concepts will be explained. Each blade element, a division of the blade into a number of independent sections along its span, will have a variable of incident velocity, i.e., the relative wind velocity, also known as apparent wind velocity.

1.2.2 Wind velocity components.

The axial freestream velocity $\vec{V}_w$ and the tangential speed $\vec{U}(r)$ at the radius of the corresponding blade cross-section are combined to form a resultant flow velocity $\vec{W}$, and according to the velocity components on figure 1.3, may be expressed as the vectorial difference, $\vec{W} = \vec{V}_w - \vec{U}(r)$.

The airfoil cross-section at radius r is set at a local blade pitch angle β with respect to the rotor plane of rotation. Together with airfoil chord line, it forms the local aerodynamic *angle of attack* α. In aerodynamics, the angle of attack α is an aerodynamic parameter and the blade pitch angle β is a design parameter[21].

Where,
r =radius,
$\vec{W}$ =relative (apparent) velocity,
$\vec{U}(r)$ =local blade velocity at r,
$\vec{V}_w$ =wind velocity,
R_T =total reaction over aerofoil,
α =angle of attack (AOA),
γ =angle of relative wind to rotor axis or incidence angle,
φ =angle of relative wind to rotor plane,
β =pitch angle of the blade (control).

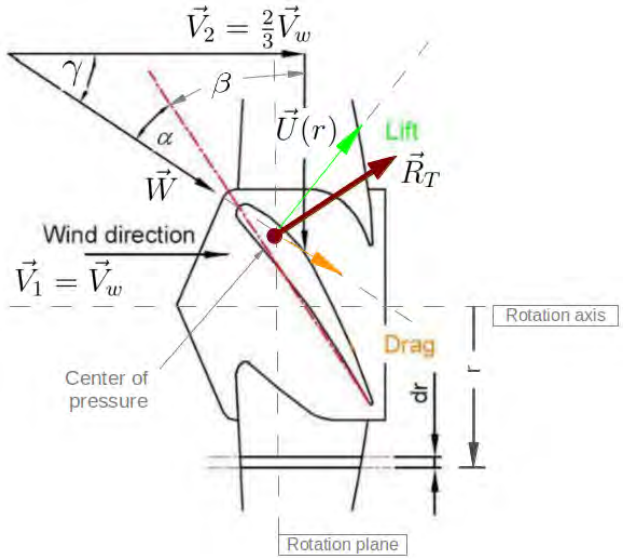

Figure 1.3. Wind velocity components at a blade element.

A simple example will provide us with information that will be useful to discuss the results of chapter 4. For simulation purposes, we shall consider $W = 1.0\ [ms^{-1}]$, and a chord= 1.0 $[m]$, both at the tip. We will also choose $\lambda = 5$ as a good practice design parameter for 3 blades.

(1) Consider that ideally we want to reduce free wind velocity to $V = \frac{2}{3}V_w$ at the rotor plane stage. Then upstream velocity, according to figure 1.3, should be $V_w = V_1 = W_R/\sqrt{\lambda^2 + \frac{4}{9}}$. For the present example $V_1 = 0.1982\ [ms^{-1}]$. According to equation 1.7, we can estimate $u_1 = \lambda V_1 = 0.991\ [ms^{-1}]$; thus $\omega = 0.0991(\frac{1}{2\pi})$, in $[rev \cdot s^{-1}]$, if $R = 10$; i.e. 10 times the chord.

(2) We easily may obtain the following geometrical parameters for any r location[19]:

$$\gamma_r = arctan\ \frac{3\lambda}{2R} r$$

$$\varphi_r = arctan\ \frac{2R}{3\lambda}\frac{1}{r}$$

$$\beta_r = arctan\ \varphi_r - \alpha_D$$

i.e., for any variation on α, the pitch control angle will vary $\beta_r = 90° - (\alpha + \gamma_r)$. For the example, at $r = R$: $\gamma_r = 82.4°$, $\varphi_r = 7.6°$ and $\beta_r = -7.4°$. We may conclude that the blade should twist its incidence and rotation plane along the length.

1.2.3 Twist along the blade's span.

The twist angle is defined as the angle between the local airfoil chord and 70% of the rotor radius or that at the blade tip (see figure 1.4). In order to achieve the optimum reduction in flow velocity over the entire length, the blades have to be twisted along it, considering effective (which is the relative or apparent component) flow velocity changes from the root to the tip. The closer to the tip of the blade, the faster the blade is moving through the air, then the greater the apparent wind angle is. Typically, the twist along blade's length goes from $10 - 20°$ from root to tip. Near the root structural requirements are the preference and thereafter low effective aerodynamic take out is expected.

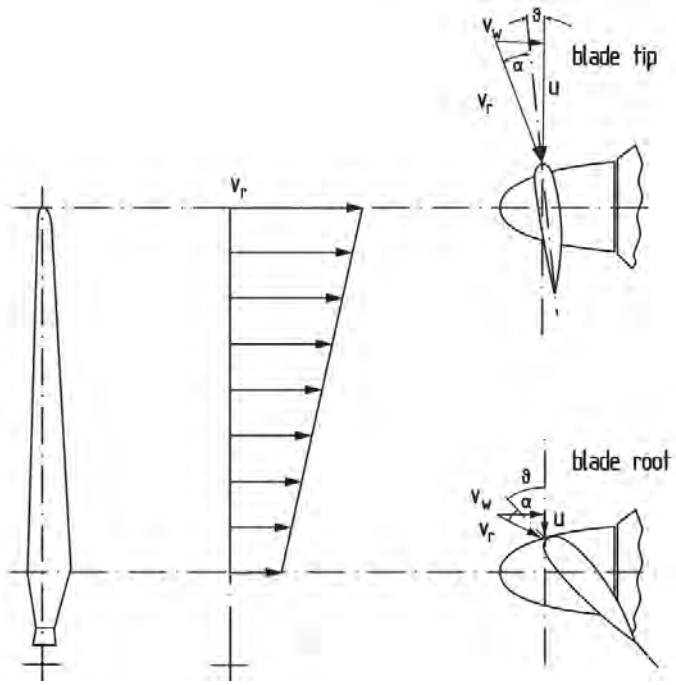

Figure 1.4. Twist along blade's length.

1.3 2-D aerodynamics of wind turbines.

Aerodynamic forces are functions of the velocities shown in figure 1.3, specifically of $\vec{W}$. Even though it is in the downwind direction (parallel to rotor axis), drag force has an effect of lift due to $\vec{W}$ which is stronger than true wind but the angle is less favourable to torque, slowing the blade down.

Acting forces generated over the aerofoil are shown in figure 1.5, where $A(r)$ = is the reaction at r location, or axial reaction and $T(r)$ = is the torque at r location, or tangent reaction. These reacting forces may be broken down into convenient components with a design-analysis aim. An efficient rotor blade consists of several aerofoils blended at an angle of twist terminating at, e.g. circular flange. For this reason, the study of aerodynamic profile is the main concern for designing and proposing specific blade geometries.

The *spanwise* velocity component over a wind turbine blade is much lower than the *streamwise* component, and it is therefore assumed in many aerodynamic models that the flow at given radial position is two dimensional and 2-D aerofoil data can thus be applied. Two-dimensional flow is comprised of a plane and if the plane is described with a coordinate system, the velocity component in the z-direction is zero [20].

In order to realize a 2-D flow it is necessary to extrude an aerofoil into a wing of infinite span. On a real wing the chord and twist changes along the span and the wing starts at a hub and ends in a tip, but for long slender wings, like those on modern gliders and wind turbines, Prandtl demonstrated that local 2-D data for the forces can be used if the angle of attack is corrected accordingly with the trailing vortices behind the wing [37]. It is now clear that 2-D aerodynamics is of practical interest even though it is difficult to realize [20] [38].

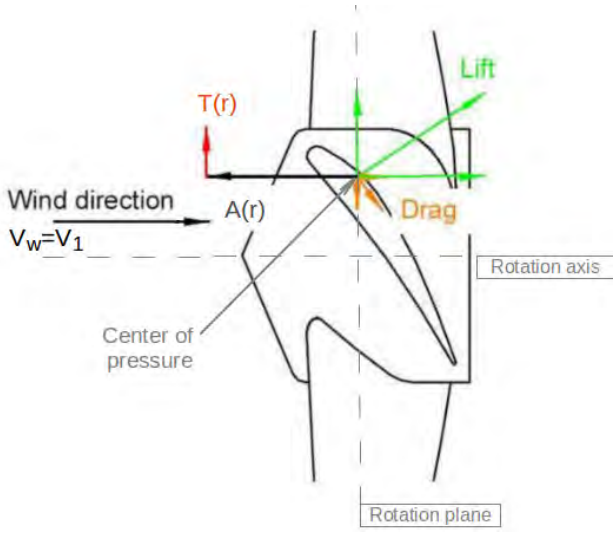

Figure 1.5. Aerodynamic forces generated at a blade element.

A further reason to consider a 2-D model is, if we desire to design a blade, a simple and effective method for calculating plan-shape (explained at subsection 1.4.3 and which gives the basic shape of a modern HAWT), assumes a well calculated lift coefficient (and maintained) for each section [38].

1.3.1 Lift and drag

As seen in subsection 1.2.1, an aerodynamic load is generated by lift and drag of the blade's aerofoil section (figure 1.3) which is a function of wind velocity (V_w), blade velocity (U), surface finish, angle of attack(α) and yaw (a mechanism that rotates the whole nacelle, used to keep the rotor facing into the wind as the wind direction changes). The goal is to resolve produced lift and drag into useful thrust (T) in the direction absorbed by the generator.

Lift will only be present if the flow incorporates a circulatory flow about the body and will be given (for small angles of attack) by the Kutta-Joukowski theorem [12].

The lift is defined by $L = \varrho(\vec{\Gamma} \times \vec{U})$ or, since L is perpendicular to U, $L = \varrho_\infty U_\infty \Gamma$, where Γ is the circulation, or vortex strength, defined by $\Gamma = \oint v \cdot ds$. To achieve a circulatory flow about a non-rotating body it must have a sharp trailing edge like an aerofoil cross-sectional shape or a thin plate [12]. Also, the Kutta-condition must be complied, which implies identifying a particular value of the circulation that moves the rear stagnation point ($U = 0$) exactly on the trailing edge, leaving the other stagnation point at the leading edge [20]. Lift is the responsible force for the power yield generated, which is why it is essential to maximise it.

For a long body, such as a wind turbine blade, the lift per unit span is used in the definition and the plan area is replaced by the chord length. Considering $\Gamma = \pi U c \sin\alpha$ as the circulation on an airfoil,

$$C_l = \frac{\text{Lift/unit span}}{\frac{1}{2}\varrho U^2 c} = \frac{\varrho\,(\Gamma \times U)}{\frac{1}{2}\varrho U^2 c} = \frac{\varrho \pi U c \sin\alpha U}{\frac{1}{2}\varrho U^2 c} = 2\pi \sin\alpha$$

where c is the chord of the airfoil. In practice $C_l = a_0 \sin\alpha$, where a_0 is called the lift-curve slope. Because the angle of attack is small, often the equation is written as $C_l = a_0\,\alpha$. Lift, thus will depend on α and flow speed U [12].

Drag is a force component parallel to the effective wind direction, i.e. in our present context, the relative velocity V_w. Basically there are two types of drag involved with our present problem:

- Skin Friction Drag (due Viscosity and Roughness) caused by the interaction between a solid and fluid, the magnitude of skin friction drag depends on the properties of both. In the case of solid, a rough surface will have a high skin friction drag and a smooth surface, a low one. On the fluid, it is caused by shear stress at all points over the immersed body concerned where fluid is touching, acting tangentially to the surface. Here drag is due entirely to the viscosity and thus it is Reynolds number dependant. Relative velocities causes internal friction between layers inside boundary layer. The cumulative effect of all these friction forces contributes to produce drag. On

a streamlined body, skin friction drag is the responsible for most of the drag because fluid has a longer contact along the surface.

- Form Drag (or Pressure Drag) due to flow separation which creates a pressure difference between front and back of an object. This difference between high and low pressure regimes opposes the motion of a moving object. A blunt body is one where most of the drag is pressure drag, while a streamlined body will reduce form drag.

Parasitic drag is a combination of these kinds of drag and interference drag. *Induced* drag is mainly involved with 3-dimensional cases. Parasite drag increases with speed. Induced drag decreases with speed. The sum of both shows that there is only one airspeed for a given wind turbine design and load that provides minimum total drag. This is the point which is the maximum lift-to-drag ratio[5].

1.3.2 Lift to drag ratio.

The most important parameter of the airfoil is the lift-drag ratio[21].

$$L/D = \frac{C_L}{C_D}$$

The lift/drag ratio, denoted as L/D, has a significant effect upon the efficiency of a wind turbine and it is recommended that a turbine blade operates at the maximum ratio[12]. In order to obtain highly accurate L/D, and because it is difficult to predict mathematically, the use of available simulation software is recommended. The local lift coefficients must be derived from the polar curves of the selected airfoil and by considering the local angle of attack, i.e. the blade pitch angle and the blade twist angle. This means that aerodynamically the optimum distribution of chord and twist of the rotor blades depends on the selection of a particular lift coefficient. As rule, this lift coefficient will be selected at best L/D for its correspondent λ value. As a first approximation design C_L may range between 0.9 and 1.1.

Reynolds number influences C_L and C_D: The nature of the flow pattern around an aerofoil is determined by the Reynolds number and this significantly affects the values of the lift and drag coefficients. The general level of the drag coefficient increases with decreasing Re and below a Re_{crit} of about 2×10^5 the boundary layer (see subsection 1.3.3) remains laminar, therefore causing a sharp rise in the coefficient. The affect on the lift coefficient is largely concerned with the angle of attack at which the stall occurs (see also subsection 1.3.3). As Re rises so does the stall angle and, because the lift coefficient increases linearly with angle of attack below the stall, the maximum value of the lift coefficient also rises[12].

1.3.3 Boundary layer and flow separation (stall).

The boundary layer is a thin region of slow moving fluid, close to the body surface, within which viscous forces predominate. Outside this layer the flow behaves almost inviscidly. The drag on the body caused directly by viscosity is quite small but the effect of this thin layer on the flow pattern is profound. The drag on an aerofoil can be attributed both to pressure and viscous sources and the drag coefficient varies significantly with both angle of attack and Reynolds number[12].

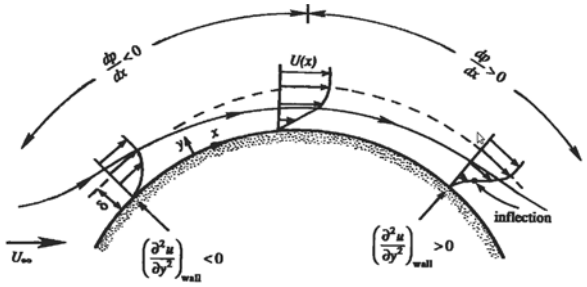

Figure 1.6. Velocity profiles across boundary layers with favourable and adverse pressure gradients.

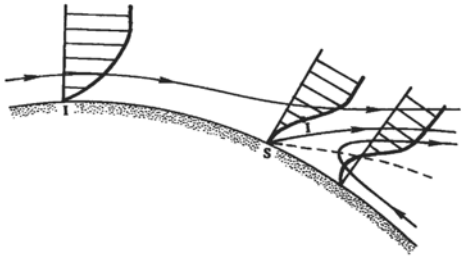

Figure 1.7. Streamlines and velocity profiles near a separation point *S*. Point of inflection is indicated by *I*. The dashed line represents u=0.

The boundary layer in a decelerating stream has a point of inflection, the existence of this point implies a slowing down of the region next to the wall, a consequence of the uphill pressure gradient. Under a strong enough adverse pressure gradient, the flow next to the wall reverses direction, resulting in a region of backward flow. The reversed flow meets the forward flow at some point S at which the fluid near the surface is transported out into the mainstream. This is known as the flow separation from the wall. The separation point S is defined as the boundary between the forward flow and backward flow of the fluid near the wall where stress vanishes: $\left(\frac{\partial u}{\partial x}\right)_{wall} = 0$.

To avoid separation and large drag, the trailing section of a submerged body should be gradually reduced in size, giving it a streamlined shape. The point of separation is insensitive to the Reynolds number as long as the boundary layer is laminar. However a transition to turbulence delays boundary layer separation[26]. Laminar and Turbulent Boundary Layers may occur: Turbulence can be artificially triggered by roughening the body surface. General flow turbulence tends to produce turbulent boundary layers at Reynolds numbers below critical value and this certainly seems to happen in the case of wind turbine blades[21].

If the angle of attack exceeds a certain critical value, separation of the boundary layer will take place. This causes a wake to form from above the aerofoil, reducing the circulation and lift, and increasing the drag. Under these circumstances, the flow past the airfoil is stalled [12].

1.3.4 Pressure variation around the airfoil.

The pressure variation (minus the ambient static pressure) in the upper surface of an airfoil is subject to suction and is responsible for most of the lift force. Figure 1.8 illustrates the pressure distribution at the surface of an airfoil. The effect of the boundary layer(see next subsection) is to reduce the pressure distribution at the rear of the aerofoil. The modified pressure distribution gives rise to pressure drag which is added to the skin friction drag also caused by boundary layer [12] (see figure 1.9).

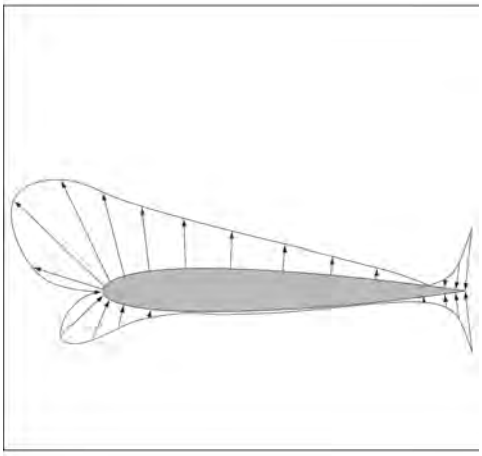

Figure 1.8. Pressure distribution around a symmetric airfoil.

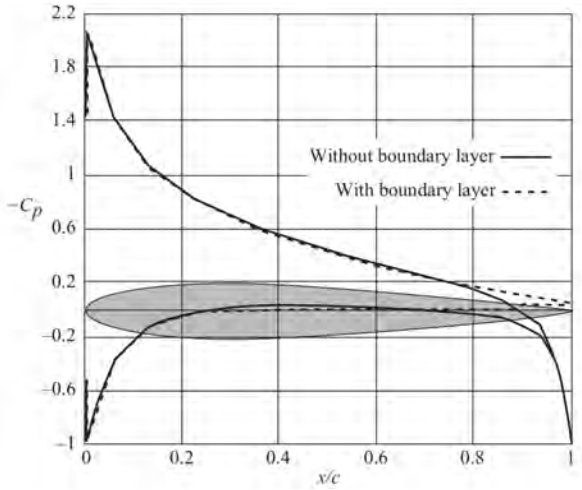

Figure 1.9. Graph $x/c - C_P$ showing boundary layer effects at the trailing edge.

1.4 HAWT blade design features

1.4.1 Blade pitching.

Once the wind in the site is measured, a design speed is established. Afterwards, it is possible to determine optimum dimensioning for a wind turbine blade. Constant velocities are desirable but wind conditions are variable for any site and the turbine must operate at

out of design conditions. A method for limiting the rotational speed must be implemented to prevent excessive loading of the blade and to maintain a high efficiency at rated wind speeds. As the oncoming wind velocity directly affects the angle of incidence of the resultant airflow onto the blade, the blade pitch angle must be altered accordingly. This is known as pitching, which maintains the lift force of the airfoil section.

Pitching methods are: (1) Feathering, by decreasing the pitch angle (using a clever algorithm which uses wind condition) reducing the angle of attack and thus reducing lift; (2) Inducing stall, increasing the angle of attack which can result in excessive dynamic loads. In order to prevent fluttering, feathering is a better option though it requires a higher mechanical movement (see figures 1.10). Passive stall control also limits rotor speed under an increased wind velocity using a *fixed pitch angle* at which stall starts automatically. This method requires a safety margin and thus has performance penalties, hence it is usually applied in small turbines (see figure 1.11) [21] [38].

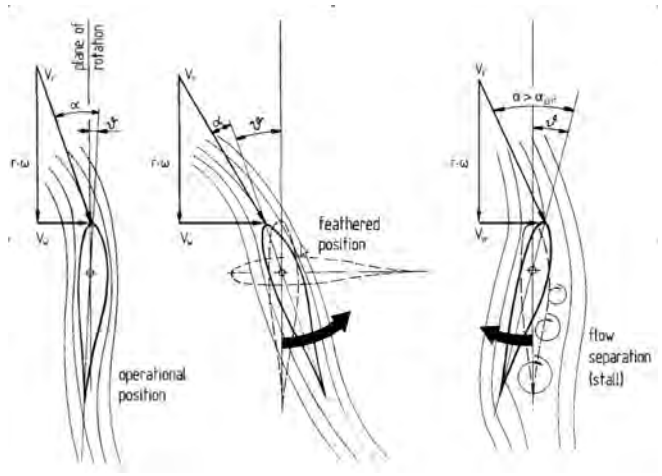

Figure 1.10. Blade pitching. Feathering and induced stall.

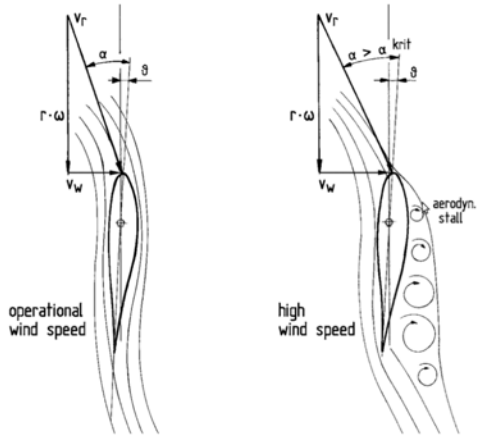

Figure 1.11. Passive stall control at operational and high wind speed.

1.4.2 Blade section aerodynamics (airfoils).

The primary objective of wind turbine design is to maximize the aerodynamic efficiency, or power extracted from the wind. In practical design, this objective should be met together with constraints on mechanical strength criteria and economical aspects [1]. The blades cutting through the air improve and enhance aerodynamic lift due to changes to their shape through their length, accommodating different relative air speeds between the tip and hub [2]. The influence of L/D on the power coefficient of the rotor can be represented in a general way as shown in figure (1.12).

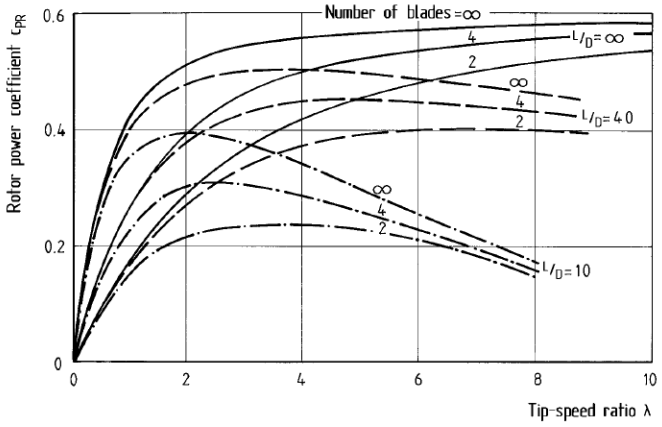

Figure 1.12. L/D ratio influence over C_{PR} for different number of blades.

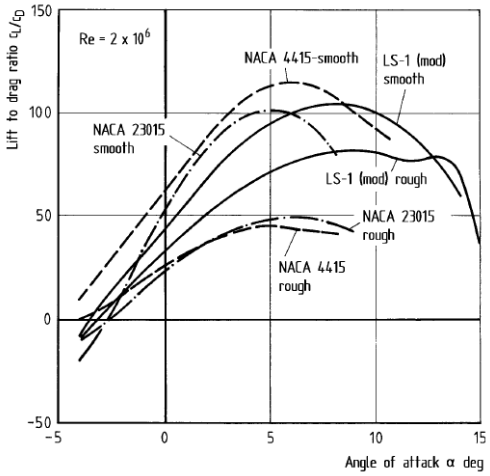

Figure 1.13. Influence of roughness on C_{PR} for different NACA airfoils.

It is clear that C_{PR} will become smaller if L/D decreases for every number of blades. Notice that for all L/D, the optimum point of the C_{PR} shifts to lower λ values. Thus, high-speed rotors manage well with fewer blades, but airfoil characteristics become a decisive factor for power generation[21]. In general the best L/D characteristics are obtained by an aerofoil that is fairly thin: its thickness may be only 10-15% of its chord length. Due to structural reasons, at the root, aerofoil shape has less aerodynamic efficiency.[3].

At the beginning of wind turbine blade design, wind power rotors used airfoils developed for aircraft wings such as four and five-digit NACA airfoils series. Nevertheless, the requirements made for wind rotor are not in every way identical. Special series have been developed in order to minimize performance losses due to surface roughness, or to achieve a particular stall behaviour. Some examples are LS, SERI and FFA series. Commonly modern NACA airfoils are series 44 and 230, also known as laminar airfoils.

Laminar airfoil shapes keeps flow boundary layer laminar along a long section of the chord length, with an extremely low drag over a certain angle of attack range[21]. Cambered airfoils, such as the NACA4412, have curved chord lines and this allows them to produce lift at zero angle of attack. Usually, cambered airfoils have higher maximum L/D ratios, compared to symmetrical aerofoils at positive angles[12].

Airfoil special series may have the following roughness characteristics: (1) slightly lower L/D, but less sensitive to surface roughness, or (2) higher L/D ratio but also more sensitive to surface roughness. So the required surface quality, as well as the contour accuracy must be feasible to manufacture. Degradation due to environmental influences must be taken into consideration, as well as different kinds of dirt in the wind, which is why the performance

must be based on a standard roughness[21]. Figure 1.13 shows influence of roughness on C_{PR} for different airfoils.

In regards to the aerodynamics of the blade thickness, the high-performance airfoils are the thinnest possible rotor blades. In contrast, the structural requirements demand a thick cross section for the load bearing elements. The goal then is to show the influence of thickness-to-chord ratio on rotor performance and energy yield. Materials and manufacturing processes influence on how thin the blade can be built. Aerodynamic requirements determine the design, but the cost of construction must be reasonable. The aerodynamic shape gives rise to loads, which are fed to the structural design. Design must be thin (ideal), and thicker closer to the root, where stresses due to bending are greatest. A trade-off is necessary between aerodynamic and structural efficiencies. Making a thicker blade at the root instead of reinforcing it can reduce the cost greatly.

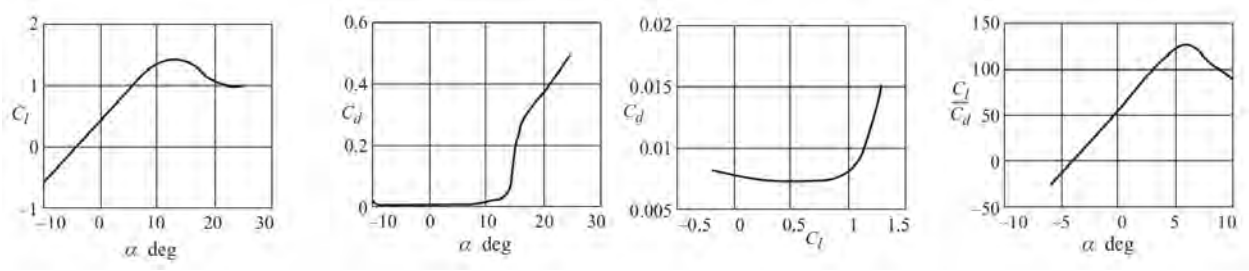

Figure 1.14. Graphs examples for an airfoil NACA4412.

1.4.3 Blade planshape, quantity and span.

According to Betz's theory, the crucial criterion for calculating the optimum theoretical shape of contour is that the demand at each blade radius and the wind speed in the rotor plane be delayed into two thirds of its undisturbed value. This requirement can be met if the product of the coefficient of local lift and local chord length follows a hyperbolic course over the blade's radius. The hyperbolic contours of the theoretical optimum shape present disadvantages for manufacturing. Moreover, straight-bladed planforms have power losses. Trapezoidal planforms are cost-effective for its manufacturing and also have a very good performance. In this sense, from an aerodynamic point of view, the outer blade area is then of much more importance for the rotor's perfomance. Because the blade near the hub is of less significance for the generation of power, higher strength with greater simplicity in manufacturing is allowed. The shape of the tip influences the tip vortices produced and thus induces aerodynamic drag.

For the chord length calculation, an ideal planshape (or planform) of a HAWT rotor blade is defined using the BEM method, by previously calculating the chord length according to Betz limit, local air velocities and the airfoil lift. One of the simplest theories for calculating the optimum chord length is based on the Betz optimization[19]:

$$c(r)_{Betz} = \frac{16\pi R}{9BC_L} \frac{1}{\lambda\sqrt{\lambda^2\left(\frac{r}{R}\right)^2 + \frac{4}{9}}}$$

$c(r)_{Betz}$ = optimum chord length,
r =local radius (variable),
R =total radius,
B =blade number,
C_L = lift coefficient at chosen α_D,
λ = local TSR.

This equation gives a good approximation for $\lambda \approx$ 5-9. For our example, we want to $c(r)_{Betz} = 1.0$ at the tip. Then, using this expression, we will have at the tip ($r = R$) $R = 9.4834$, using a $C_L = 0.70$ that is commonly used for preliminary computations, $\lambda = 5$ and $B = 3$. From here, we will use $R = 9.5$ as a practical approximation for the exercise to be presented in chapter 4.

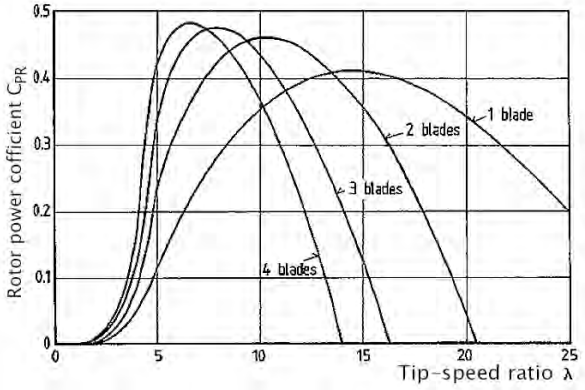

Figure 1.15. Influence of the number of blades on the rotor power coefficient and the optimum tip-speed ratio.

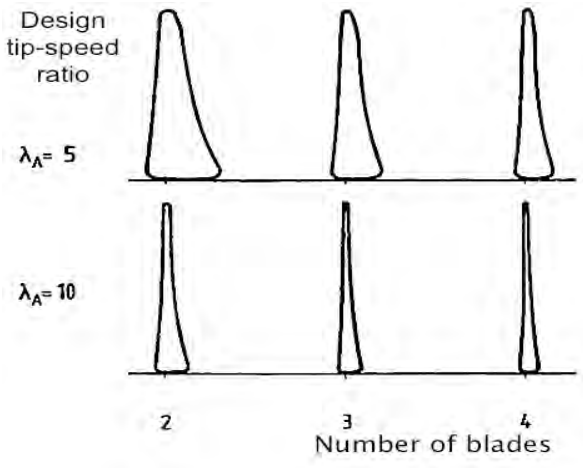

Figure 1.16. Optimum rotor blade shapes for different design λ and blade numbers, for NACA 4415 and $c_{L,design} = 1.1$.

A longer blade will favour the power extraction, due to the fact that it implies a major sweep area. But, by increasing the blade length, the deflection of the blade tip due to axial wind force will also increase. Another parameter associated with length and often used for characterizing the geometrical rotor blade shape are solidity (see table 1.1), aspect ratio ((rotor radius)^2 / planform area of a rotor blade) and taper (chord length at the blade tip/ chord length at the blade root); e.g. in order to avoid problems related to the strength or stiffness of a manufactured slender blades, the blade's aspect ratio must be reasonable. It is necessary to provide the blade with a constant slowing effect over the rotor disc so that none of the air leaves the turbine or passes through too fast, failing to absorb energy. The blade design can narrow closer to the tip than the root, whilst still generating sufficient lift [3].

Now, on the other hand, considering the number of blades, figure (1.15) shows the influence of this parameter on the C_{PR} (valid for any type of HAWT blade), and figure 1.16 shows its relation with planshapes respect to λ, where the NACA airfoil is described in subsection 1.4.2.

There is a small increment in maximum C_{PR} while increasing the quantity of rotor blades, as seen in figure 1.15. The curves within the range which the C_{PR} is larger than the threshold is reduced as the number of blades increases [21] [1]. That is to say, the rotors with less blades rotate faster, thus compensating for their disadvantage of having a smaller physical blade area [21]. By increasing the number of blades, the cost of the system increases drastically and the mechanical design of blades becomes a difficult task: The more blades there are, the thinner they should be in order to be aerodynamically efficient. [1].

Literature review

In the present review, we look for airfoil design and optimization researches, but mainly tools and models of the flow field calculation around the airfoil using any developed or commercial of computer aided solution that uses finite volume method (FVM), among other common methods where available literature is focused on solving the Navier-Stokes equations, or other types of analysis method. Literature review of optimization problems may be structured as follows: airfoil shape optimization, wind turbine blade performance optimization (where the shape of the airfoil is fixed and the design variables are limited to the blade); and wind turbine optimization of the wind turbine is fully modelled. Other optimization problems include the different tools and models used in aerodynamic, structural and wind speed modelling, and finally, optimization algorithms[13].

To avoid excessive lift performance which may lead to an abrupt stall for the airfoil design, Grasso[18] provides and upper limit for the C_L at a specific AOA and a maximum drop after such point, based on[22,41]. Ju et al.[24] restrict the drag coefficient value in the airfoil geometry optimization to prevent it from undesirably becoming higher during the optimization of the L/D and C_L of the airfoil. An important field for the development of wind turbines is the optimization of the airfoil shape through the design of new airfoil families[40,41] suited for the blades. We examine the performance optimization approaches for wind turbine airfoils presented in[17,24,40].

For airfoil optimization via CFD assisted by other tools, Lin et al.[42] propose how to design and analyze flow over an airfoil shape of a horizontal axis wind turbine for 5 kW power generation using BEM theory, and using COMSOL Multiphysics® as an analysis software, choosing the NACA 4409 airfoil with angle of attack 5 degrees as the optimum blade design, and thus suitable to construct the HAWT for design average wind speed. Najar et al.[35] reviews the design optimization of blades. They determine the flow field around the airfoil of the wind turbine responsible for the buildup of forces acting on the airfoil. A CFD model has been used to calculate the aerodynamic effect on the blade airfoil at a critical Reynolds number and constant wind speed under different turbulence models with inviscid flow so that the blade achieves an optimum power performance with an optimum value for L/D. Zhu et al.[45] integrates a method to design airfoils and the rotor blade by determining the airfoil optimization based on the blade local speed ratio. Local 2D airfoil BEM computations were performed during the airfoil optimization which provide high C_P values over a wide range of

AOA. Final results shows an optimal flow angle and chord length. Validations carried out by full blade BEM and CFD both showed good aerodynamic characteristics. The integration of the simplified BEM and XFOIL® can be regarded as a reliable tool for airfoil and rotor platform design.

Regarding models and tools, a mathematical model for fluid dynamics wind turbine design based on the BEM (from the Glauert propeller theory) has been implemented and improved by[27] using mathematical simulations compared with experimental data found in the literature. A good agreement was found, and the model was implemented to optimize rotor performance.

Once the design conditions are set up, which are the rated wind speed, the design tip speed ratio and the design angle of attack, it is possible to display the linear distributions of the pitch angle in each section. This is how Bai[10] designs a HAWT blade by BEM theory and the modified stall model. The blade aerodynamics are also simulated to investigate its flow structures and aerodynamic characteristics. Investigations of aerodynamic characteristics for the turbine blade were performed by the numerical simulation.

The Reynolds averaged Navier-Stokes (RANS) equations combined with the Spalart-Allmaras turbulence model that describes the three dimensional steady state flow on the wind turbine blade were solved with the aid of a commercial CFD code. The simulation results are compared with the improved BEM theory which demonstrates that the CFD is a good method on aerodynamic invesigation of a HAWT blade. A good match between the improved BEM theory and the numerical simulation was achieved.

For exclusive CFD analysis of the system, Almohammadi et al., present two papers[7,8]; in the first they proposed a solution produced by using the 2D Unsteady Navier-Stokes equations (URANS) with two turbulence models using a mesh independent approach for convenience, and mainly due to the sensitivity of the power coefficient produced by the turbine to the dynamic stall phenomenon and the turbulence level around the blades. The model includes three VAWT 2D-blade systems immersed in the fluid domain. In the second paper, he uses 2D Navier–Stokes equations to investigate the dynamic stall process in the VAWT 2D-blade system. Due to an existing experimental work of a VAWT in upright and tilted conditions, Chowdhury et al.[14] did a numerical validation by means of CFD analysis by solving Unsteady Reynolds Averaged Navier-Stokes (URANS) equation, choosing a turbulence model and achieving a mesh dependency analysis and an optimum time step. A good agreement between experimental and theoretical results were obtained at both tilted and upright positions. Lanzafame et al.[28] modeled RANS turbulence models for the prediction of the flow field around wind turbines. The results demonstrate the good capabilities of the transition turbulence model. The 2D CFD model was calibrated and validated comparing the numerical results with experimental data. The process of generating the 2D CFD model was done inside the ANSYS Workbench multi-physics®. Particularly, the finite volume Fluent Solver was used in an Unsteady RANS (URANS) version to solve the Navier-Stokes equations and capture the unsteadiness. A good agreement between numerical and experimental data was

found. Li et al.[30] presented a dynamic overset CFD simulations, studying two sequences of the experiment test cases with complete turbine geometry, including the NREL phase VI blades, and approximate geometries for hub, nacelle and tower. RANS and DES models are used in the simulations. Results show that the CFD predictions match the experimental data consistently well, including the general trends of power and thrust, sectional normal force coefficients and pressure coefficients at different sections along the blade.

Classic literature is very handy and important as supportive literature, like refs.[9,12,20,21,32,43].

Chapter 2

Programming and validation

2.1 Solution of Navier-Stokes equations by numerical methods.

The use of computational fluid dynamics (CFD) to predict both internal and external flows has grown enormously in recent decades. Even today the development of CFD software to analyze aerodynamic problems by which we get answers necessary for the evaluation and design is widely developed. It is also possible to use certain methodologies to directly apply CFD analysis on turbine blades.

The geometry of the blade is an aerodynamic shape, with non-linear chord and twist distribution. This can be calculated based on the BEM theory, with respect to a given coefficient and profile. Four models may be used to predict the performance of the blades: BEM model (blade element momentum), lifting panel and vortex model, actuator line model, and CFD (computational fluid dynamics) [35].

The following section is a description of how a CFD technique known as *Finite Volume Method* is incorporated into a computer code for solving a discretised or algebraic form of the governing equations of a fluid in order to study the flow around 2D blades.

2.1.1 Non-dimensional Navier-Stokes equations.

This section briefly describes the physical fundamentals of mathematical modelling of fluid dynamics, specifically of the governing equations for 2D. The governing equations of fluid flow that mathematically represent the physical laws of conservation of mass and momentum can be written for one, two or three dimensions. Our main focus for this study is based on the two-dimensional solution. The non-dimensional form of the mass and momentum conservation equations in two dimensions (x, y) can be written as [16]:

$$\frac{\partial u}{\partial x} + \frac{\partial v}{\partial y} = 0, \tag{2.1}$$

$$\frac{\partial u}{\partial t} = -\frac{\partial uu}{\partial x} - \frac{\partial uv}{\partial y} - \frac{\partial p}{\partial x} + \frac{1}{Re}\left(\frac{\partial^2 u}{\partial x^2} + \frac{\partial^2 v}{\partial y^2}\right), \tag{2.2}$$

and

$$\frac{\partial v}{\partial t} = -\frac{\partial vv}{\partial x} - \frac{\partial uv}{\partial y} - \frac{\partial p}{\partial y} + \frac{1}{Re}\left(\frac{\partial^2 u}{\partial x^2} + \frac{\partial^2 v}{\partial y^2}\right) \tag{2.3}$$

where equation 2.1 is a continuity equation as an incompressible fluid, i.e. $\varrho = \varrho_0 = \text{constant}$, which has to be coupled with the non-linear time-dependant momentum equations, where the primitive variables are the velocity components u, v, and the pressure p. Note that the mass and momentum conservation equations are referred to as the continuity and Navier-Stokes equations respectively.

The scaling was made as follows: The sole parameter of the system is the Reynolds number defined by $Re = \frac{\varrho_0 V_\infty L}{\mu}$, V_∞ is a stream free velocity, L is a characteristic length and μ is the dynamic velocity. The steady N-S equations are formally elliptic in space and the unsteady equations are parabolic in time.

2.1.2 A solution for the Navier-Stokes equations in a two-dimensional domain using finite-volume method.

The finite-volume method (FVM) is a method for representing and evaluating partial differential equations in the form of algebraic equations[29]. The general transport equation written in terms of a general variable ϕ is used for solving the governing equations for flow. We know that all fluid flow equations, including equations for scalar quantities can be usefully written as:

$$\frac{\partial(\varrho\phi)}{\partial t} + \nabla \cdot (\varrho\phi\mathbf{u}) = \nabla \cdot (\Gamma \nabla \cdot \phi) + S_\phi \tag{2.4}$$

Various phenomena are involved in equation 2.4: a rate of change and a convective term at the left, and a diffusive with a Γ diffusion coefficient and the source term S_ϕ at the right side.

Observe that considering two-dimensions, ($\phi = u, v$), the diffusion coefficient is equal to the constant viscosity μ, and $S_\phi = -\nabla \cdot p$, the general transport equation, becomes the dimensional form of equations 2.2 and 2.3.

This equation is used as a starting point for the computational procedures in the finite volume method, by setting ϕ equal to any corresponding variable (1, u or v), and selecting the appropriate diffusion coefficient Γ and source term S_ϕ, for each partial differential equations

for mass and momentum conservation. In time-dependent problems it is necessary to integrate with respect to time over a small interval Δt. It is also necessary to divide what will be a computational domain into discrete control volumes. The time and space integration yields the following integral form for the time-dependent process of the transport equation [43]:

$$\int_{\Delta t}\frac{\partial}{\partial t}\left(\int_{CV}(\varrho\phi)dV\right)dt+\int_{\Delta t}\int_{A}\mathbf{n}\cdot(\varrho\phi\mathbf{u})dA\,dt=\int_{\Delta t}\int_{A}\mathbf{n}\cdot(\Gamma_{\phi}\nabla\cdot\phi)dA\,dt+\int_{\Delta t}\int_{CV}S_{\phi}dV\,dt \quad (2.5)$$

where CV is a control volume. We place a total number of nodal points at the frontiers of the domain. The boundaries of the faces of each control volume or cell will be positioned mid-way between adjacent nodes. Thus, each node is surrounded by a cell. It is common to set nodes at the edges and corners of the domain where boundary conditions are established.

The common convention for CFD methods use the system notation that identifies P as the actual nodal point; west and east nodes as W and E, respectively. West and east faces are referred as lowercase w and e. Distance between nodes are identified as δx and δy. This convention happens mainly for the scalar variable (p), which in figure 2.1 (a) and (b) are represented as an orange square and nodes are shown as black dots with capital (I, J) locations.

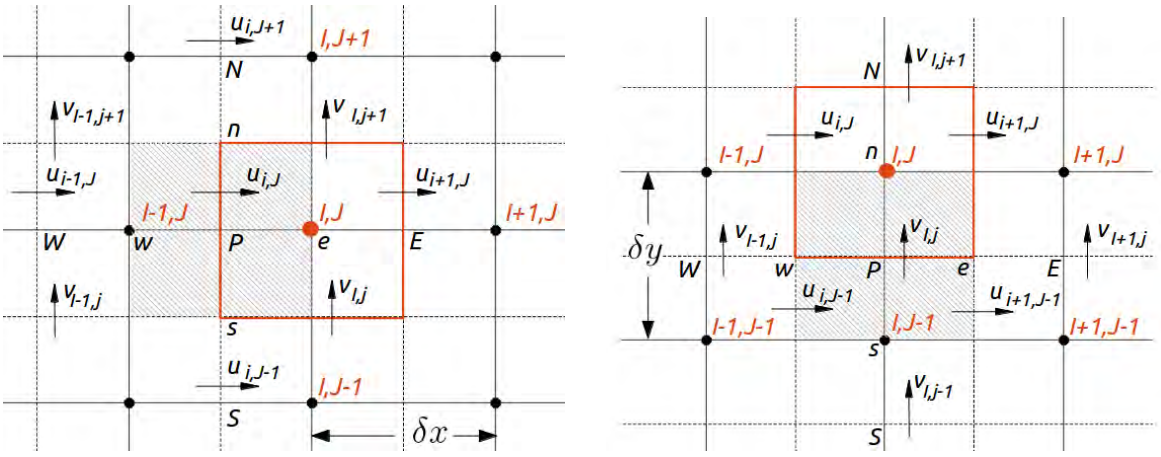

(a) u-control volume (b) v-control volume

Figure 2.1. Staggered control volumes and their neighbouring velocity components. Showed the scalar control volume (orange square) on both figures and the staggered (a) u-velocity and (b) v-velocity control volume (hatched area). Uppercase denotes the scalar grid and lowercase the velocities grid.

The finite volume method starts with a discretisation of the flow domain, but we need to decide where to store velocities. It isn't possible to store velocities on the same locations

as the scalar variables, i.e. the same nodes, because a highly non-uniform pressure field can act like a uniform field in the discretised momentum equations. Therefore, a staggered grid is needed to solve this, as shown in figures 2.1, for (a) u and (b) v velocities (hatched control volumes, denoted with lower case notation (i, j)), in order to avoid non-zero pressure gradient terms. The idea is to evaluate pressure p in ordinary nodal points, and velocity components on staggered grids centered around the cell faces.

The key step of the finite volume method is the integration of governing equations over a control volume to yield a discretised equation at its nodal point P. A clear advantage of the method is that the discretised equation has a clear physical interpretation. Based on equation (2.5), and substituting each term by a balance equation of ϕ related to physical processes for each control volume and rearranging them, we obtain the following form for a general internal node point of the discretised equations, considering a uniform regular gridded 2-D domain[43]:

$$a_P\phi_P = a_E\phi_E + a_W\phi_W + a_N\phi_N + a_S\phi_S + S_P \tag{2.6}$$

where each a coefficient may include contributions of convective or diffusive balances, or even a source model. This equation system must be iteratively solved by, for example, using a direct tridiagonal matrix (TDMA) method, incorporated as FORTRAN subroutines within the code.

Due to an issue involving the solution for the pressure field, so a pressure-velocity coupling strategy must be devised. In general, the velocity field is not known and emerges as part of the overall solution process along with other flow variables, so a numerical strategy for computing it is required. The transport equation for each velocity component can be derived from the equation 2.4 by replacing u, and v, thus satisfying equation 2.1. The problem arises for solving equations (2.2) and (2.3), because in first place, they contain non-linear quantities in the convective term, and even more, there is no transport or state equation for solving pressure.

Since the velocity and pressure are coupled, if the correct pressure field is applied in the momentum equations, then the resulting velocity field should satisfy continuity. But, due to the fact that the pressure field is unknown, we need a method for calculating and correcting pressure on each iteration step in order to get closer to convergence criteria.

An iterative solution strategy is based on the SIMPLE (Semi-Implicit Method for Pressure-Linked Equations) algorithm, which essentially is a guess-and-correct procedure for the pressure calculation on the staggered grid. In this study a variation called SIMPLE-Consistent or SIMPLEC algorithm, that follows same SIMPLE algorithm, but omits terms less significant was used[43].

To initiate the SIMPLEC calculation process a pressure field p^* is guessed. Discretised momentum equations are solved using p^* to yield velocity components u^* and v^* that are

the resultant velocities obtained from the guessed p^*. Now, we define the correction p', so that $p = p* + p'$, where p is the final pressure field. Then we define the velocity corrections u' and v' to correct the velocities u and v, as well, $v = v* + v'$ and $v = v* + v'$ [43].

The sequence of operations of the SIMPLEC algorithm are the following:

1. Propose an initial guess p^*, u^*, v^*.

2. Solve discretised momentum equations to obtain $u*, v*$ using previous guessed p^*, u^*, v^*, ϕ^* by solving,

$$a_{i,J}u^*_{i,J} = \Sigma a_{nb}u^*_{nb} + (p^*_{I-1,J} - p^*_{I,J})A_{i,J}$$
$$a_{I,j}v^*_{I,j} = \Sigma a_{nb}v^*_{nb} + (p^*_{I,J-1} - p^*_{I,J})A_{I,j}$$

   where summation $\Sigma a_{nb}u^*_{nb}$ refers to neighbour cells values on the staggered grid, and the last term represents the pressure.

3. Solve pressure correction equation to obtain p' using previously computed $u*, v*$ by solving,

$$a_{I,J}p'_{I,J} = a_{I-1,J}p'_{I-1,J} + a_{I+1,J}p'_{I+1,J} + a_{I,J-1}p'_{I,J-1} + a_{I,J+1}p'_{I,J+1} + b_{I,J}$$

   which represent the discretised continuity equation that determines the pressure correction p'. The source term b' is the continuity imbalance arising from the incorrect velocity field u^*, v^*. So, b' must tend to zero in order to obtain pressure correction field and thus p, u, v.

4. Correct pressure and velocities to obtain p, u, v using p' by solving,

$$p_{I,J} = p^*_{I,J} + p'_{I,J}$$
$$u_{i,J} = u^*_{i,J} + u'_{i,J}$$
$$v_{I,j} = v^*_{I,j} + v'_{i,J}$$

   where u' and v' velocity corrections equations are:

$$u'_{i,J} = d_{i,J}(p'_{I-1,J} - p'_{I,J}) \qquad \text{and} \qquad v'_{I,j} = d_{I,j}(p'_{I,J-1} - p'_{I,J})$$

   where ,

$$d_{i,J} = \frac{A_{i,J}}{a_{i,J} - \sum a_{nb}} \qquad \text{and} \qquad d_{I,j} = \frac{A_{I,j}}{a_{I,j} - \sum a_{nb}}$$

5. Compare to convergence criteria, i.e. $b'_{I,J} < tolerance$ and take a decision: If it complies, then stop loop. If it doesn't comply, then go back to start using new values, setting $p* = p, u* = u, v* = v, \phi^* = \phi$.

The values of coefficients $a_{I,j}$, $a_{i,J}$ and a_{nb} may be calculated with any of the differencing methods i.e. upwind, hybrid or QUICK[43]. In our case, a central difference scheme for the coefficients is chosen for its mathematical hardiness, though it may fail under certain situations involving convection. In order for numerical results to be physically realistic, fundamental properties of discretisation schemes must be observed, such as: Conservativeness, boundedness and transportiveness.

For a uniform grid we can write the cell face value property ϕ as $\phi_e = (\phi_P + \phi_E)/2$ and $\phi_w = (\phi_W + \phi_P)/2$, by solving equation 2.6. By identifying the coefficients of u in our code, the central differencing expressions for the discretised convection-diffusion equation in two-dimensions 2.6, result as follows[43]:

$$
\begin{aligned}
a_E &= (\tfrac{1}{Re}\,\frac{s_e}{\delta x}) - (u_e\, s_e)/2 \\
a_W &= (\tfrac{1}{Re}\,\frac{s_w}{\delta x}) + (u_w\, s_w)/2 \\
a_N &= (\tfrac{1}{Re}\,\frac{s_n}{\delta y}) - (u_n\, s_n)/2 \\
a_S &= (\tfrac{1}{Re}\,\frac{s_s}{\delta y}) + (u_s\, s_s)/2 \\
a_P &= a_E + a_W + a_N + a_S + \frac{dV}{dt} \\
s_P &= u_{i,J}\,\frac{dV}{dt} - \frac{p_{I+1,J} - p_{I,J}}{dx}\,dV
\end{aligned}
$$

where $u_e = (u_{i,J} + u_{i+1,J})/2$, $u_w = (u_{i-1,J} + u_{i,J})/2$, $u_n = (v_{i+1,J} + v_{i,J})/2$ and $u_s = (u_{i,J-1} + u_{i+1,J-1})/2$. The control volume size is defined as $dV = \delta x\, \delta y$. For v coefficients, we must use the equivalent expressions.

For the *time integration scheme*, we shall use a complete implicit method, expressed as:

$$
\frac{d\phi}{dt} = \frac{\phi^{n+1} - \phi^n}{dt} = f\left(t_{n+1}, \phi^{n+1}\right) \tag{2.7}
$$

where ϕ is a variable obtained through the discretised transport equations at the current time n and at the following new time $n+1$, considering the time step dt. This implies that a system of algebraic equations must be solved at each time level for each variable. For our code, time marching starts at a given initial velocity and pressure field. The system of equations has to be solved with the selected dt. The next solution for u, v and p is assigned as the former values, and the procedure is repeated to progress the solution by a further time step until the selected elapsed time is completed. Small time steps are needed to ensure the accuracy of results due the accuracy of the scheme is first order in time. This scheme was selected because of its robustness and unconditional stability.

2.1.3 Solid domain definition using a 'marking-cell' technique.

Many techniques have been developed to approximate solutions assuming a solid obstacle of a generalized (non-Cartesian) geometry present within the fluid domain. The internal cells and boundary cells for this 'sub-domain' receive a special discretisation, defined by the mark-cells variable. See figure 2.2.

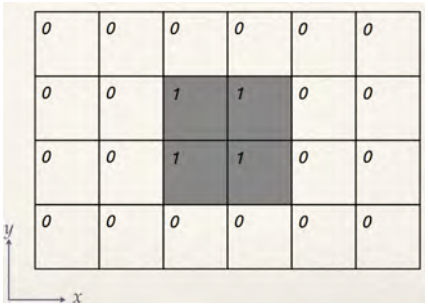

Figure 2.2. Control volumes as solid domains are identified with an index.

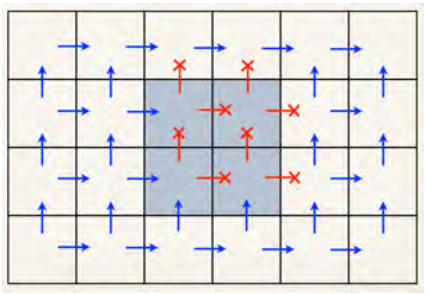

Figure 2.3. Velocities for marked cells are cancelled.

This means that any 'marked' and/or adjacent control-volume cells relative to this sub-domain will receive a particular formulation. Thus, selected cells are subject to either velocity nullification (figure 2.3) or correction for u and v, considering the staggered grid.

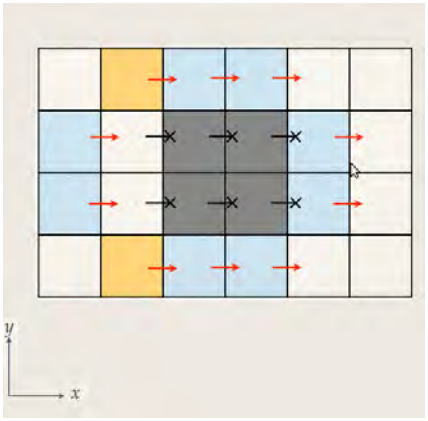

Figure 2.4. Correction in u velocity component because internal boundary effect.

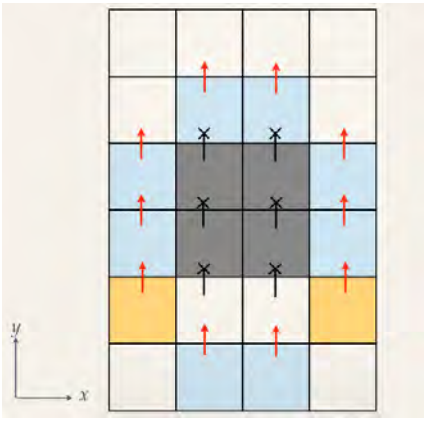

Figure 2.5. Correction in v because internal boundary effect.

According to equation 2.6 , corrections at the boundaries are defined as follows: For u velocity over adjacent control volumes of mark_cell(i,j) shown in figure 2.4 the corrections are,

At east face (west of body): $a_P\phi_P = (S_P + a_E u_{(i+1,j)})$
At west face (east of body): $a_P\phi_P = (S_P + a_W u_{(i-1,j)})$
At north face (south of body): $(a_P + a_N)\phi_P = (S_P + 2a_N u_{(i,j+1)})$
At south face (north of body): $(a_P + a_S)\phi_P = (S_P + 2a_S u_{(i,j-1)})$
Inside of body: $(\delta V/\delta t)\phi_P = (\delta V/\delta t)u_{(i,j))}$

For v velocity over adjacent control volumes of mark_cell(i,j) shown in figure 2.5 the corrections are,

At east face (west of body): $(a_P + a_E)\phi_P = (S_P + 2a_E v_{(i+1,j)})$
At west face (east of body): $(a_P + a_W)\phi_P = (S_P + 2a_W v_{(i-1,j)})$
At north face (south of body): $a_P\phi_P = (S_P + a_N v_{(i,j+1)})$
At south face (north of body): $a_P\phi_P = (S_P + a_S v_{(i-1,j-1)})$
Inside of body: $(\delta V/\delta t)\phi_P = (\delta V/\delta t)v_{(i,j))}$

2.1.4 Graphical representations.

Some results are presented as vorticity isolines and streamlines. Vorticity for the 2-Dimensional problem of solving N-S equations are used to show results, and it is defined as:

$$\omega = |\omega| = |\bigtriangledown \times V| = \frac{\partial v}{\partial x} - \frac{\partial u}{\partial y} \tag{2.8}$$

The stream function definition is $\frac{\partial \psi}{\partial y} = u$ and $\frac{\partial \psi}{\partial x} = -v$. Then by means of eq. 2.8, the Poisson equation for the ψ variable can be written as,

$$\bigtriangledown^2 \psi = \frac{\partial^2 \psi}{\partial x^2} v + \frac{\partial^2 \psi}{\partial y^2} = -\omega \tag{2.9}$$

2.2 Programming algorithm for basic geometry.

A code was written for solving the problem of interest by using FORTRAN. Before engaging in its solution, it is necessary to make some validations so that the given solution complies with physics. The validation of the results was done by using an immersed regular-geometry and was later compared to well-validated experimental data.

2.2.1 Flow behind a cylinder.

To validate the code used, a flow around a square and circular cylinder was chosen. As shown in figure 2.6, the wake behind a cylinder should become unstable beyond $Re \approx 40$

and therefore a slow oscillation begins. As vortices of opposite circulations are shed off alternately from the two sides, the circulation around the cylinder changes its sign, resulting in an oscillating lift or lateral force.

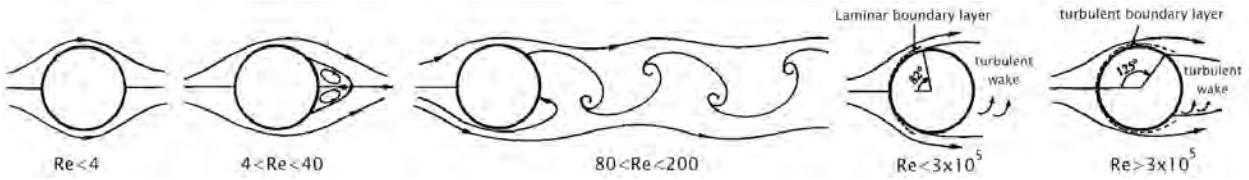

Figure 2.6. Some regimes of flow over a circular cylinder.

The passage of regular vortices causes velocity measurements in the wake to have a dominant periodicity. The frequency is expressed as a nondimensional parameter known as Strouhal number which is commonly used as a measure of the predominant shedding frequency f_s. The definition is $St = f_s D/U_\infty$ where D is the diameter of the circular cylinder (characteristic length) and U_∞ the freestream velocity.

The strategy used for Strouhal number computation is as follows: In order to obtain the Strouhal number for a particular flow condition over a temporal development, the following steps must be taken[34]. First the total force exerted over all the immerse body must be evaluated, integrating the pressure (p) and the wall shear stress (τ) over the 2-D geometric surface.

$$\overrightarrow{F} = \oint_{geom} pds + \oint_{geom} \tau ds \tag{2.10}$$

where the variables are nondimensional. Observe that the non-dimensional expressions for shear stress is defined by:

$$\tau = \frac{1}{Re}\frac{\partial u}{\partial y} \tag{2.11}$$

2.2.2 Squared cylinder as immersed geometry.

A square cylinder was first used as the immersed shape for testing the basic steps of the algorithm in the code. Depending on its positions, the discrete shear stress for each control volume is calculated by $\tau_x = \frac{1}{Re}\frac{du_{i,j}}{dy/2}$ and $\tau_y = \frac{1}{Re}\frac{dv_{i,j}}{dx/2}$ as seen in figures (2.7) and (2.8).

The x and y components of the force on the immersed boundary are,

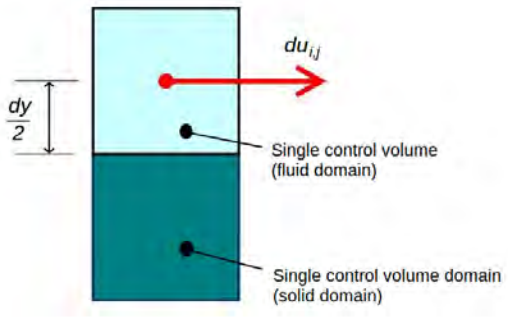

Figure 2.7. X-direction shear stress on control volumes.

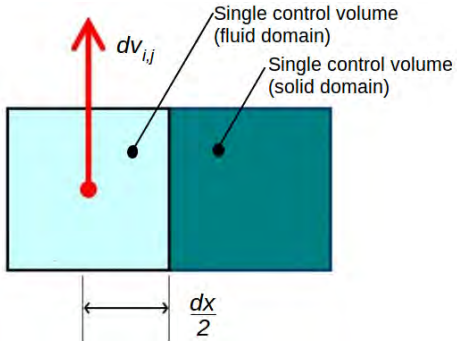

Figure 2.8. Y-direction shear stress on control volumes.

$$F_x = \oint_{geom} p_x ds + \oint_{geom} \tau_x ds \tag{2.12}$$

$$F_y = \oint_{geom} p_y ds + \oint_{geom} \tau_y ds \tag{2.13}$$

The manner in which both values are computed for this geometry, is as follows: We choose groups of control volumes depending on the force direction exerted with respect to the adjacent boundary. The direction of each force is selected as shown on figures (2.9) and (2.10).

Using this consideration we then define each group of control volumes for doing the sum of discrete values,

$$F_x = \left[\sum p_w dy + \sum p_e dy\right] + \left[\sum \tau_n dx + \sum \tau_s dx\right] \tag{2.14}$$

$$F_y = \left[\sum p_n dx + \sum p_s dx\right] + \left[\sum \tau_w dy + \sum \tau_e dy\right] \tag{2.15}$$

However, because,

$$\overrightarrow{F} = F_x \hat{\imath} + F_y \hat{\jmath} \tag{2.16}$$

and since the flow is moving in x direction, in this case:

$$F_D = F_x \qquad \text{and} \qquad F_L = F_y$$

Each of these correspond to both drag and lift forces which are frequently expressed as follows,

$$F_D = C_D \qquad \text{and} \qquad F_L = C_L \tag{2.17}$$

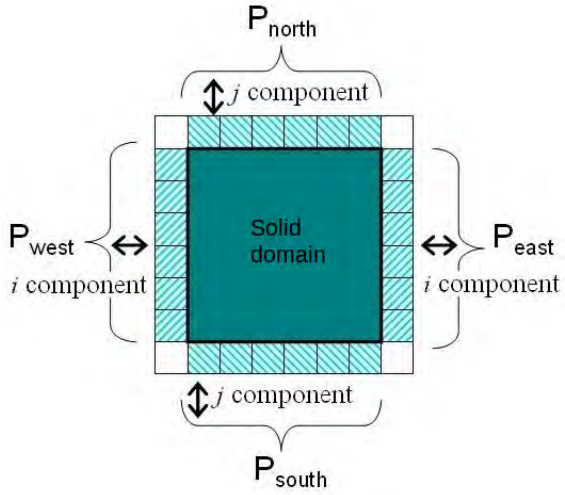

Figure 2.9. Selected control volumes for pressure integration.

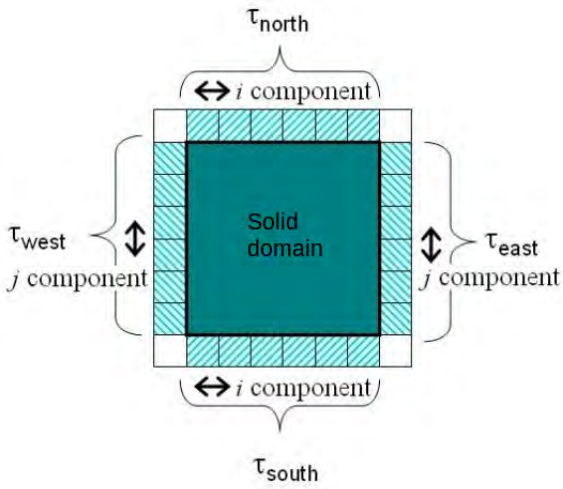

Figure 2.10. Selected control volumes for shear stress integration.

where C_D and C_L are the drag and lift coefficients.

Because of the wake activity, which is a repetitive production of asymmetric formation of vortices, a large amount of instantaneous lift forces will be created, producing mechanical vibration. The relevance of C_L is that from the temporal development of this value, we may obtain (via FFT) a characteristic non-dimensional frequency coming from wake formation behind the immersed body[34]. If the whole calculation is non-dimensional then the Strouhal number is given directly by $St = f_s$. This computation will be validated in Chapter 3 for a circular cylinder case.

2.2.3 Circular cylinder as an immersed geometry.

For a cylinder shaped geometry, the total force is obtained using a procedure similar to that described in the previous subsection. Firstly pressure and shear stress must be obtained over the corresponding control volumes in the fluid domain, adjacent to the solid control volumes.

In order to calculate the shear stresses, and thus the tangential forces, we take the following steps: The horizontal and vertical components of the velocity are evaluated at the nearest node to the immersed geometry. This is done by averaging the velocity components of the nearest nodes. Velocities $u(i,j), u(i-1,j)$ are averaged, as well as $v(i,j), v(i,j-1)$. This procedure is illustrated in figures (2.11) and (2.12) for u and v respectively.

The resultant velocity vector $\vec{u}_R$ is calculated from such averages on the nodes of each

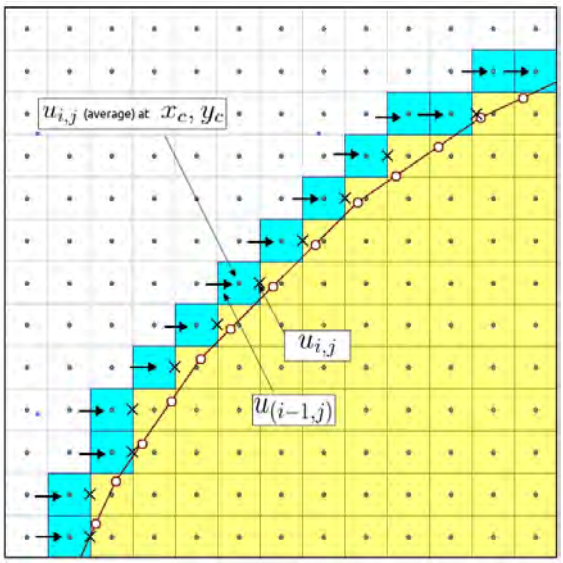

Figure 2.11. Interpolation of the u velocity. Selected control volumes for $\bar{u}$ velocity near cylinder boundary on x_c, y_c.

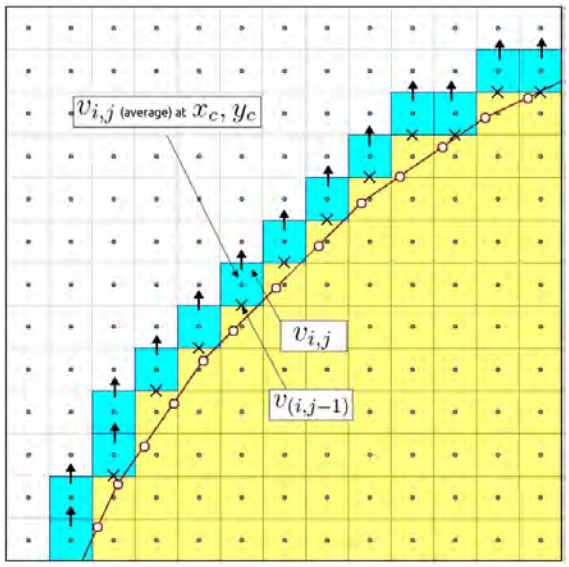

Figure 2.12. Interpolation of the v velocity. Selected control volumes for $\bar{v}$ velocity near cylinder boundary on x_c, y_c.

control volume at the boundary, as shown in figure (2.13). The forces on the boundary can be calculated by decomposing this resultant velocity vector $\vec{u}_R$ into its normal and tangential components relative to the body surface, i.e.:

$$\vec{u}_R = (u_n, u_T) = u_n\hat{\mathbf{n}} + u_T\hat{\mathbf{T}}$$

where $\hat{\mathbf{n}}$ and $\hat{\mathbf{T}}$ are unit vectors in the normal and tangential directions. Thus: $\vec{u}_T = \vec{u}_R - u_n\hat{\mathbf{n}}$, where $u_T = |\vec{u}_T|$.

The shear stress is computed as follows: We define a Cartesian coordinate system where u_x is a parallel velocity. In this axis of coordinates, the definition of shear stress is: $\tau_{ij} = \mu\frac{\partial u_i}{\partial x_j}$, where (i, j) are refered to the relative reference frame. Once we have defined boundary cells and marked cells, we interpolate the velocity in the boundary cell nodes considering that the velocity in the cell face next to the boundary is zero. These interpolations are u, v components at the nodes. Now, we define the unit normal vector as:

$$\vec{r} = \frac{\vec{p} - \vec{c}}{|\vec{p} - \vec{c}|}$$

where $\vec{p}$ and $\vec{c}$, and are the position vectors of the node and the center the circle respectively. The normal and tangential components of the velocity $\vec{u_R}$ are: $\vec{u}_{\hat{\mathbf{n}}} = \vec{u}_R \cdot \vec{r}$ and $\vec{u}_T = \vec{u}_R - \vec{u}_{\hat{\mathbf{n}}}$. The shear stress is then:

$$\tau = \frac{1}{Re}\frac{\partial u_T}{\partial n} \approx \frac{1}{Re}\frac{\Delta u_T}{\Delta n} = \frac{1}{Re}\frac{u_T^{node} - u_T^{circle}}{r_{ij} - r_{circle}} \tag{2.18}$$

where $u_T^{circle} = 0$, because we are considering a no slipping condition between a viscous flow and a rigid body. The difference $r_{(i,j)} - r_{circle}$, where $r_{(i,j)} = \sqrt{(x^2_{c(i,j)}) + (y^2_{c(i,j)})}$, and $x^2_{c(i,j)}$ and $y^2_{c(i,j)}$ are the coordinates of the control volume centres, and r_{circle} is the actual circle radius.

Once we have the stress tensor, the tangential force can be calculated with the expression $F_\tau = \tau_{ij} A_{ij}$, where the area A_{ij} is the perimeter fraction that corresponds to the node (i, j). The tangential force vector $\vec{F}_T$ in its Cartesian components by projecting in the x and y directions. This is illustrated in figure 2.14. In the code, we use each vector $\vec{u}_T$ to obtain τ on each boundary cell, and then each corresponding $\vec{F}_T$. Then, we decompose these in x, y components, to finally integrate them for obtaining total $\vec{F}_x$ and $\vec{F}_y$ derived from shear stresses.

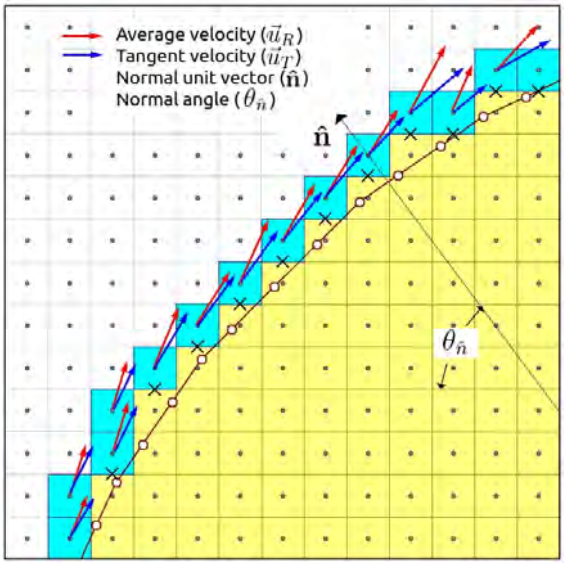

Figure 2.13. Computation of tangent velocity vector $\vec{u}_T$ from resultant velocity vector $\vec{u}_R$ and $\hat{\mathbf{n}}$ near boundary.

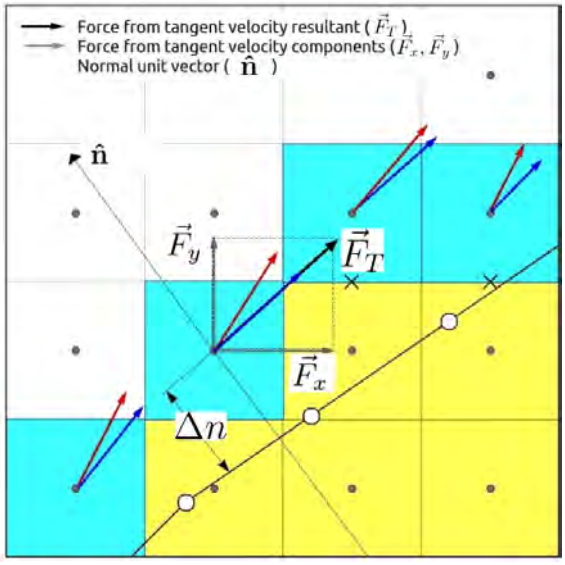

Figure 2.14. Shear stress forces decomposed on $\vec{F}_x$ and $\vec{F}_y$ components for a boundary cell (blue).

For computing the force derived from pressure, a similar but simpler procedure was taken. In this case, we know that $F_p = p_{ij}\, A_{ij}$. We already established that A_{ij} is the proportional fraction of circumference according to the total number of control volumes surrounding the immersed object (see figure 2.15) and defined as $A_{ij} = \frac{2\pi r_{circle}}{ncv_{bound}}$, which is a simplified computation method but what might carry out an error for certain sections around the circumference.

The magnitude $p_{i,j,}$ was computed on each boundary cells while converging the solution for all the fluid domain on every control volume centre, so interpolation is not required. Each one of these F_p must be normal to the surface of the cylinder, and decomposed as well in x, y components as shown in figure (2.16), and lastly, they should be integrated according to eq. (2.12) and (2.13) with the goal of obtaining $\vec{F}_x$ and $\vec{F}_y$ due to pressure. The sum of both x, y pressure and shear stress forces will result in C_D and C_L respectively.

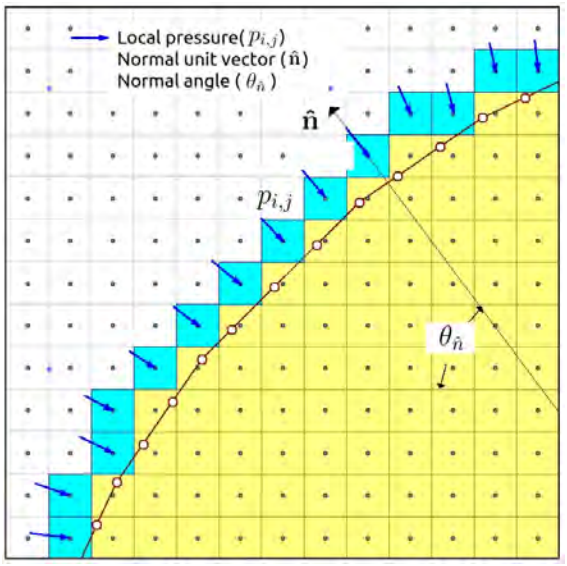

Figure 2.15. Local pressure $p_{i,j}$ on boundary cells (blue). Normal vector $\hat{\mathbf{n}}$ shows force $\vec{F}_p$ direction.

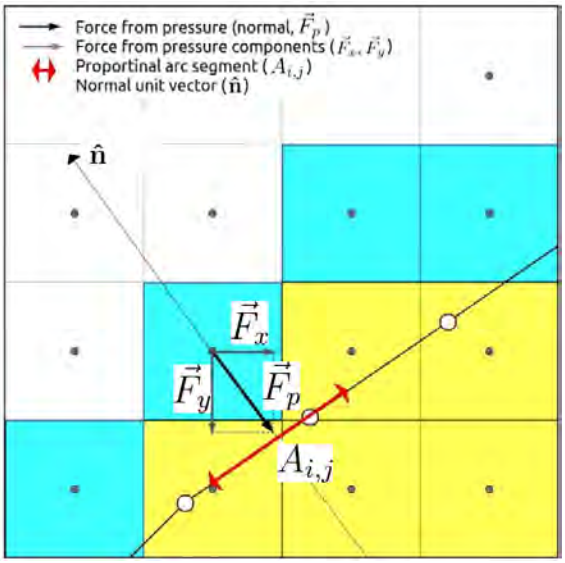

Figure 2.16. Pressure forces decomposed on $\vec{F}_x$ and $\vec{F}_y$ components for a boundary cell (blue).

2.3 Square cylinder validation.

One of the most important problems in CFD is having and incompressible fluid flowing around a square cylinder with a square cross-section confined in a channel. In this example, we can see the effect of wall confinement on flow field characteristics like flow separation, periodicity and vortex street formation. Among the most important advantages of the problem are its simplicity and the fact that flow separation points are fixed. The geometrical situation is sketched in figure 2.17. At low Reynolds number flow is laminar, steady and attached to the square cylinder. As Reynolds number increases the flow separates, but remains laminar. Beyond $Re = 50$, unsteadiness develops and flow becomes periodic. Localized regions of high vorticity are shed alternatively from either side of the cylinder and are

convected downstream. In the present example we validate the characteristic unsteady flow at $Re = 100$.

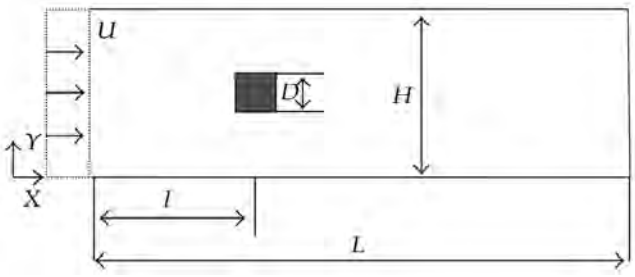

Figure 2.17. Diagram showing square-cylinder in the domain.

2.3.1 Inputs.

Initial conditions. The parameters used in the example are taken from satisfactory results of previous publications available in the literature. The main parameters are: Domain total length (L), height (H), as well as blockage ($B = H/D$), where D is the side of the square, and L/D ratio[36]. The upstream length $l = L/4$ has been chosen from this study. The Reynolds number is the main parameter which governs the qualitative behaviour. The actual parameters are listed in tables 2.1 and 2.2.

Table 2.1. Settings for square cylinder computations.

Item	Inputs
Reynolds number	100
Inlet velocity	$u = 1.0$
Square size	$D = 1.0$
Square location	$l = 7.5$

Table 2.2. Time and convergence settings for square cylinder computations.

Parameter	Inputs
Time	300
Tolerance	$1e-5$
Itmax[a]	100

[a]Maximum number of iterations

It is pertinent to observe that if the analysis is transitory, we will have to make the analysis after a certain period of time from the start ($t = 0$) has passed and time independent flow has been achieved. So, we must ensure that the entire run time (time=itmax·dt)[1] exceeds this interval. The velocity at the entrance to the domain is declared as $u = 1.0$ at $t = 0$, and at the domain of the fluid should be $u = 0$. However, as a mathematical strategy, it has been

[1]Total elapsed run time equals to the maximum number of iterations multiplied by the time step.

given an initial value of $u = 1.0$ at whole the fluid domain looking to achieve steady-state in less iterations.

Space and time integrating schemes are defined in Table 2.3, as well as the selected velocity-pressure coupling formulation. No-slip boundary conditions ($u = 0$, $v = 0$) are used on the lower and upper walls of the channel and in the immerse object walls.

Table 2.3. Domain characteristics and schemes for square-cylinder validation

Feature	Setting
Grid type	Cartesian, structured
Domain size, $L \times H$	30×15
Number of nodes	750×375
Scheme	Central Difference.
Time scheme	Full Implicit
Formulation type	SIMPLEC
Boundary cond. on Top/Btm walls	No-slip

2.3.2 Results for flow past a square cylinder.

Results obtained from computations include the lift coefficient, drag coefficient and Strouhal number, and are presented in Table 2.4 and plotted in figure 2.18. In these graphs, sensitivity to input parameters are plotted, where a clear sensibility to time step dt as well as $u\ du/dt$ ratio is observed.

Table 2.4. *V*ariables and results for the square cylinder calculation.

Run	$nx \times ny$	dx, dy	dt	$u\frac{dx}{dt}$	$C_L\ avg$	$C_L\ rms$	$C_L\ peak$	C_D	St
1.	600×300	0.050	0.005	10.0	-0.0350	0.1135	0.1605	0.7891	0.0833
2.	600×300	0.050	0.004	12.5	-0.0316	0.1242	0.1757	0.7885	0.0667
3.	750×375	0.040	0.005	8.0	-0.0292	0.1475	0.2086	0.7930	0.0833
4.	1000×500	0.030	0.005	6.0	-0.0252	0.2330	0.3296	0.8001	0.0750
5.	750×375	0.040	0.0067	6.0	-0.0260	0.1287	0.1820	0.7909	0.1120
6.	750×375	0.040	0.008	5.0	-0.0250	0.1134	0.1604	0.7915	0.1330
7.	750×375	0.040	0.010	4.0	-0.0303	0.1036	0.1466	0.7936	0.1550

The root mean square (rms) and peak values are the most common mathematical method of defining amplitude of a sinosoidal waveform. For a sine wave, the rms value is 0.707 times

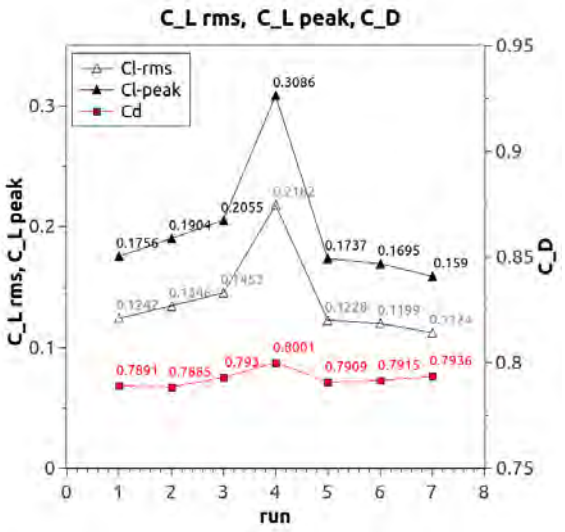

(a) C_L and C_D.

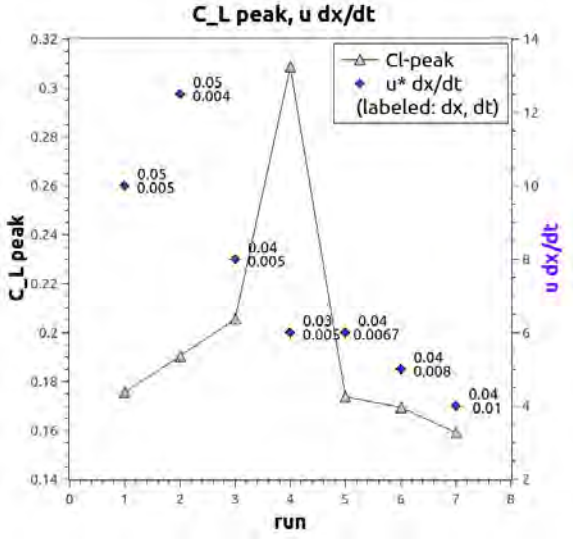

(b) C_L and udx/dt, according to table 2.4

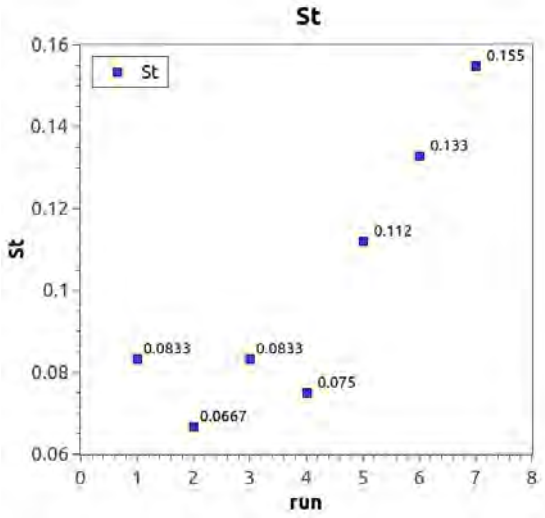

(c) *Strouhal number*, according to table 2.4

Figure 2.18. Flow over an square cylinder at $Re = 100$. Different scenario plots according to table 2.4 Parameters: $nx = 750$, $ny = 375$, $tncv = 281,250$, $time = 300$, $tol = 1e-5$, $maxiter = 100$.

the peak value, thus in table 2.4, $C_L rms = \frac{1}{\sqrt{2}} C_L peak$. Results may be compared with the table of results 2.5.

The best values found for runs 5-7, were compared to published values given in reference [36]. Figure 2.19 shows the periodic time variation for the flow past a square cylinder, and thus lift coefficient C_L and drag coefficient C_D dependence of time. There was an expected behaviour of the periodic variation of lift and drag coefficient for different Re after $Re_{crit} \approx 54$ for the square case.

Table 2.5. Reported experimental-numerical reference values [36] [33].

Re	$C_{L,avg}$	$C_{L,peak}$	C_D	St
100	0.000	$0.087 - 0.158$	$1.38 - 1.52$	$0.130 - 0.150$

Looking at the results, it can be observed that, although the amplitude is almost the same for C_L for every run, different amplitudes are found for C_D numbers because this is influenced mainly by pressure distribution on the rear side of the square cylinder which is strongly influenced by the vortex shedding at the top and bottom sides of the cylinder.

The z-vorticity and pressure field output graphs are presented in figures 2.20 and 2.21; interaction between the square cylinder and top/bottom walls may be appreciated. We may see in the figure captions which variables are kept and which ones are changed.

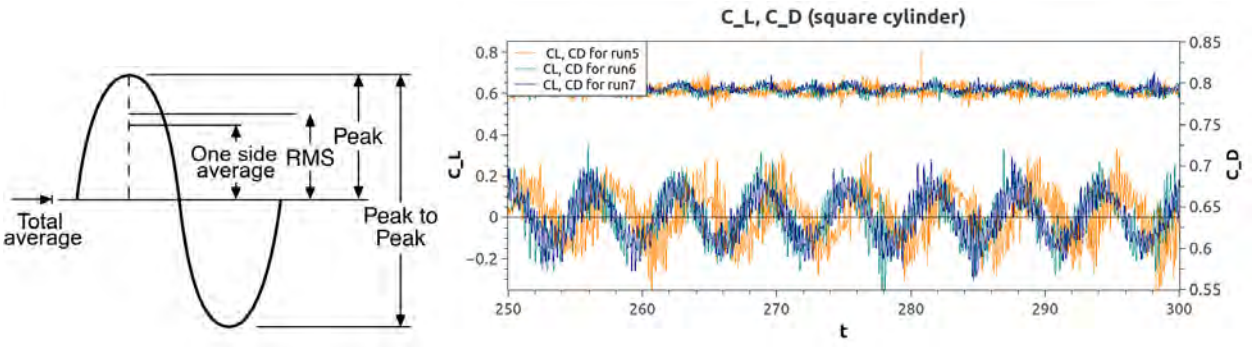

(a) Signal features. (b) Outputs signals for runs 5 (orange), 6 (cyan) and 7 (dark blue).

Figure 2.19. Flow over an square cylinder at $Re = 100$.

We may preliminarily conclude that C_L is inside the expected range of values, though not for the case of C_D that has an average error of 45%. Despite this we'll go on with our study, because our main parameter, the Strouhal number, is inside the range for runs *6* and *7*. We have found a proper independence between the internal-external interaction for certain domain sizes, allowing us to observe a proper development of the wake past the square cylinder

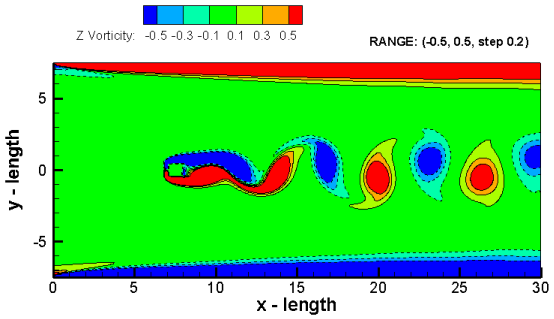

(a) z vorticity, range $(-0.5, 0.5)$ with 0.2 step using $dt = 0.0067$, $itmax = 44,776$, $udx/dt = 6.0$.

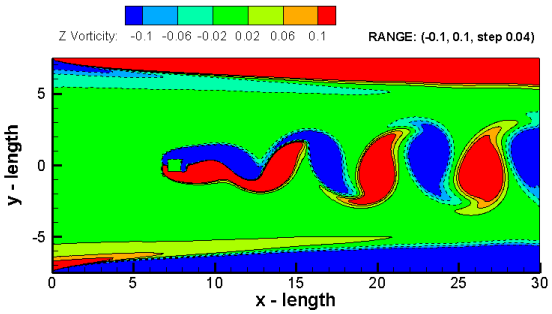

(b) z vorticity, range $(-0.1, 0.1)$ with 0.04 step using $dt = 0.0067$, $itmax = 44,776$, $udx/dt = 6.0$.

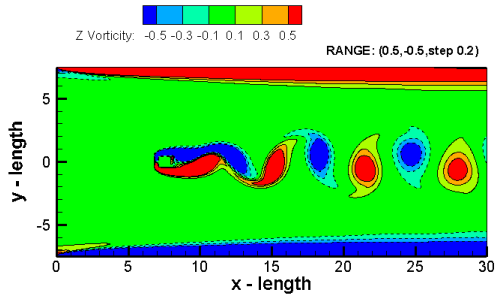

(c) z vorticity, range $(-0.5, 0.5)$ with 0.2 step using $dt = 0.008$, $itmax = 37,500$, $udx/dt = 5.0$.

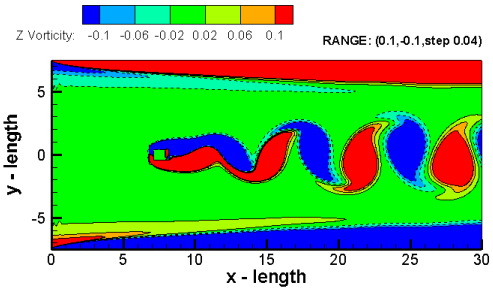

(d) z vorticity, range $(-0.1, 0.1)$ with 0.04 step using $dt = 0.008$, $itmax = 37,500$, $udx/dt = 5.0$.

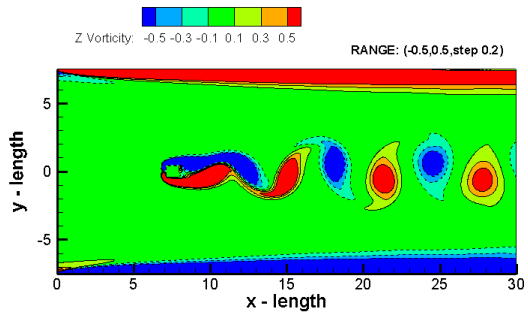

(e) z vorticity, range $(-0.5, 0.5)$ with 0.2 step using $dt = 0.010$, $itmax = 30,000$, $udx/dt = 4.0$.

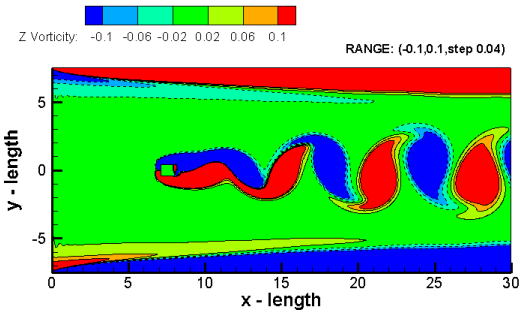

(f) z vorticity, range $(-0.1, 0.1)$ with 0.04 step using $dt = 0.010$, $itmax = 30,000$, $udx/dt = 4.0$.

Figure 2.20. z vorticity. Parameters: Re=100, nx=750, ny=375, tncv=281,250, dx=dy=0.040, time=300, tol=1e-5, maxiter=100.

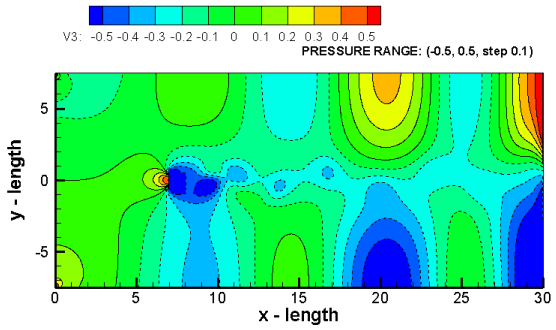

(a) Pressure, range $(-0.5, 0.5)$ with 0.1 step using $dt = 0.0067$, $itmax = 44,776$, $udx/dt = 6.0$.

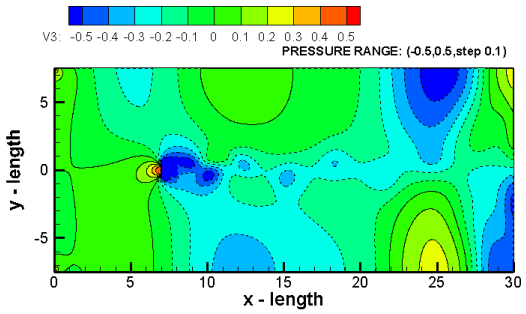

(b) Pressure, range $(-0.5, 0.5)$ with 0.1 step using $dt = 0.008$, $itmax = 37,500$, $udx/dt = 5.0$.

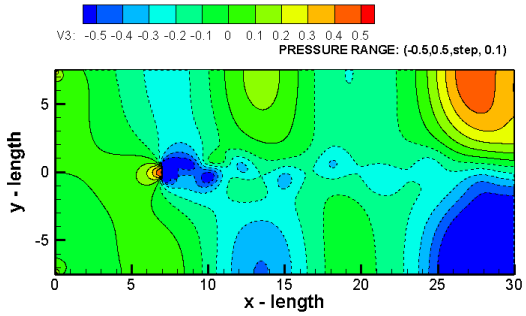

(c) Pressure, range $(-0.5, 0.5)$ with 0.1 step using $dt = 0.010$, $itmax = 30,000$, $udx/dt = 4.0$.

Figure 2.21. Pressure. Parameters: Re=100, nx=750, ny=375, tncv=281,250, dx=dy=0.040, time=300, tol=1e-5, maxiter=100.

with good Strouhal number proximity.

2.4 Circular cylinder validation.

In this section we will analyse the flow around a circular cylinder in steady and unsteady flows. A rectangular domain was used to simulate the flow over this stationary cylinder. Aerodynamic responses have been found and assessed, C_D, C_L and St outputs were found after transient variation. Additionally, flow characteristics such as velocity and pressure field, as well as normal and tangential stresses at the boundary of the cylinder were depicted.

2.4.1 Geometrical and numerical parameters.

A rectangular domain with respect to an aspect ratio L/H, and an immersed circular cylinder with a diameter D, symmetrically located in the vertical direction and at a distance l from the inlet was considered, similar to the previous case. The domain is discretised with a Cartesian structured grid of $nx \times ny$ nodes. See figure 2.22.

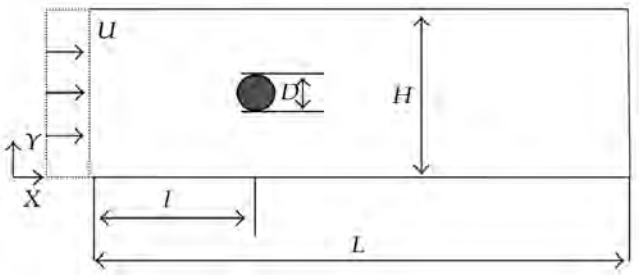

Figure 2.22. Diagram showing circular-cylinder in the domain.

The central difference discretisation strategy is used for the space derivatives, and the time integration is made with implicit scheme. As explained in the previous chapters, the pressure linked equations are solved with the SIMPLEC iterative algorithm. See Table 2.6 and Table 2.7.

Table 2.6. Conditions for the validation of the circular cylinder numerical solution.

Item	Input
Grid type	Cartesian, structured
Scheme	Central difference
Inlet boundary cond.	Dirchlet
Outlet boundary cond.	Neumann
Time scheme	Implicit
Formulation type	Simplec

2.4.2 Initial and boundary conditions.

The initial conditions used for velocity are in the whole domain. An axial constant velocity $u = 1.0$ and zero transversal velocity $v = 0$ are assumed for the inlet boundary (Dirichlet condition), and a zero axial gradient for the axial velocity $\partial u/\partial x = 0$ and zero transversal velocity $v = 0$ are considered for the outlet boundary (Neumann condition). A no-slip boundary condition is assumed for the cylinder (inner boundary) and two types of boundary conditions are used for the lateral walls: slip and non-slip conditions.

For this section, a set of *17* computation run scenarios are explained:

- Scenarios *1-7* are listed in the Table 2.7 as a first approach using different Re values. The first seven runs are intended to show qualitative behaviour of the response, outputs such as periodicity that starts at specific Reynolds numbers, looking for vortex shedding and St-Re relationship. These vortices develop and remain attached to the cylinder up to $Re_{crit} \approx 47$. Numerical convergence is monitored as well.

- Scenarios *8-11* were run with $Re = 100$ using different numerical parameters, recording peak lift coefficients ($C_{L,peak}$), drag coefficients (C_D) and Strouhal numbers (St) as indicators were made in order to test the numerical convergence and error reduction.

- Scenarios *12-17* were tested at different Re values and listed at Table 2.7, showing the output summary for these cases in Table 2.10, where we are looking to obtain Strouhal values and other main indicators for selected parameters.

Table 2.7. Input summary for the circular cylinder scenarios approach.

Run	Re	D	l *size*	*Domain*	$nx \times ny$	dx, dy	dt	*time*	$itmax$[2]	*tolerance*	$maxiter$[3]
1.	1	0.47	1.0	6×2	300×200	0.010	0.100	100	$1,000$	$1e-4$	80
2.	40	0.47	1.0	6×2	300×200	0.010	0.100	100	$1,000$	$1e-4$	80
3.	80	0.47	1.0	6×2	300×200	0.010	0.100	100	$1,000$	$1e-4$	80
4.	90	0.47	1.0	6×2	300×200	0.010	0.100	100	$1,000$	$1e-4$	80
5.	100	0.47	1.0	6×2	300×200	0.010	0.100	100	$1,000$	$1e-4$	80
6.	150	0.47	1.0	6×2	300×200	0.010	0.100	100	$1,000$	$1e-4$	80
7.	200	0.47	1.0	6×2	300×200	0.010	0.100	100	$1,000$	$1e-4$	80
8.	100	1.00	6.0	20×5	400×100	0.050	0.005	100	$20,000$	$1e-5$	100
9.	100	0.47	1.0	3×2	300×200	0.010	0.100	100	$1,000$	$1e-4$	80
10.	100	1.00	7.5	30×15	750×375	0.040	0.0067	300	$44,776$	$1e-5$	100
11.	100	1.00	7.5	30×15	750×375	0.040	0.010	300	$30,000$	$1e-5$	100
12.	60	1.00	7.5	30×15	750×375	0.040	0.008	300	$37,500$	$1e-5$	100
13.	80	1.00	7.5	30×15	750×375	0.040	0.008	300	$37,500$	$1e-5$	100
14.	100	1.00	7.5	30×15	750×375	0.040	0.008	300	$37,500$	$1e-5$	100
15.	120	1.00	7.5	30×15	750×375	0.040	0.008	300	$37,500$	$1e-5$	100
16.	160	1.00	7.5	30×15	750×375	0.040	0.008	300	$37,500$	$1e-5$	100
17.	200	1.00	7.5	30×15	750×375	0.040	0.008	300	$37,500$	$1e-5$	100

2.4.3 Results for flow past a circular cylinder (runs *1*-*7*).

In regards to the transient behaviour, we observe that our numerical integration strategy presents a large transient period. This is illustrated in figure 2.23 where the lift coefficient is plotted as function of time for different Reynolds numbers. All of the results shown in the following sections were obtained for steady flows when the transient behaviour died out.

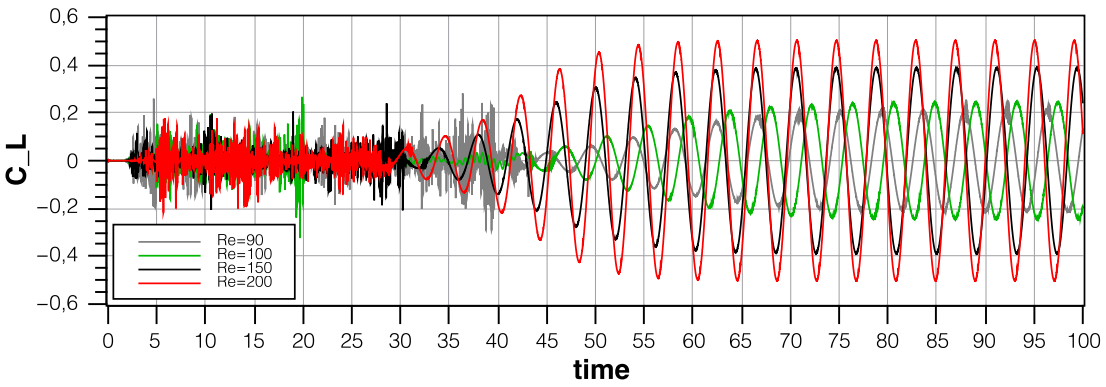

Figure 2.23. C_L as a function of time for different values of the Reynolds numbers: Re=90, 100, 150, and 200. Steadiness appears over $Re \approx 55$.

Theoretically, beyond a critical Reynolds number, unsteadiness develops and the flow becomes periodic. Graph Time-C_L for different Re for runs between $1 < Re < 80$ were discarded because no clear signals coming from the vortex shedding appeared in a Time-C_L graph, plotting only C_L patterns as time develops from $Re = 90$ up to $Re = 200$ at $t = 100$, as shown in figure 2.23. However, snapshots of streamlines around the circular cylinder for different Reynolds numbers are shown in figure 2.24, from (a) where we consider a Reynolds number equal to one at $t = 100$ to (e) $Re = 200$.

Notice that for $Re = 1$ the streamline distribution practically coincides with the one of an ideal fluid. As we can see in graph (b), at $Re = 40$, flow separates fully and two symmetrical vortices symmetrical appear behind the cylinder. Alternative behaviour from subsequent Reynolds numbers are presented at $t = 100$. One may observe how clear sinusoidal behaviour barely starts from $Re = 60$. Also, snapshots were taken along temporal evolution for $Re = 100$, at timesteps t=40, 60, 80 100 and 200 time units, as shown in figure 2.25 (a) to (e), where steadiness was achieved at $t \approx 55$, describing a time transient stage.

Unfiltered results for C_L and C_D graphs are shown in figures 2.26, and a sinusoidal pattern, which is a sign of a sustained vortex shedding process is observed. Figure 2.26 *(a)* shows C_L and *(b)* shows C_L for run *5*, both indicating that no steady state is observed after $t = 100$.

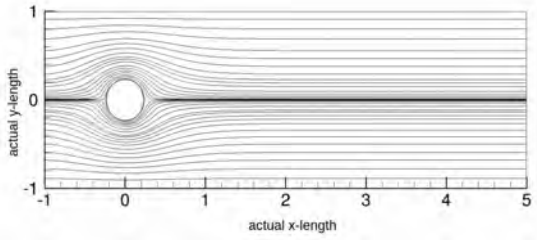

(a) $Re = 1$ at $t = 100$

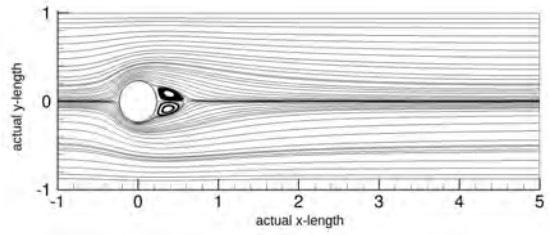

(b) $Re = 40$ at $t = 100$

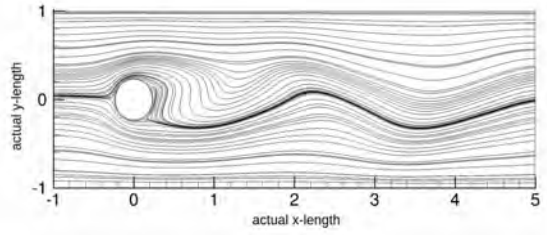

(c) $Re = 80$ at $t = 100$

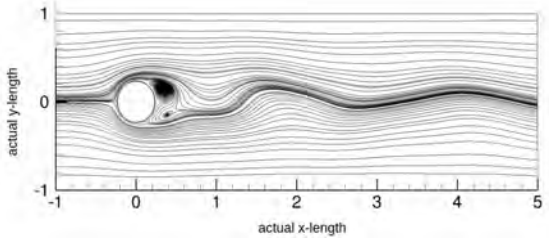

(d) $Re = 100$ at $t = 100$

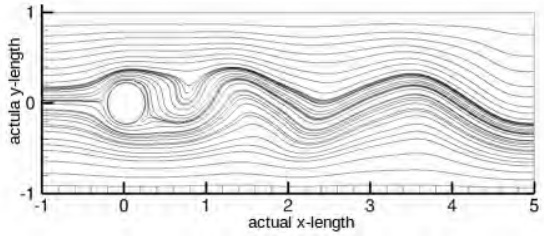

(e) $Re = 200$ at $t = 100$

Figure 2.24. Streamlines around a cylinder, t=100.

Averaged coefficients are time-averaged outputs obtained for each C_L and C_D instant value per its corresponding elapsed time, $C_{L,avg} = \sum_{i=1}^{t} \frac{C_{L,i}}{i\Delta t}$ and $C_{D,avg} = \sum_{i=1}^{t} \frac{C_{D,i}}{i\Delta t}$, being t the total time units at $t = 100$, and starting to register from a proposed $t_{steady} = 0.5$ time. The graph shows the assumption that the transient stage ends at $t \approx 0.5$. Results are shown in figures 2.27 *(a)* and *(b)* using run *5*. An important number to observe is the Courant number (C), which is defined for a two-dimensional case as $\mathrm{C} = u_x \frac{\Delta t}{\Delta x} + u_y \frac{\Delta t}{\Delta y} \leq \mathrm{C}_{max}$. The value of C_{max} changes with the method used to solve the discretised equation, especially depending on whether the method is explicit or implicit. If an explicit (time-marching) solver is used then typically $\mathrm{C} < 1$. Implicit (matrix) solvers are usually less sensitive to numerical instability and so larger values of C may be tolerated. The Courant-Friedrichs-Lewy (CFL) condition indicates stability for the numerical solution, but not convergence. The Courant number will be frequently used as a reference parameter in this work.

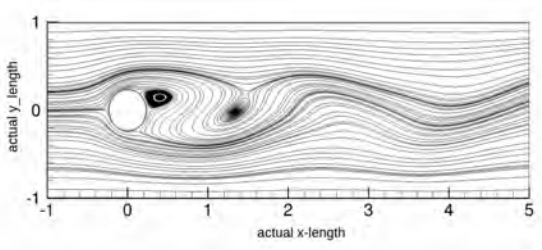

(a) $Re = 100$ at $t = 40$

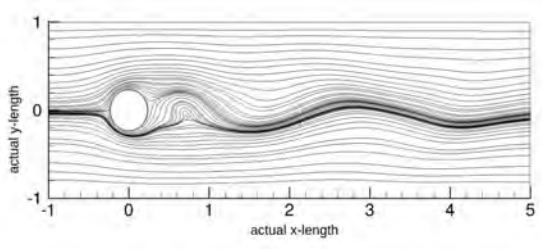

(b) $Re = 100$ at $t = 60$

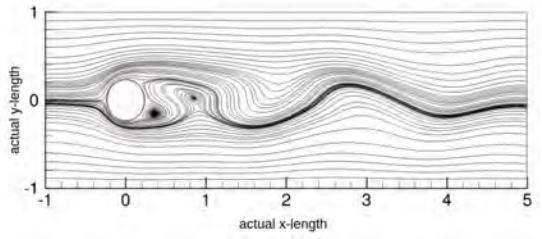

(c) $Re = 100$ at $t = 80$

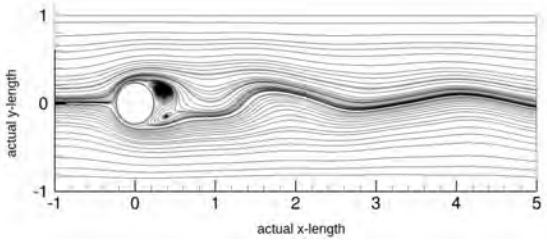

(d) $Re = 100$ at $t = 100$

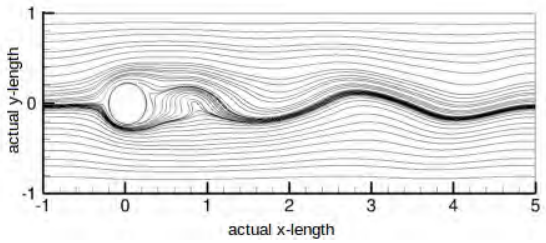

(e) $Re = 100$ at $t = 200$

Figure 2.25. Streamlines around a cylinder, Re=100

Applying a Discrete Fourier Transformation (DFT) to the C_L signal shown in figure 2.26 (a), we obtain a singular response computed with a Fast Fourier Transform (FFT) algorithm. See figure 2.28. If noise is present in raw-data, a local regression using weighted linear least squares and a 2^{nd} degree polynomial model (matlab's loess command) may be applied to selected steady data (starting at a proposed steady time) to filter and compare it, as shown in figure 2.29 (a). A clear sinusoidal behaviour is shown after treatment but this smooth data is useful just as a demonstration, and is not required for obtaining a latter f_s (as we can see in figure 2.29 (b)) where both curves are superimposed.

These sets of data were useful for obtaining a dominant frequency, as we can see in figure 2.28 using inputs from Table 2.7, and from a clean signal shown in figure 2.26. Figure 2.29 (b) shows the f_s found with this method. A brief summary of results are shown in Table 2.8.

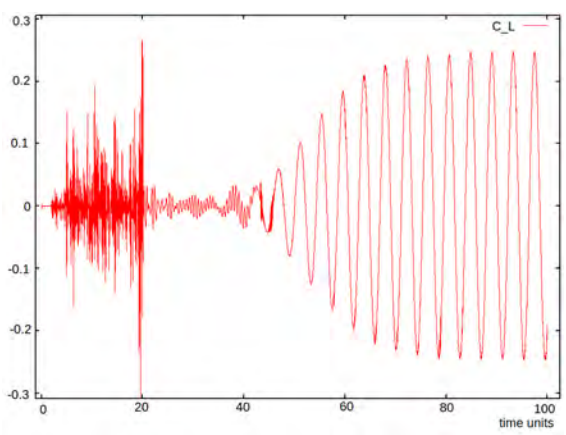

(a) time-C_L graph.

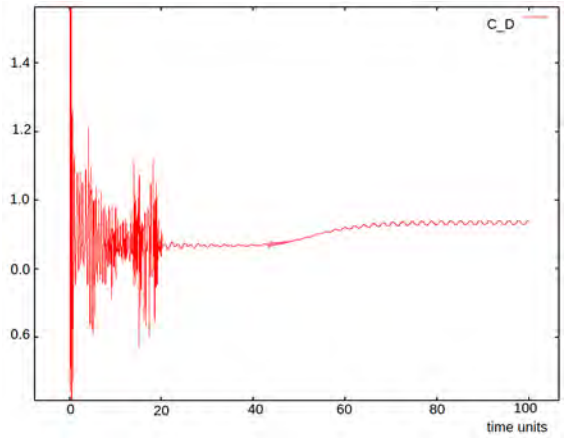

(b) time-C_D graph.

Figure 2.26. First results of lift and drag coefficients evolution in time using Re=100.

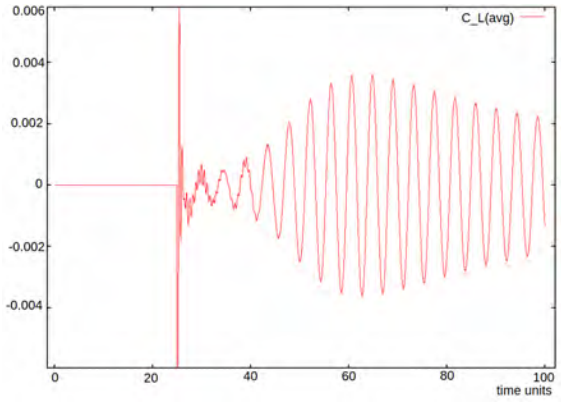

(a) time average-C_L graph.

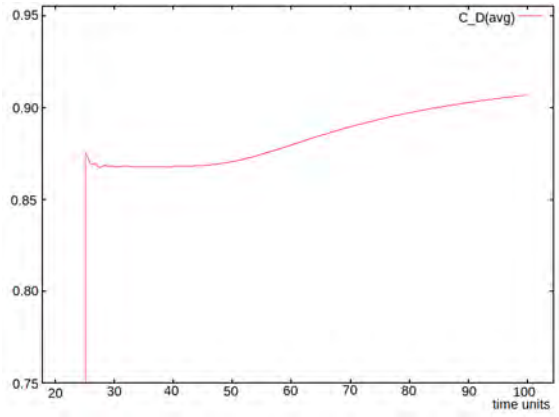

(b) time average-C_D graph.

Figure 2.27. Time averaged lift and drag coefficients using Re=100.

Comparing the pressure distribution to an ideal flow we can see that ideally around the surface of a circle is $C_P = 1-(\frac{w_k}{U_\infty})^2 = 1-4sin^2\varphi$, where φ is the angular coordinate that goes from 180° at the front to 0° to the rear of the cylinder. This expansion displays a symmetric behaviour of the pressure coefficient on the cylinder surface, defined as $C_P = p - p_\infty$, as a function of the angle φ[39]. We can see a natural discrepancy at the rear side if we compare figures 2.30 (a) C_P obtained for an ideal flow around circle (dotted line) and (b)experimental (broken line). Finally, 2.30 (c) is the result of the present work (continuous line) using run *5*.

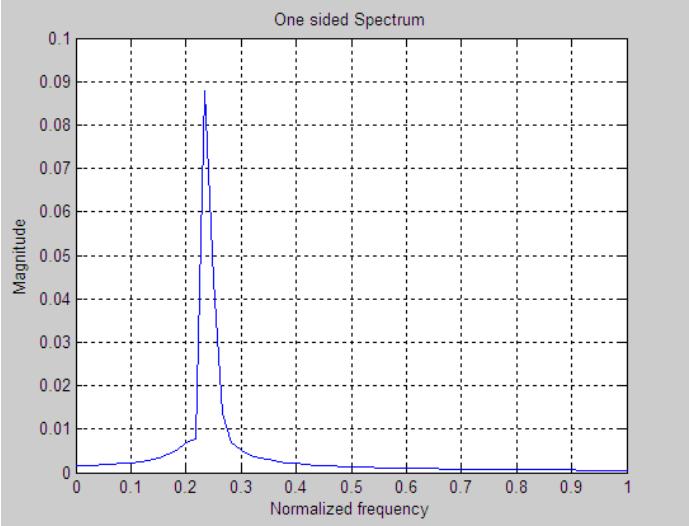

Figure 2.28. FFT graph from $t - C_L$ data.

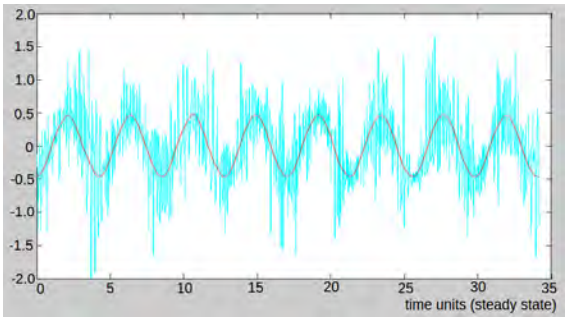

(a) Output from raw data and filtered signal using matlab's rloess.

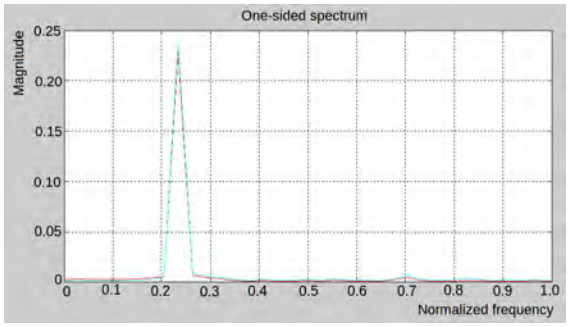

(b) Characteristic frequency after DFT of both signals.

Figure 2.29. Output from raw data and frequency after DFT.

Regarding the physical conditions at the cylinder surface, we recall that the distance over which the viscous forces have an effect is termed the boundary layer thickness. The magnitude of shear stress that manifests itself in the boundary layer is given as function of the polar angle. We can see in 2.30 (b), how shear stress force F_{ss} decays at $\varphi \approx 80°$ attributed to boundary layer separation. Though our boundary layer may be called artificial due it consists basically of an interpolation, we have some characteristics that complies with it like the following[11]:

Table 2.8. Results for cylinder for run 1 validation

Item	Constant
CLF (sum of max.$x-y$ values)	0.313
C_l, average	0.000
C_d, average	0.905
$St = f_s$	0.233

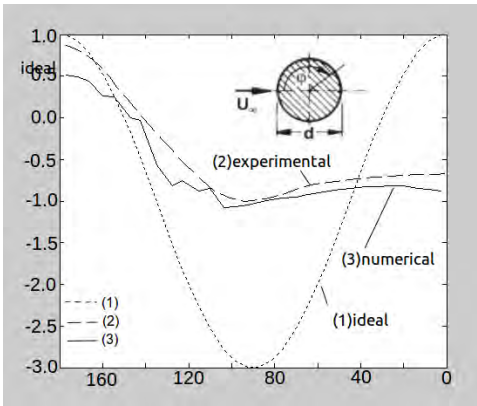

(a) Comparison between C_P ideal flow around circle (1,dotted line), experimental (2, broken line) and present work result(3, continuous line).

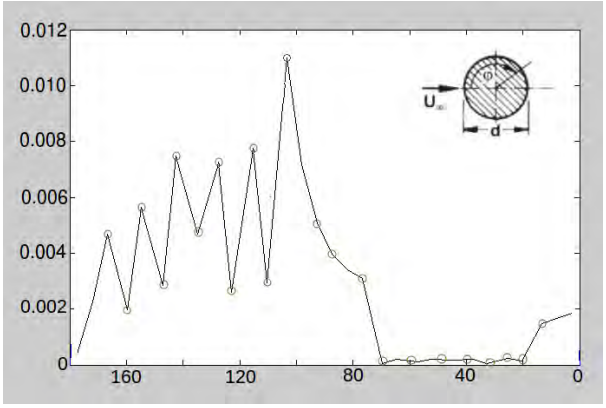

(b) Force magnitude for shear stress-angle ($\varphi - F_{ss}$). If Re increases, the separation point of the BL moves to lower values of φ.

Figure 2.30. Comparison of C_P for ideal, experimental and present work. Re=100.

- The velocity decreases to zero at the region closest to the wall. An originally laminar flow is affected by the presence of the walls.
- Most of the flow is unaffected by the presence of the circular cylinder. The flow away from the object can be treated as inviscid, and can sometimes be approximated as potential flow.
- The thickness is a function of the ratio between the inertial forces and the viscous forces, i.e. the Reynolds number. As Re increases, the thickness decreases. The region near the wall where the viscous forces are of the same order as the inertial forces. We will observe this point in further tests.

The separation of the boundary layer is an undesired event because it increases the drag C_D. For the present work, a precise computation of thickness will not be performed, but separation points are assumed to be well located. When Re increases, the separation point

of the boundary layer moves to lower values of θ, reaching a minimum value of about 80° from the front stagnation point. The furthest the point of separation of the rear stagnation, the greater the drag. On the validation results some of these characteristics are present, e.g. 2.30 *(b)* shows a shear stress force graph respect to the angle on half the circumference on control volumes next to the solid body, according to the monitor. It can be said that a sudden fall of velocity and thus shear stress-force shows a clear evidence of flow separation.

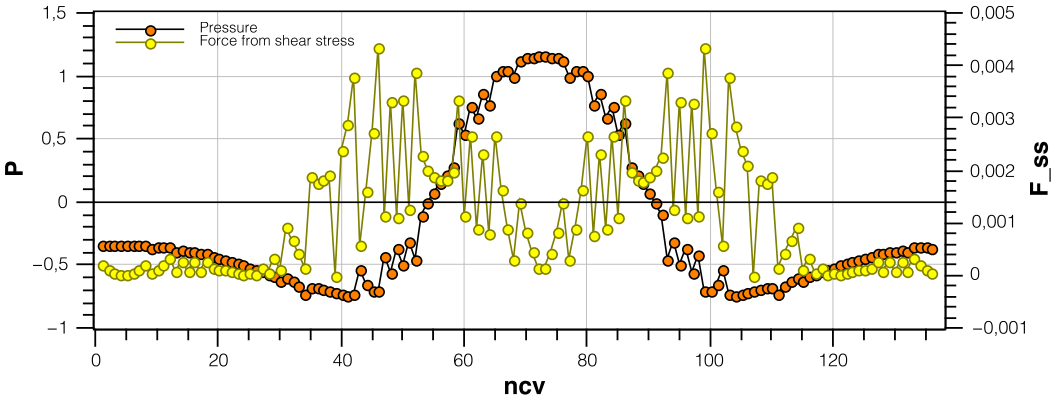

Figure 2.31. Pressure and shear stress around circular cylinder.

Using the input corresponding to run *9* in Table 2.7, in figure 2.31, both pressure distribution and shear stress around the cylinder are shown. A pressure maximum appears at the front stagnation point then the pressure reduces to minima near the top and bottom of the circular cylinder.

Numerical simulation shows that recirculation is occurring, which means two things: (1) A decrease in velocity is happening at the viscous layer due to its proximity to the non-slip condition of the immerse body, and (2), a prevalence of a pressure gradient against flow is occurring which is favouring to back-flow. Also, for run *9* inputs, two representations of control volumes at the boundary next to the body are shown in figures 2.32 (a) and (b). Here we can confirm graphically how pressure and tangent velocity is occurring at the very boundary, in magnitude and direction (normal and tangent respectively). Pressure scalar field is represented in figure 2.32 (c).

The results from the numerical solution concerning the force distribution i.e. pressure and shear stresses exerted over the solid body, coincide with the expected fields (*reference required*) but we consider we may go further on with other validation cases.

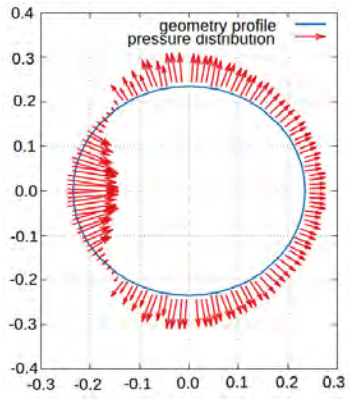

(a) Pressure distribution represented with vectors.

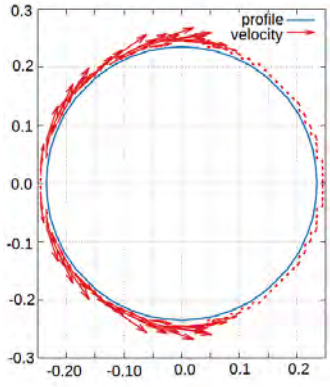

(b) Tangent velocities (shear stress) distribution represented with vectors.

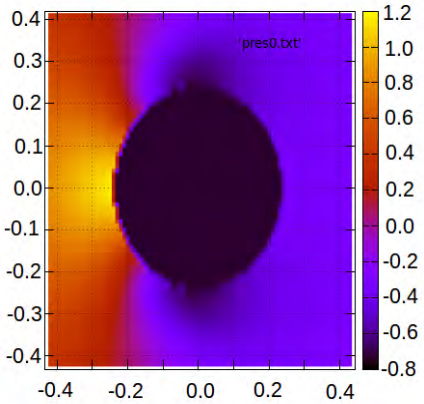

(c) Contour pressure field near circular cylinder.

Figure 2.32. Graphs for flow around a circle validating our code, with vector and contour plotting over the boundary control volumes in the fluid domain.

2.4.4 Results for flow past a circular cylinder (runs *8-17*).

After analysing the results, we conclude that the input parameters used in run *14* were the best combination of numerical parameters and computer time for our study. In order to obtain an accurate Strouhal number due alternating vortex shedding, a set of computations were made at $Re = 100$ that shares the domain size 30×15 (runs 10, 11 and 14). Results for these runs are shown in table 2.9. Sensitivity on $u\frac{dx}{dt}$ and dt is observed. The chosen run was *14* with non dimensionalized values ($D = 1.0$, $u = 1.0$), obtaining $St = f_s = 1/(\text{shedding cycle time}) = 0.1466$, for $Re = 100$.

Table 2.9. Results of the circular cylinder at $Re = 100$. N_{ncv} is the total number of control volumes in the domain.

Run	N_{ncv}	$u\frac{dx}{dt}$	C_L *avg*	C_L *rms*	C_L *peak*	C_D	St
8.	$40,250$	10.0	0.000	–	–	0.905	0.233
10.	$281,250$	6.0	–	0.1374	0.1943	0.6764	0.1218
11.	$281,250$	4.0	–	0.1335	0.1841	0.6759	0.1833
14.	$281,250$	5.0	–	0.1302	0.1888	0.6761	0.1466

Then, a final set of computational runs are $12 - 17$ from the table 2.7, were performed to obtain St at different Re values. This new set was arranged, using run *14* parameters, but at different Re according to Table 2.10.

Comparative results are shown in figure (2.33) with some numerical and experimental well documented values of previous works. We can see a trend obtained in the present work compared to documented references.

Over a period of 100 years, beginning with the vortex frequency measurements of Strouhal in 1878, there has existed a disparity of 20% among the many measurements of Strouhal number vs Reynolds number in the laminar shedding regime. Agreement to the 1% level of $St - Re$ relationship for laminar parallel shedding using different techniques are given in figure 2.33[44]. According to other sources, experiments show that for a circular cylinder the value is close to 0.21 for a large range of Reynolds number, including three dimensional instabilities.

Table 2.10. Variables and results for runs applied to the circular cylinder approach, $u\frac{dx}{dt} = 5.0$

Run	Re	C_L *avg*	C_L *rms*	C_L *peak*	C_D	St
12.	60	−0.0303	0.0762	0.1086	0.7190	0.1200
13.	80	−0.0303	0.1068	0.1511	0.6910	0.1333
14.	100	−0.0303	0.1335	0.1888	0.6761	0.1466
15.	120	−0.0303	0.1684	0.2382	0.6721	0.1466
16.	160	−0.0303	0.2222	0.3142	0.6732	0.1600
17.	200	−0.0303	0.2608	0.3689	0.6783	0.1600

For the circular cylinder case we can state that a qualitative well represented behaviour of the fluid was demonstrated for $Re < 2000$. The boundary layer separation and the recirculation behind the body was qualitatively well captured due the viscous effects noticeable on the deceleration of flow near the body and the presence of an adverse pressure gradient.

2.5 Summary and present work scope.

In this chapter we presented the description of a numerical code that successfully solves the conservation equations in fluid mechanics for an integration domain with internal boundaries. The solution method is based on the marking cells technique.

The results obtained indicate that most properties of the flow are in qualitative agreement with experimental observations. Some other properties like St(Re) function are predicted to be within 15% for Re<100.

Ideally, for the treatment of the numerical simulation of a viscous compressible flow over an airfoil problem, a non-rectangular domain grid is required to be wrapped around the airfoil. Continuity, momentum and energy equations have to be transformed into a new curvilinear

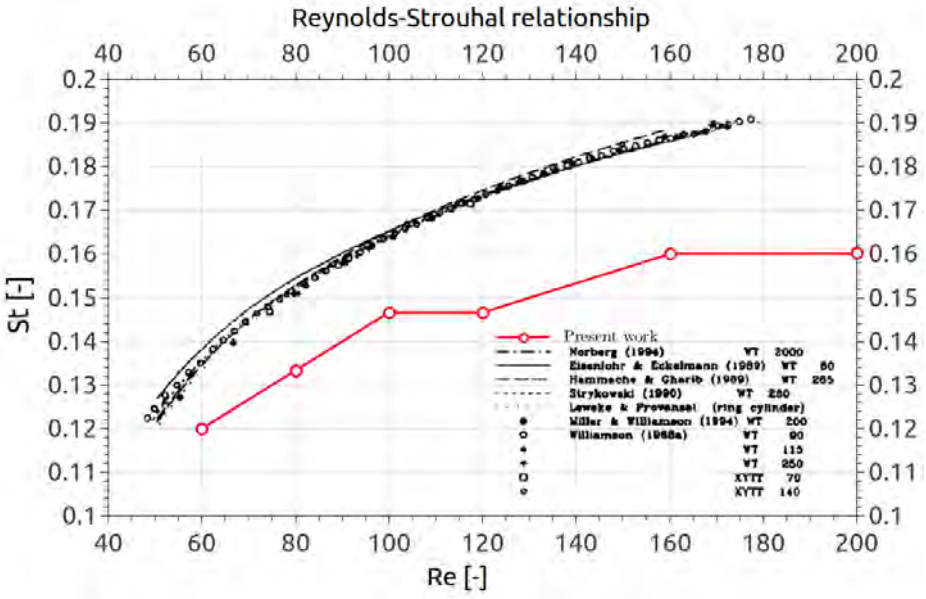

Figure 2.33. St-Re number relationship. Acronyms meaning, WT: wind tunnel facility; XYTT: a water facility known as the XY Towing Tank. The numbers indicate length/diameter ratio.

coordinate system. This treatment or a detailed explanation are beyond the scope of the present work.

Turbulent flow is also out of the scope of the present work though it is worth to be included in future development. Typical wind turbine performance situations take place in Re values between 10^5 and 10^6, thus the use of a turbulent model may be decisive for a blade design. It has been shown that for completely laminar flows, because of the peculiar aerodynamic properties of some low Reynolds number, flows may separate over airfoils.

To illustrate the importance of using a turbulence model, observe that although a laminar flow separates over the top and bottom surfaces of the airfoil, if a turbulence model is used for calculation, a remarkable difference presents with a flow completely attached, because turbulent flow resists separation much more than laminar flow [9].

The present work uses a finite volume method over a structured rectangular domain with the intention of demonstrating how far it is from real cases, while keeping certain characteristics valid or if it is a useful tool for calculating certain blade design features, though not for a detailed study at the physics of the boundary layer. This work is also a useful example for pedagogical purposes.

Chapter 3

Streamlined profile validation

3.1 Programming algorithms for a streamlined profile.

A similar procedure used for the squared and circular cylinder geometries will be applied for a streamlined body immersed within the flow, our main concern being the calculation of C_D and C_L. The design of a wind turbine blade, i.e. the proper cross section along its length must have a streamlined shape (if it is mechanically possible) with a specific tilted position in order to achieve optimal performance therefore, taking advantage of the forces which occur during the interaction between the fluid and body. The aerodynamic forces and moments on a body moving through a fluid or a fluid moving against a relative static body are due to the pressure and stress distribution over the body's surface.

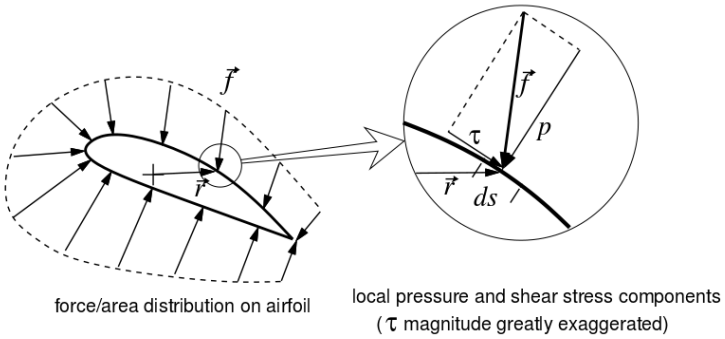

Figure 3.1. Resulting aerodynamic force exerted on an airfoil and its components.

Surface force distribution of the fluid flowing about the body exerts a local force-area $\vec{f}$ on each point of the body. Its normal and tangential components are the pressure p and the shear stress τ as shown in figure 3.1 [9] [31].

3.1.1 Algorithm for marking cells in the domain

Several steps were taken in order to compute C_D and C_L over an streamlined profile. The following list briefly describes each of them:

(i) Choice of online databases.

(ii) Read data and point addition.

(iii) Find aerodynamic center and rotation.

(iv) Select and mark cells of solid domain.

(v) Select boundary cells at fluid domain for monitoring.

(vi) Compute pressure at the boundary.

(vii) Compute shear stress at the boundary.

(viii) Compute of C_D, C_L, and lift-to-drag ratio.

Each item of this list is described in some detail, as follows:

(i) **Online databases.** A intermediate goal for the present project is to program a code capable of reading normalized $x-y$ data that describes an airfoil geometry. Several databases are available online. There are sites available in which a wide range of symmetrical, NACA 4, 5 or 6 digit airfoils database collection can be found.

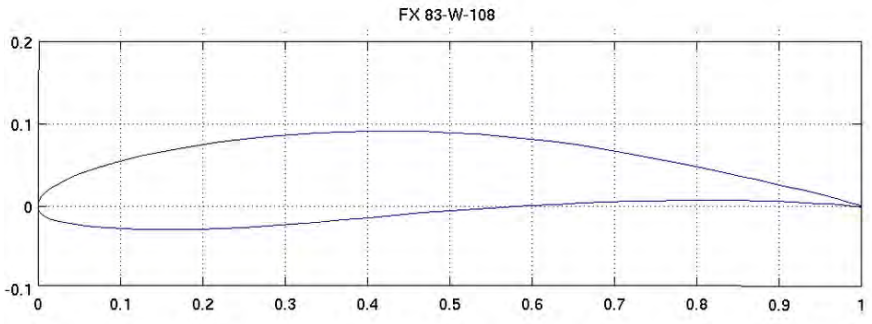

Figure 3.2. Airfoil Coordinates for NACA FX 83-W-108 obtained from downloaded database.

The sites contain detailed information like max-min percentage thickness or maximum percentage camber relative to the chord, generating x-y coordinates data files, etc. Also, the

Reynolds number range, turbulence level (N_{crit}) and maximum C_L/C_D are given in some sites. Default values of the pitch angle, camber radius or thickness may be modified and plotted for visualization. In figure 3.2, an example of an airfoil downloaded from UIUC site[6], which contains a wide range of coordinate databases is shown.

(ii) **Airfoil data reader and point addition algorithm.** Once data is downloaded, each point is located according to its x-y coordinates in an absolute Cartesian reference frame. Separation between points should be closer than the size of a single control volume, otherwise it could trigger problems further on when *marked-cells* are required for selection, i.e. a point will be needed for each control volume to be marked out. In other words, selected control volumes (or marked cells as we will commonly refer to) must conform a closed area with no cell exception for a later correct selection of all cells inside the airfoil area. To guarantee this condition, an interpolation process should be implemented. Figure 3.3 shows how interpolated (blue) points must be located between original (orange) points in order to complete the reciprocity between a marked cells and coordinate points.

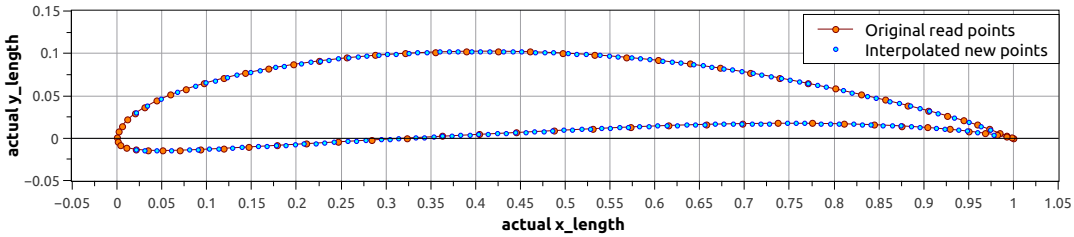

Figure 3.3. Read points(orange) and interpolated points(blue).

As shown in figure 3.3, the points read from the data base are complemented with new ones added by interpolating them between existing pairs of points, and inserting as many as it is necessary in order to fill the space with enough points equally spaced having a separation less than the size of a control volume (Δx or Δy, depending on the slope case). The procedure to achieve this is described in the diagram shown in fig.3.5 where the algorithm is explained.

The original number of points is $n = \sum_{i=1}^{n} c_i$, where c is a single Cartesian point (x, y), an m is the new number of points, summing the original set plus the new ones: $m = n + \sum_{i=1}^{n-1} p_i$, where p_i are the points created between each pair of $(x, y)_i$ and $(x, y)_{i+1}$ original points. The number of interpolated points p_i may vary from segment to segment because of it is the ratio of the distance between original point couple and the size of a control volume. See figure 3.4 for the detailed graphic explanation.

The output data will lead to the selection of the proper control volumes over the Cartesian domain using the mark cells technique described on step (iv) and is explained in the algorithm shown in figure 3.5. The code has a conditional rule depending on whether the angle

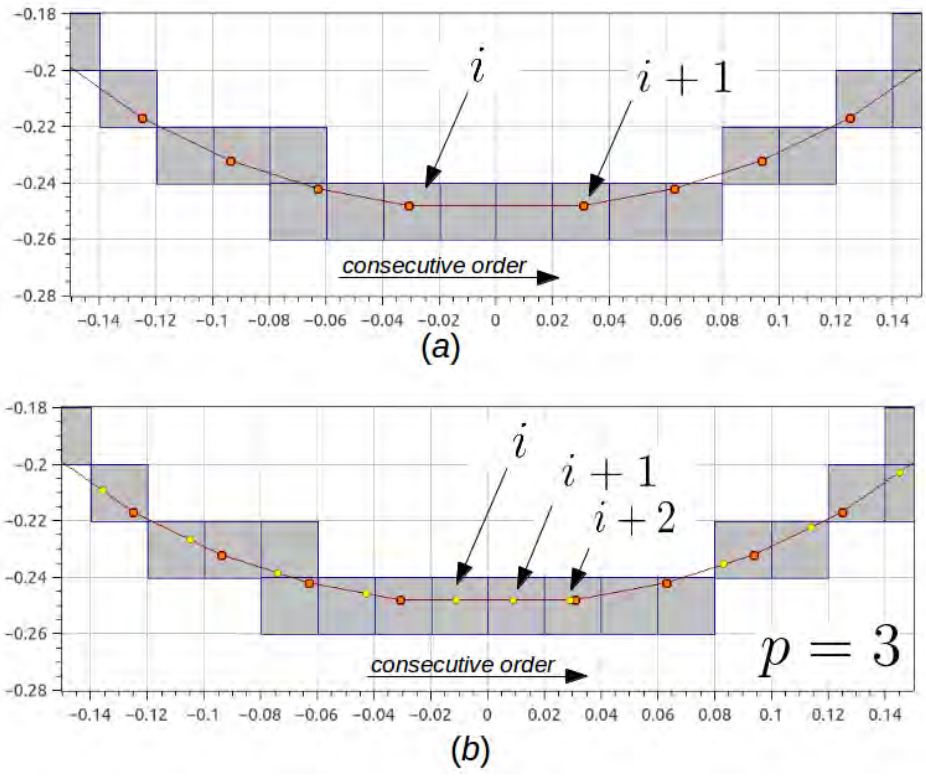

Figure 3.4. (a)Points read by subroutine (orange) from the original data base and (b)new added points (yellow) creates the p_i set for each pair of original points. The entire enumeration of points is reset after interpolating new ones. Notice that there must be a point $(x, y)_p$ for each control volume cell(gray) selected further on (future selected control volumes (mark cells) are only shown as reference).

of attack (AOA) is either equal or different from zero. For $AOA \neq 0$ an auxiliary subroutine will be called to rotate all read/created points, to create a file with new Cartesian coordinates $x - y$. From the wind turbine blade axes of coordinates, this implies it changes the pitch angle. The output for this tilted airfoil geometry with the specified angle will be also marked out later according to the technique explained in step (iv). Rotation of all points will be done as described in the diagram as the rotating subroutine. The algorithm of this last code segment will be described in what follows.

(iii) **Find aerodynamic center and rotation.** The point at which the resultant pressure acts is called the center of pressure. If we consider an airfoil at an angle of attack, we can theoretically determine the pressure variation around the airfoil, and calculate the aerodynamic force situated at the center of pressure. Formally, the center of pressure is defined

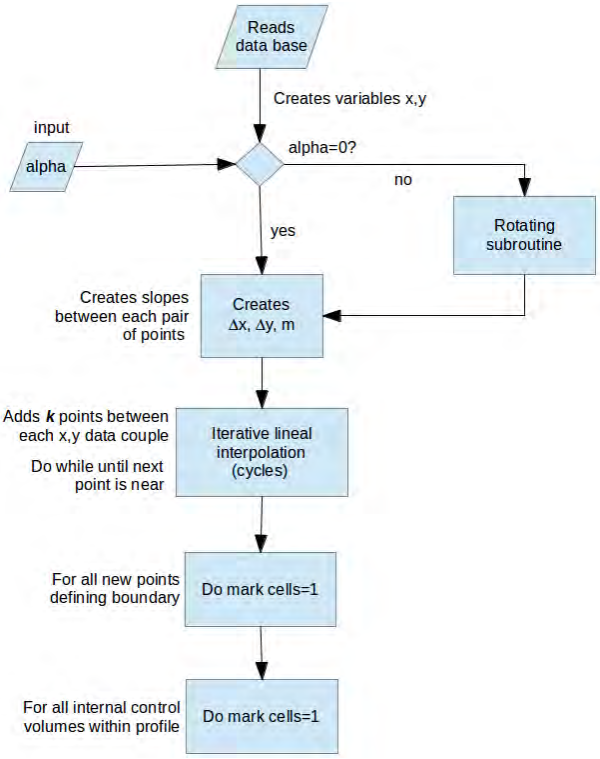

Figure 3.5. Flow diagram for reader-point adder subroutine.

by,

$$x_{cp} = \frac{\int x(s)\, p(s)\, ds}{\int p(s)\, ds} \qquad\qquad y_{cp} = \frac{\int y(s)\, p(s)\, ds}{\int p(s)\, ds}$$

where s is the coordinate around the airfoil, and $x(s)$, $y(s)$ determine the airfoil profile. If we change the angle of attack, the pressure distribution changes and therefore the aerodynamic force, the location of the center of pressure, and the moment will change. Hence, determining the aerodynamic behavior of an airfoil is very complicated if we use the center of pressure to analyze the forces. We can compute the moment about any point on the airfoil if we know the pressure distribution. The aerodynamic force will be the same, but the value of the moment depends on the point where that force is applied.

On other hand, the aerodynamic center is defined as the point at which the aerodynamic angular momentum, M, is independent of the angle of attack, α. It is convenient to specify the aerodynamic center (ac) as the point at which the pitching moment coefficient C_M for the airfoil does not vary with lift coefficient (i.e. angle of attack), which is $\frac{dC_M}{dC_L} = 0$. It

has been found both experimentally and theoretically for thin airfoils at low speed that, if the aerodynamic force is applied at a location $\frac{1}{4}$ chord from the leading edge on most low speed airfoils, the magnitude of the aerodynamic moment remains nearly constant with the angle of attack. The location where the aerodynamic moment remains constant is called the aerodynamic center (ac) of the airfoil. Using the aerodynamic center as the location where the aerodynamic force is applied eliminates the problem of the movement of the center of pressure. For supersonic airfoils, the aerodynamic center is nearer to $\frac{1}{2}$ chord location.

For symmetric airfoils, the aerodynamic moment about the ac is zero for all angles of attack. With camber, the moment is non-zero and constant for thin airfoils. For a positive cambered airfoil, the moment is negative and results in a counter-clockwise rotation of the airfoil. With camber, an angle of attack can be determined for which the airfoil produces no lift, but the moment is still present [4].

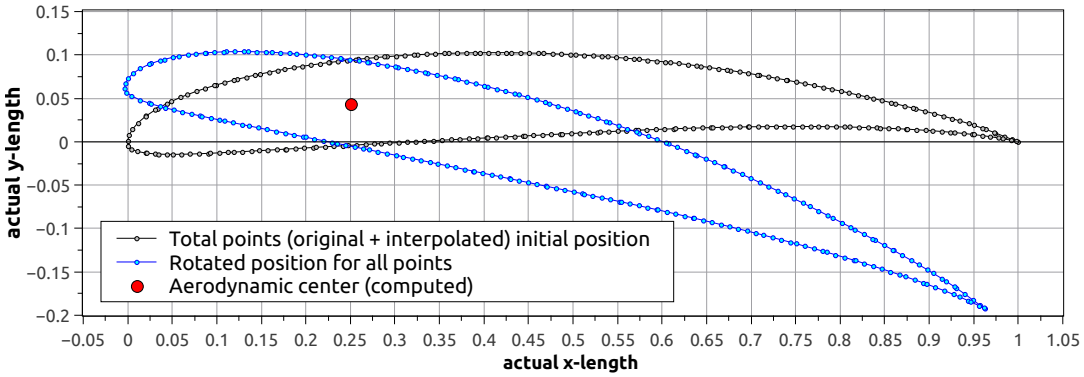

Figure 3.6. Rotated points using aerodynamic center as pivot.

The present code was programmed in such a way that ac is selected precisely as pivot for pitching the airfoil. This strategy was selected in order to have an equivalent comparison, keeping the same moment over the airfoil, at the same reference frame conditions and inputs. The position of the aerodynamic center is shown in figure 3.6. The flow diagram for the rotating subroutine algorithm is shown in figure 3.7.

(iv) **Select boundary and internal cells in the solid domain.** The output for a rotated or non-rotated geometry will return data to airfoil reading subroutine, leading us to the next step of the main subroutine: A boundary cell selection in the solid domain.

Two factors are involved here: A measuring proximity factor that indicates if new points must be created, and an adding proximity factor, that creates and locates the new points between original pair $(x, y)_i$, $(x, y)_{i+1}$. Let be n the original number of data points and m the new number of data points added via while-loop between each $(x, y)_n$ data couple.

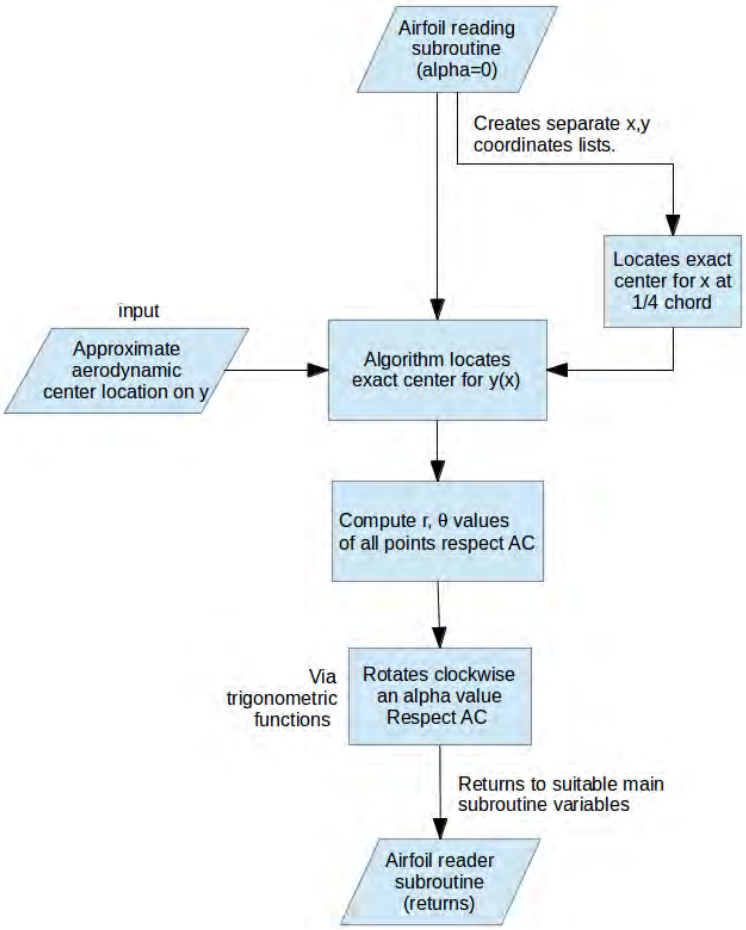

Figure 3.7. Flow diagram for point-rotation subroutine.

A new set k of total points is obtained. At this stage of the main algorithm, slopes m_{k-1} are created between each pair of points $(x, y)_k$. It is important to see that for each new pair of points $(x, y)_k$, a new set of slopes m_{k-1} between them are created. Then, the algorithm finds a (i, j) location to assign a mark cell(i,j) value and a local normal slope cell(i,j) value (see figure 3.8). After all new points are created, marking-cell procedure cycle starts. For each new point $(x, y)_k$ created, a control volume or cell is marked with the integer variable $marked\,cell = 1$ for the solid domain and the remaining cells with the default values $marked\,cell = 0$.

The marking cell technique described on the previous chapter shows the numerical treatment for each selected cell used as a boundary in the solid domain as well as in the boundary of the fluid domain. In fig. 3.9, boundary selection for the cells of interest is illustrated.

The selection of the whole solid domain area is done by a boolean operation of a double selection of cells in a vertical direction. Two cycle selections were performed previously: One

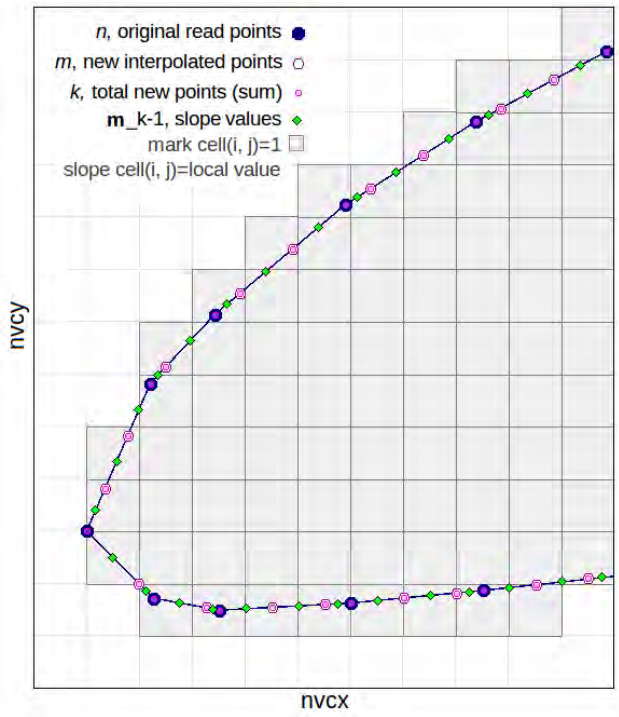

Figure 3.8. Selection of cells at the boundary (mark cells(i,j)=1) and slope value assigment (slope cells(i,j)=1).

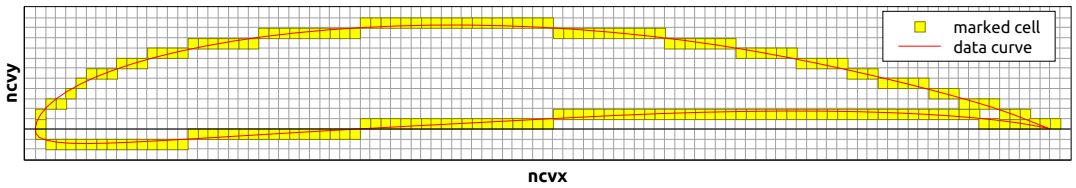

Figure 3.9. Solid domain first selected boundary cells.

from up-down direction marking cells from the lower boundary of the airfoil, and a second one, going from down-up direction marking cells from the upper boundary. The union of both sets contain the final selection of the appropriate cells of the interior area of the object. An example of final marked cells for tilted control volumes using the *ac* as pivot is shown in figure 3.10 highlighted in yellow. The *ac* pivot is denoted as a red filled circle.

(v) **Select boundary cells at fluid domain for monitoring.** The next step in the main algorithm is to identify the boundary cells for the fluid domain. A boundary cell is defined

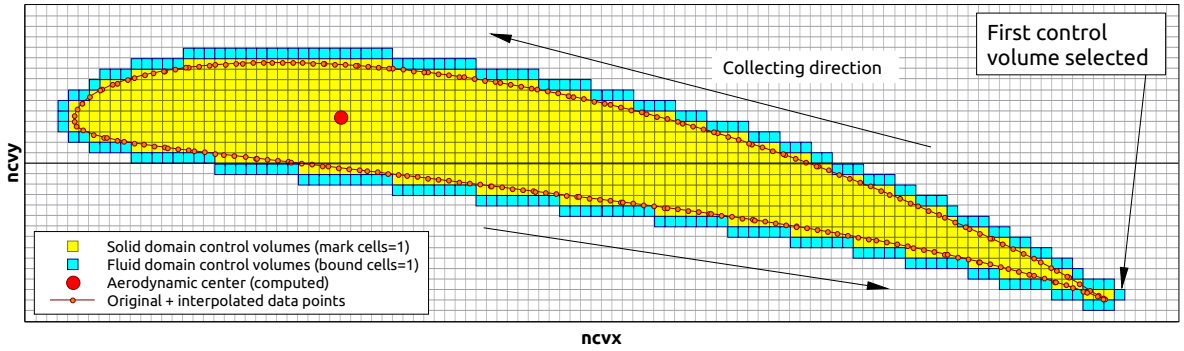

Figure 3.10. Final selected control volumes of airfoil in an Cartesian domain. Marked (mark cells=1) and boundary cells (bound cells=1) selected. Boundary cells are selected and listed.

as a cell that contains a point that defines the airfoil profile. The algorithm used for selecting boundary cells is as described in figure 3.11:

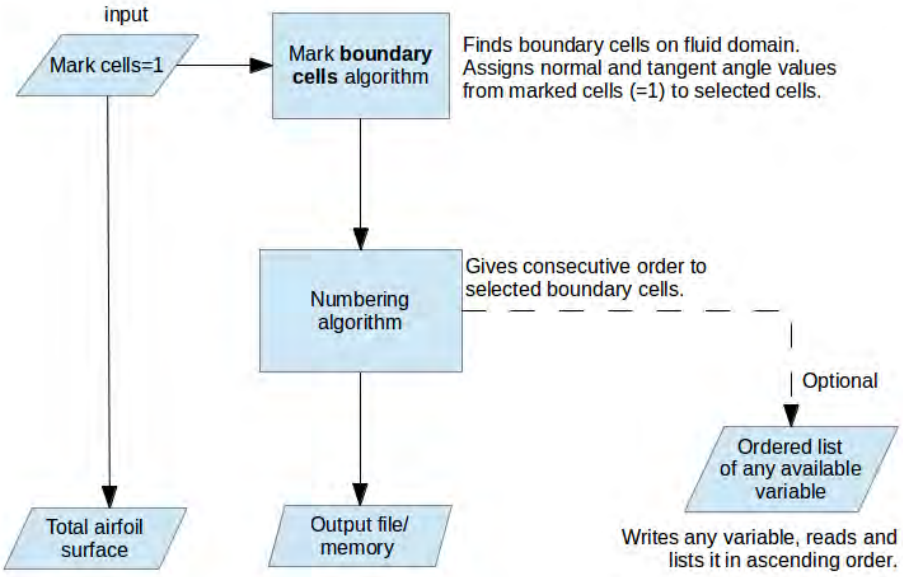

Figure 3.11. Flow diagram for boundary cells selection (fluid domain) subroutine.

1. Locate the cell at the trailing edge.
2. Search the next cell, looking for the neighbour boundary cell in the fluid domain. Search these cells with the following priority: Give preference to north, then north-west and west cells, and mark them as boundaries.

3. Select the next cells on the boundary, continuing with south-west, south and south-east cells, in consecutive order.

4. End of search criterion. When the boundary cells search finds the first cell at the trailing edge cell then the process stops. Figure 3.10 shows an example in the direction of selection of all boundary cells around.

Examples in the case of a tilted airfoil (relative to incoming wind direction) are shown in figure 3.10, where the selection of boundary cells of solid body and inside filling (yellow) using all data points, and boundary fluid cells (blue).

The boundary cells in the fluid domain will work as monitor cells. The purpose of listing the boundary cells in the order just described is to show information contained there, for instance the geometrical features, like the normal and tangent angles relative to the surface for each one of these control volumes. These angles are called $\theta_{\hat{n}}$ and $\theta_{\perp\hat{n}}$ of slopes m_{m-1} and are associated at this point to marked cells in the boundary of the fluid domain using the variable $bound\,cells = 1$, shown in figure 3.12 and 3.13. With this strategy, the pressure and velocity are conveniently stored once the solution is reached after the time cycle.

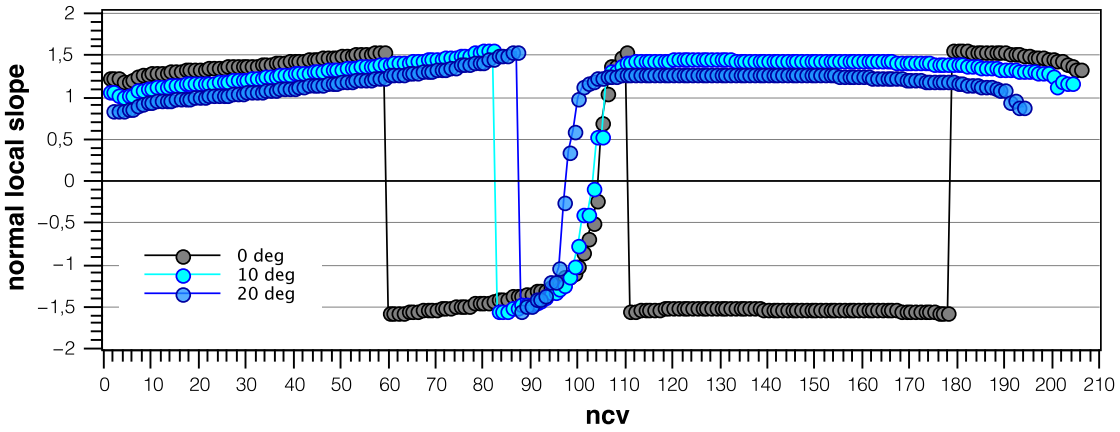

Figure 3.12. Normal local slope at different attack angles. The $x-$ axis is the monitor at the boundary cell denoted as ncv or number of control volume.

Local normal and tangent slopes are allocated in the boundary cells of the fluid domain (with variable $bound\,cells = 1$), and are collected as follows: (1) For each $(x, y)_i$, $(x, y)_{i+1}$ segment, a m_{m-1} is computed, (2) For each marked cell (on boundary cells of the solid domain), selected as described on step (iv), a m_{m-1} value is allocated. (3) Likewise, $\theta_{\hat{n}}$ and $\theta_{\perp\hat{n}}$ in marked cells will transfer values to boundary cells in the fluid. For each angle of attack, local normal and tangent angles $\theta_{\hat{n}}$ and $\theta_{\perp\hat{n}}$ will change. This method was useful to confirm

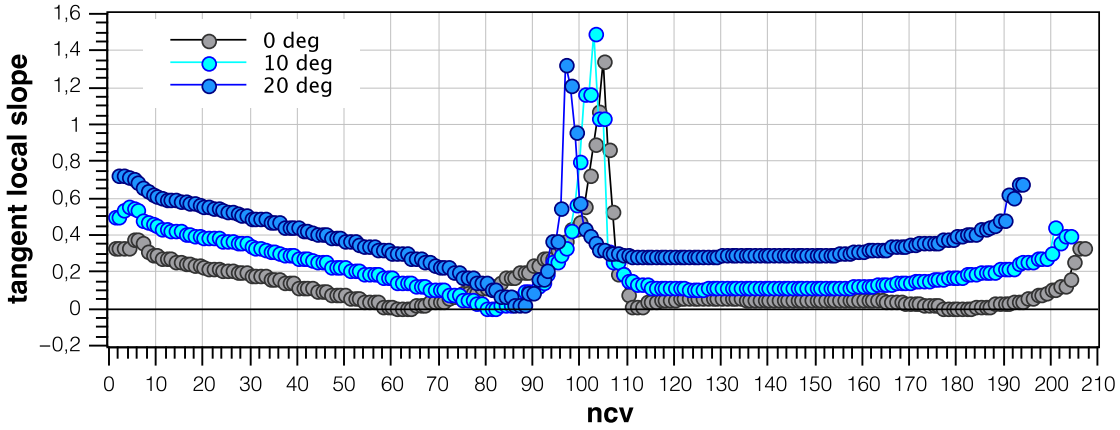

Figure 3.13. Tangent local slope at different attack angles (Only positive values).

that values on every control volume were effectively sensitive to each α step.

(vi) **Computation of the total force obtained from pressure.** After the time cycle has finished and the $\nabla \cdot u = 0$ condition has been satisfied, the final pressure p and velocity u, v fields are obtained on the whole fluid domain. The pressure algorithm for computing values at boundary is shown in figure 3.14.

As described on sections 2.2.2 and 2.2.3, for the square and circular geometries, a similar procedure was followed to compute $\vec{F}_{P,total}$ by integrating $\int Pds$ for the whole boundary. The specific steps of the algorithm are:

1. Normal forces are computed for each cell considering the local pressure in $\hat{n}$ direction.
2. The segment ds for each control volume at the boundary is computed with the expression $\sum_{i=1}^{m-1}(x,y)_{i,i+1}/ncv_{bound}$, i.e. the sum of length segments between all m new points divided by the total number of control volumes in the solid boundary.
3. Resultant force is split in $\mathbf{F}_x$ and $\mathbf{F}_y$.
4. The force components are integrated obtaining finally $\mathbf{F}_{x,total}$ and $\mathbf{F}_{y,total}$ for pressure sources.

The aerodynamic performance of airfoil sections can be studied most easily by reference to the distribution of pressure over the airfoil. This distribution is usually expressed in terms of the pressure coefficient, $C_P = (P - P_\infty) \,/\, \left(\frac{1}{2}\varrho U_\infty^2\right)$. C_P is the difference between local static pressure and freestream static pressure, nondimensionalized by the freestream dynamic pressure. The plot C_P vs. x/c as illustrated on figure 1.9, in chapter 1, and indicates that there

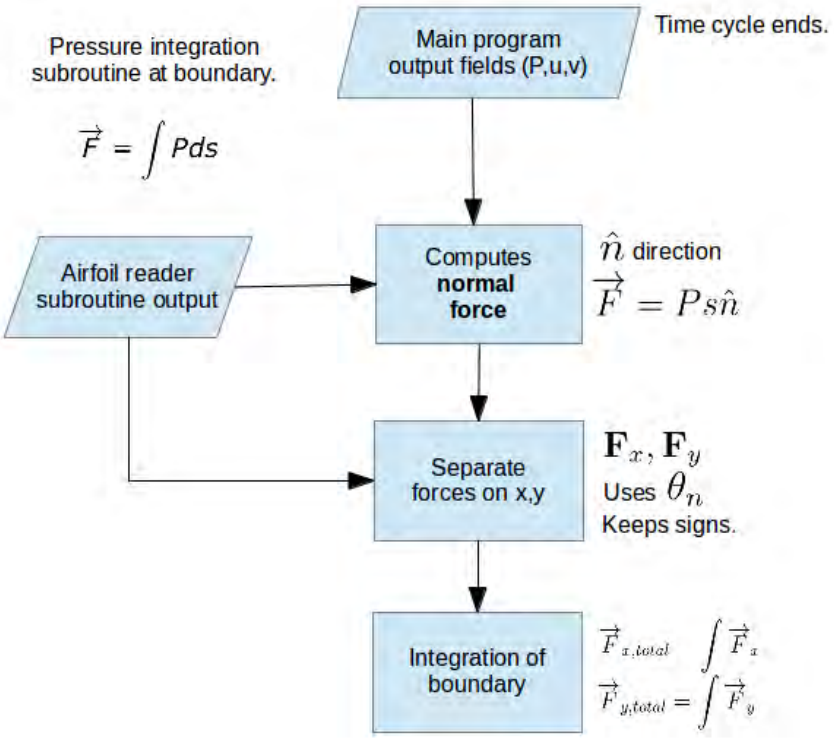

Figure 3.14. Flow diagram for total force obtained from pressure.

is a variation from the leading edge (0.0) up to the trailing edge (1.0), depending of the presence of a boundary layer. C_P is plotted upside-down with negative values (*suction*), higher on the plot.

(vii) **Computation of the total force obtained from shear stress.** The algorithm for computing the total force $\vec{F}_{ss,total}$ originated at the boundary is shown in figure 3.15. The total force is obtained by integrating $\int \tau ds$, where τ is the stress tensor and ds is the differential of the distance along the airfoil. Let us consider $\theta_{\hat{n}}$ as the angle normal to the airfoil surface, $\theta_{\perp\hat{n}}$ as the angle tangent to the airfoil surface, θ_u the angle of the velocity of the fluid at the boundary cell and α_{ss} is the opposite angle in the velocity triangle formed by the velocity of the fluid at the boundary cell and the tangent component of this velocity. See also figures 3.16 and 3.17 to identify each of them. The steps of the algorithm are:

1. Compute the resultant velocity $\vec{u}(u, v)$ and θ_u, over a convenient absolute-reference frame.

2. Classify the location of ($\vec{u}(u, v)$, θ_u) in a specific position (see figure 3.16) formed by

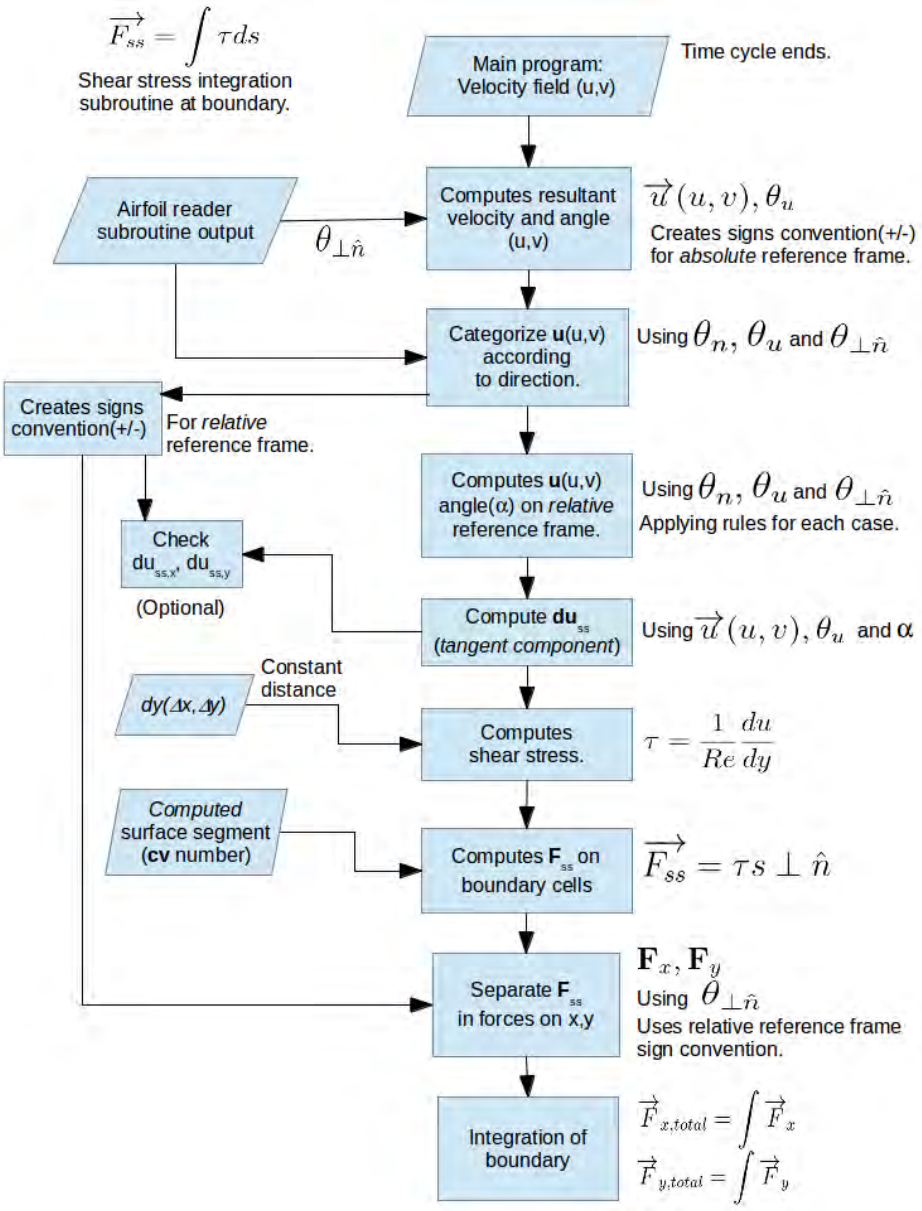

Figure 3.15. Flow diagram for total force obtained from shear stress.

the absolute-reference frame (x-y) and the relative-reference frame $(\theta_{\hat{n}}, \theta_{\perp\hat{n}})$ in order to choose the adequate algebraic rule in the next step. Figure 3.17 shows how this may change depending on $\theta_{\hat{n}}$, $\theta_{\perp\hat{n}}$ and θ_u case.

3. Compute α_{ss} angle using geometric rules based on $\theta_{\hat{n}}$, $\theta_{\perp\hat{n}}$ and θ_u depending on a

specific category previously defined. Variable α_{ss} was created for simplifying computing du_{ss} in the next step. No matter the direction of $\vec{u}$, the algorithm must compute the appropriate α_{ss} projected value. Notice that $\alpha_{ss} \neq AOA$.

4. Compute $du_{ss} = \vec{u} \cdot \sin \alpha_{ss}$. This is a tangent component of the velocity for every control volume on the boundary cells in the fluid domain.

5. Compute shear stress $\tau = \frac{1}{Re} du_{ss}/dy$, using a constant dy, that is the perpendicular average distance between the center of the control volume at the boundary(where velocity is measured) and the airfoil theoretical surface, that is $dy = \Delta x$ or Δy.

6. Compute $\vec{F}_{ss} = \tau \cdot s$ applied on $\theta_{\perp \hat{n}}$ direction.

7. Split the resultant force in $\mathbf{F}_x$ and $\mathbf{F}_y$.

8. All these local forces are integrated to obtain $\mathbf{F}_{x,total}$ and $\mathbf{F}_{y,total}$ stress source.

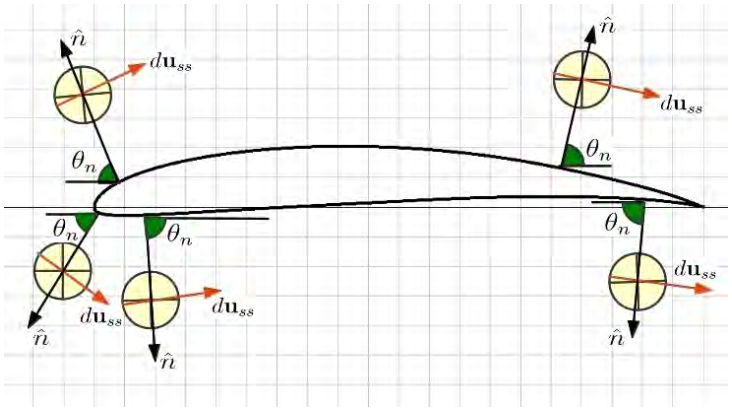

Figure 3.16. Projection rules for obtaining a tangent component from normal and tangent unit vectors.

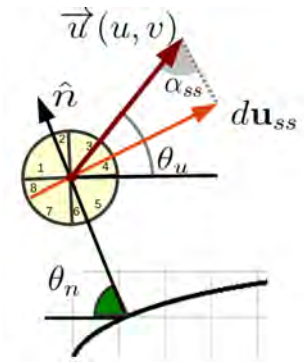

Figure 3.17. Details for obtaining tangent component from a velocity vector.

(viii) **Algorithm for lift-to-drag ratio (L/D) ratio subroutine.** A useful measure for the aerodynamic efficiency of an airfoil is the lift-to-drag ratio, given by $\frac{L}{D} = \frac{C_L}{C_D}$. At any given velocity, high as possible $\frac{L}{D}$ values are desired because the higher this ratio value is, the more aerodynamically efficient the body facing a flow is. The $\frac{L}{D}$, algorithm is shown in diagram 3.18.

The steps for the algorithm are: (1) The forces $\mathbf{F}_{x,total}$ and $\mathbf{F}_{y,total}$ at each point on the boundary are computed for both pressure and shear stress, (2) the forces are integrated and projected for each direction $x, total$ and $y, total$, (3) the coefficients C_L and C_D are computed and, (4) the ratio $L/D = \frac{C_L}{C_D}$ is obtained.

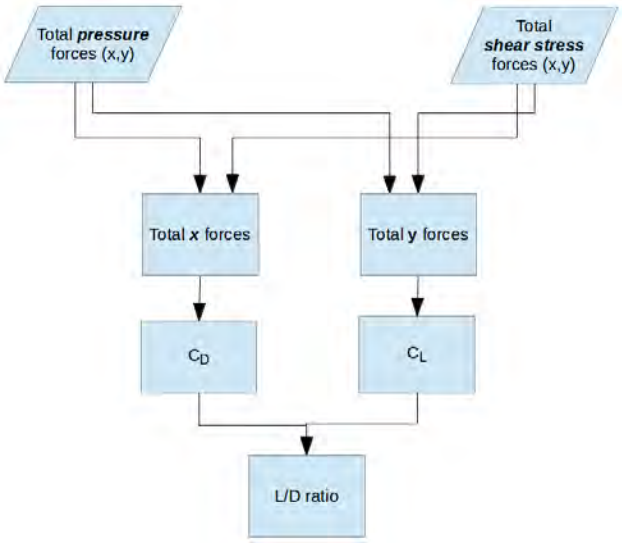

Figure 3.18. Flow diagram for L/D ratio computation.

3.2 Calculation for a streamlined profile.

3.2.1 Inputs.

A validation for a streamlined profile was done by applying the algorithms described on the previous section. The inputs are shown in tables, 3.1, 3.2 and 3.3

Table 3.1. Inputs for a streamlined a profile run validation.

Item	Input
Grid type	Cartesian/structured
Domain size, $x \times y, y - centered$	20×5
Number of control volumes, $nx \times ny$	400×100
Time step, dt	0.005
Number of time iterations, $itmax$	20,000
Iteration tolerance	1E-5

3.2.2 Lift and drag relationships.

The aerodynamic performance, which depends mainly on the lift and drag, is fundamental for the design of an efficient rotor blade. Aerodynamic lift is the force responsible for the power

Table 3.2. Constants for streamlined profile run validation

Item	Constant
Reynolds, *Re*	100
Inlet x velocity, u	1.0
Control volume size, $dx \times dy$	0.05×0.05
Cylinder diameter, D	1.0
Center location, (x,y)	6.0, 0.0
Total elapsed time units, *time*	100
Maximum number of iterations, *maxiter*	100

Table 3.3. Conditions for streamlined profile run validation

Item	Constant
Scheme	Central Difference
Boundary cond. on Top/Btm walls	Free-slip
Time scheme	Implicit
Formulation type	Simplec

yield generated by the turbine and it is therefore essential to maximise with an appropriate design. The drag force which opposes the motion of the blade is also generated by friction and should be minimized. Figure 3.21 (a) shows the drag and lift coefficients (C_D and C_L) as functions of the angle of attack (AOA).

Expected reduction of C_L at $\approx 15°$ does not appear, rather it continues ascending until 30°, for reasons not completely verified. Below, figure 3.20 (a) at left shows a C_D-C_L polar type graph for positive values of C_L and right (b) shows the L/D ratio graph.

The ratio of lift to drag is an indication of the aerodynamic efficiency as we already explained. It is then apparent that an aerofoil section with a high lift to drag ratio, typically greater than 30, can be chosen for a rotor blade design [38]. We can observe the similarity with typical curves in 1.14.

3.2.3 Pressure distribution over an streamlined body.

The pressure distribution is plotted using consecutive selected control volumes in the horizontal axis using our own cell monitor. Starting from the trailing edge going over the upper surface to the leading edge and then back by the lower surface back to the starting point.

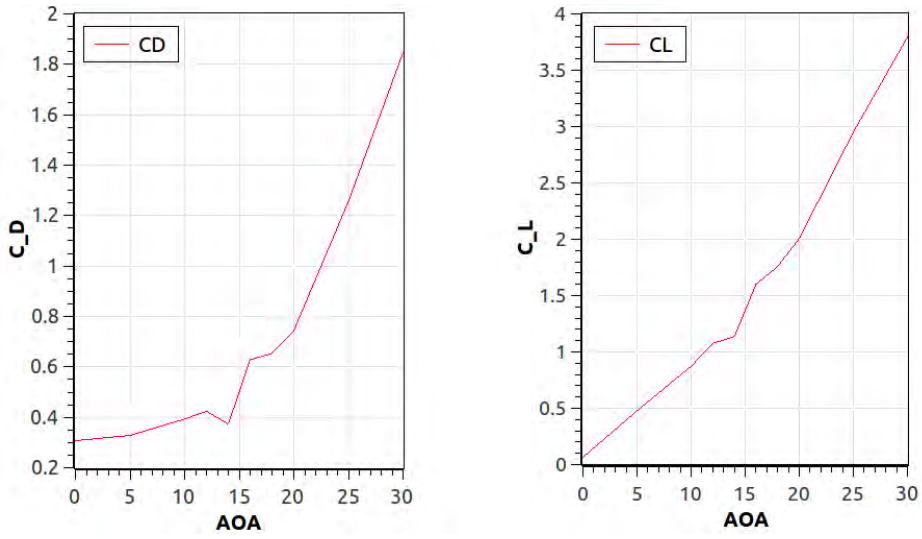

Figure 3.19. C_D-α (left); C_D-α (right)

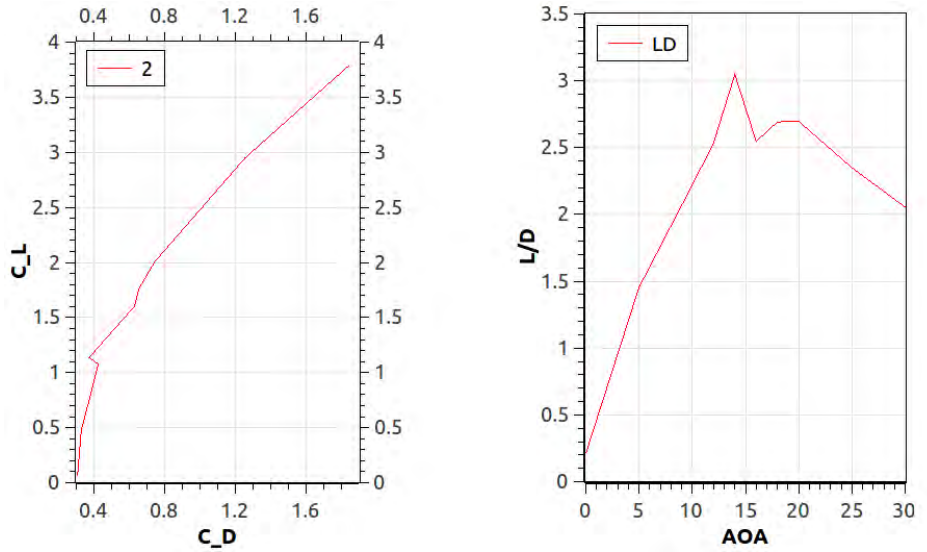

Figure 3.20. C_D vs. C_L (left); L/D ratio (right).

Contrary to typical representations, positive values are plotted in the upper side of the graph. The pressure at the stagnation point passes through 0. Figure 3.21 shows pressure distribution at boundary cells at Re=100 for $\alpha = 0°$, $10°$ and $20°$ [25].

The pressure field is a function of the thickness of a streamlined body placed in the flow. The acceleration and deceleration caused by a finite body width creates favourable and un-

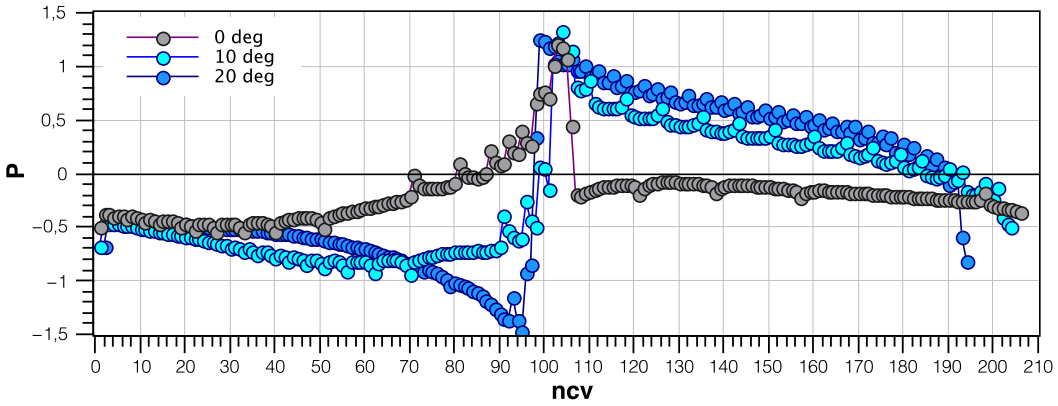

Figure 3.21. Pressure distribution at boundary cells for Re=100, $\alpha = 0°$, $10°$ and $20°$, along chosen control volumes at the boundary.

favourable pressure gradients. When the body is thin, there are only weak pressure gradients and the flow remains attached. As the body gets thicker, the adverse pressure gradient resulting from the deceleration near the rear, leads to flow separation, recirculation and vortex shedding. Focusing on the rear region of the flow, it is seen that as thickness of the body is reduced in the separated region disappears as the adverse pressure gradient is diminished [11]. As we observed in figures 1.8 and 1.9, the effect of the boundary layer is to reduce the pressure distribution at the rear of the aerofoil [12]. This coincides with previously reported theoretical observations explaining for a viscous flow: When the backward force due to the decreased pressures behind the maximum thickness is somewhat increased, while the forward push due to the increased pressures near the tail is much reduced, provoking a rearward force known as boundary layer normal-pressure drag (form drag). [23].

The pressure distribution for $Re = 100$ is shown in figures 3.22 (a), (c) and (e) for $\alpha = 0°$, $10°$ and $20°$ respectively. These values will be used later for C_L, C_D computation. The pressure field distribution is given in the right hand column, figures (b), (d) and (f). A more detailed scalar pressure field for this case is shown as the sequence in figure 3.25, for a range of α values from $0°$ to $30°$. The stagnation point that appears initially at the leading edge moves back, creating a growing high pressure zone below the aerofoil as α increases.

3.2.4 Shear stress distribution over an streamlined body.

In most aerodynamic situations, the pressure p (or the relative pressure $P - P_\infty$ is typically greater than τ by at least two orders of magnitude, and so the resultant $\vec{f}$ is very nearly perpendicular to the surface. But the stress often significantly contributes to drag, so it cannot be neglected entirely.

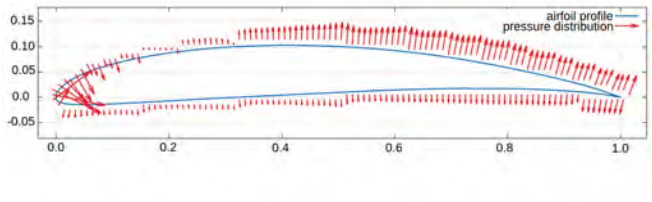

(a) Pressure distribution at 0°

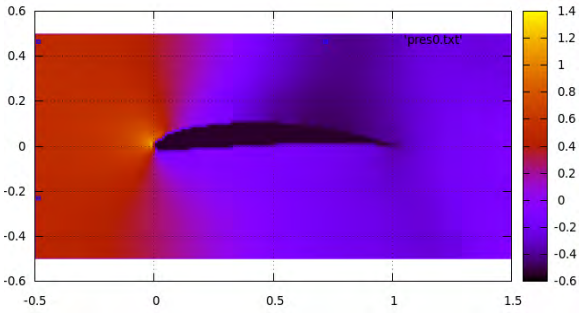

(b) Pressure field at 0°

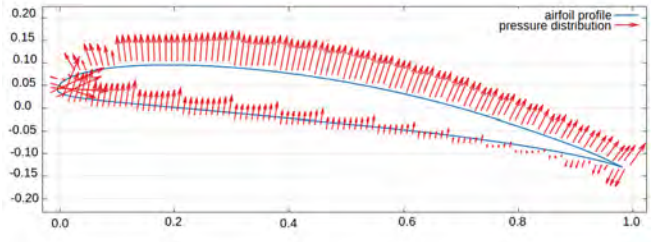

(c) Pressure distribution at 10°

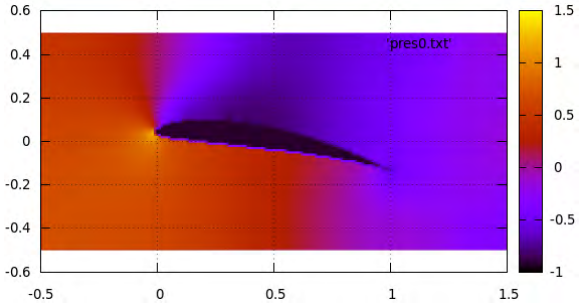

(d) Pressure field at 10°

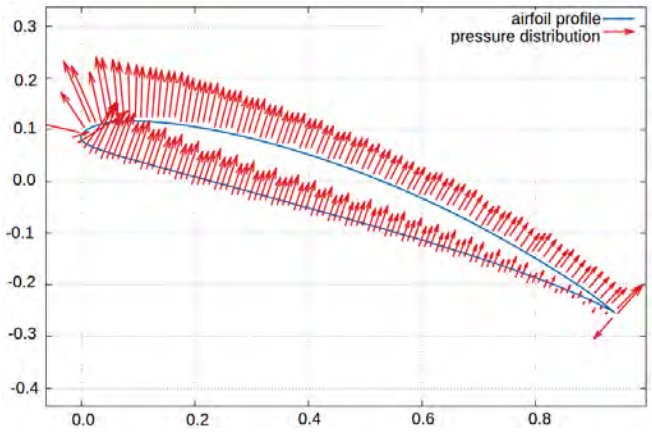

(e) Pressure distribution at 20°

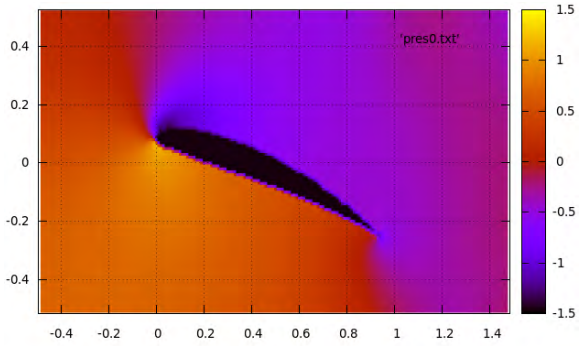

(f) Pressure field at 20°

Figure 3.22. Pressure distribution and pressure field around airfoil

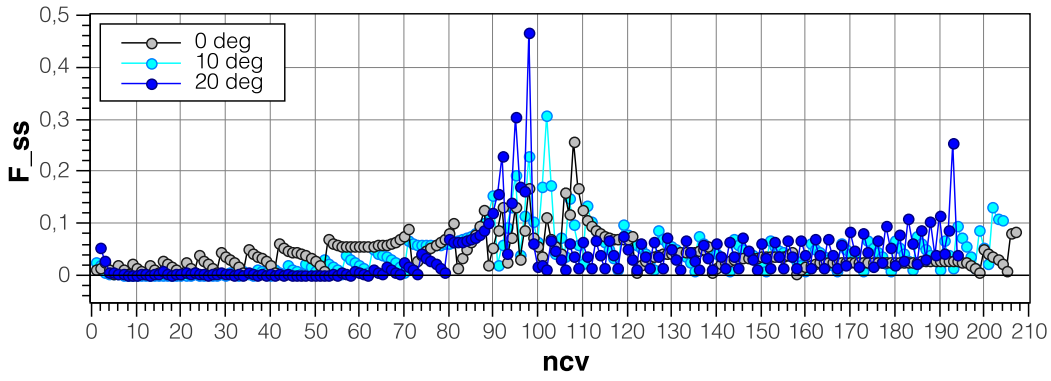

Figure 3.23. Forces from shear stress, function of tangent velocities at boundary cells for $\alpha = 0°$ (gray), $10°$ (cyan) and $20°$ (blue).

Tangent velocity magnitudes used for shear stress (τ) calculation are graphed for $Re = 100$ are shown in figure 3.23 for $\alpha = 0°$, $10°$ and $20°$. Visualization of tangent velocity vectors $\vec{u}$ are also shown in figure 3.24 on boundary cells control volumes[31]. We may appreciate in graph 3.23 large variations between values, mainly due the chequered topology of the surface where the flow see as as small obstacle each stair step that conforms the solid boundary, we may observe this at the abrupt change in magnitude of the velocities around the airfoil surface in figure 3.24.

3.2.5 Boundary layer separation over streamlined bodies.

In the case of streamlined airfoils at a low angle of attack, separation occurs only at the trailing tip with minimal losses. As the angle of attack increases, the separation point moves upstream leading to an increased drag. Laminar flow may be viewed as a streamlined sequence in figure 3.26, for a range of angles of attack from $0°$ to $30°$ and for $Re = 100$. At approximately $12°$ a separation of flow appears at the rear top zone of airfoil, and a clear recirculation visualization appears at $20°$.

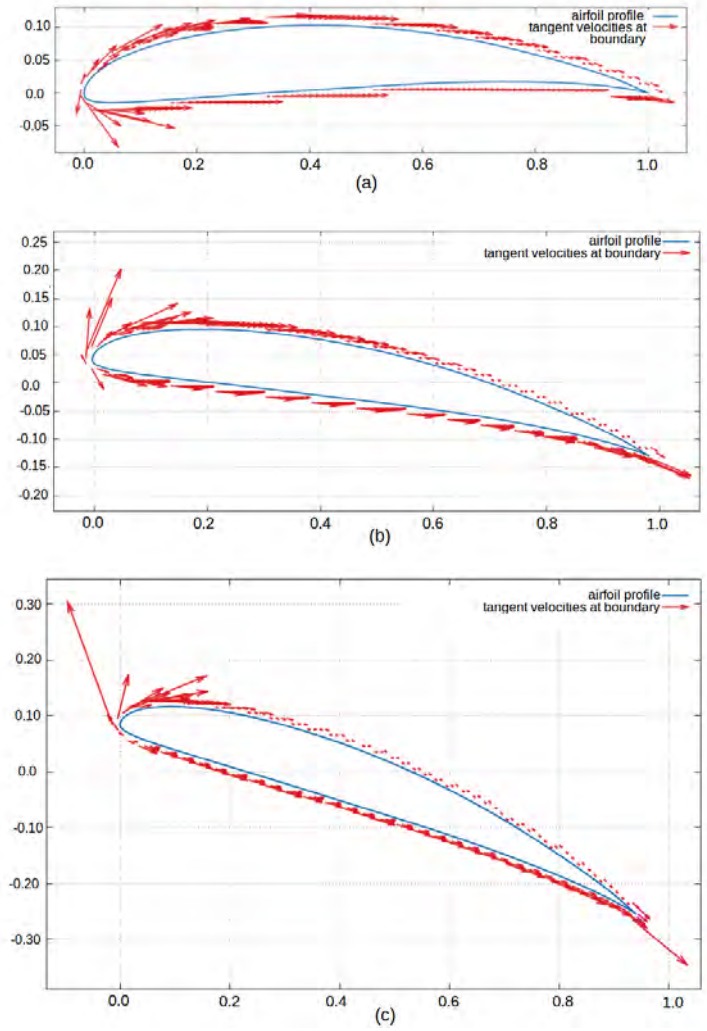

Figure 3.24. Tangent velocities next to airfoil at (a)0°, (b)10° and (c)20° for the present work.

3.3 XFOIL comparison using a HAWT blade using a NACA 4412 profile.

3.3.1 XFOIL results for NACA 4412.

The aim of this study is to compare flow properties at larger Reynolds numbers obtained with the present work code and XFOIL[15]. XFOIL is an interactive program for the design

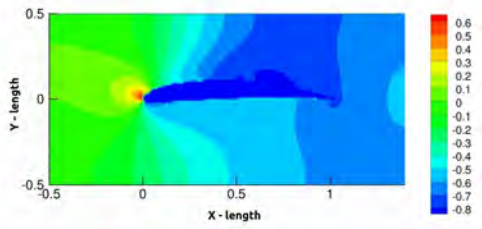

(a) Pressure field at $\alpha = 0°$

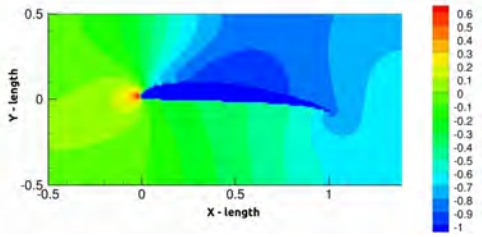

(b) Pressure field at $\alpha = 5°$

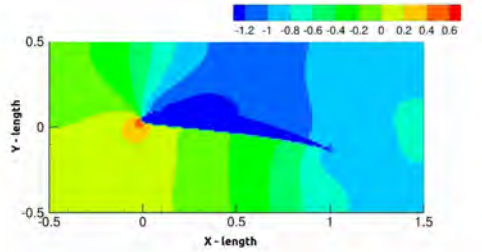

(c) Pressure field at $\alpha = 10°$

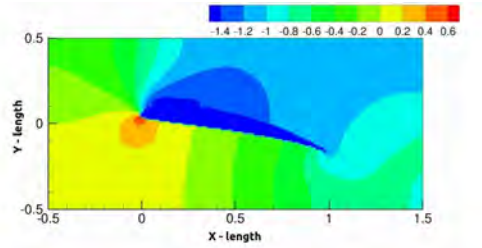

(d) Pressure field at $\alpha = 12°$

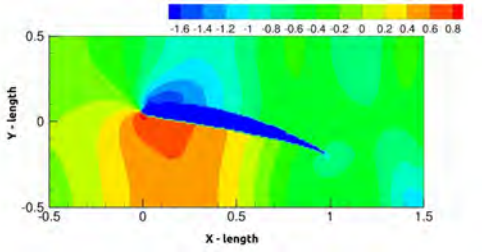

(e) Pressure field at $\alpha = 14°$

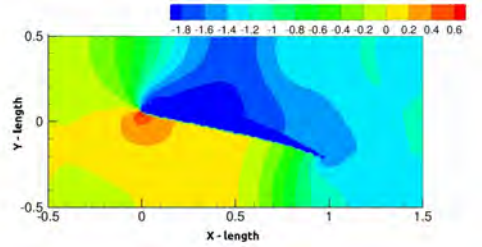

(f) Pressure field at $\alpha = 16°$

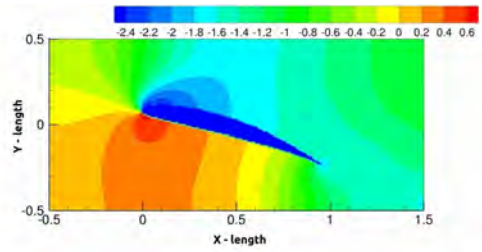

(g) Pressure field at $\alpha = 18°$

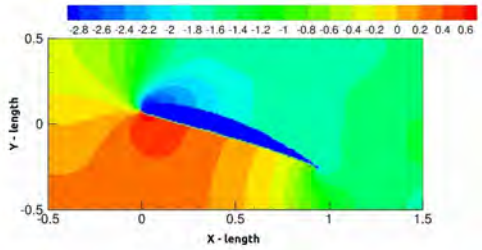

(h) Pressure field at $\alpha = 20°$

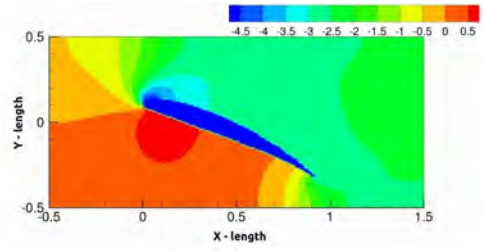

(i) Pressure field at $\alpha = 25°$

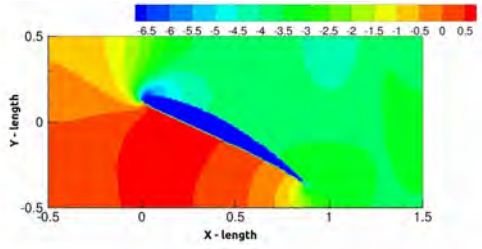

(j) Pressure field at $\alpha = 30°$

Figure 3.25. Pressure field at Re=100 for the present work.

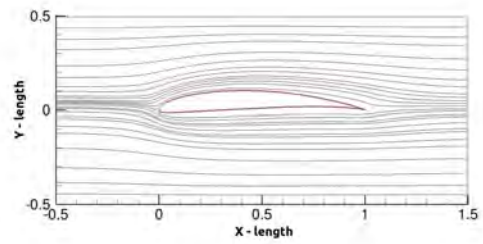

(a) Streamlines at 0°

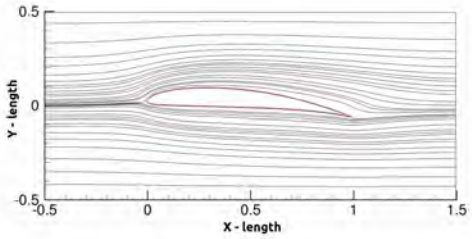

(b) Streamlines at 5°

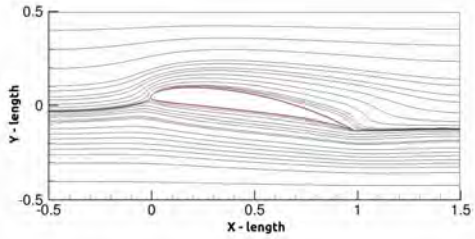

(c) Streamlines at 10°

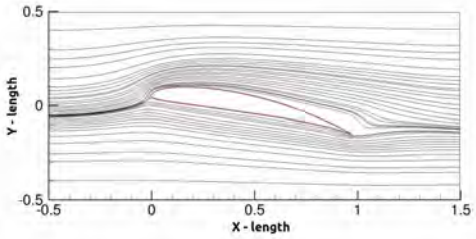

(d) Streamlines at 12°

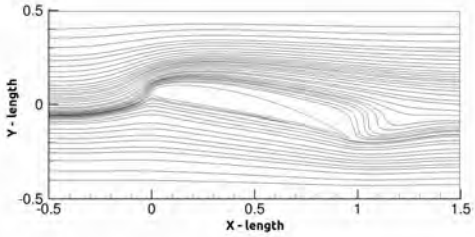

(e) Streamlines at 14°

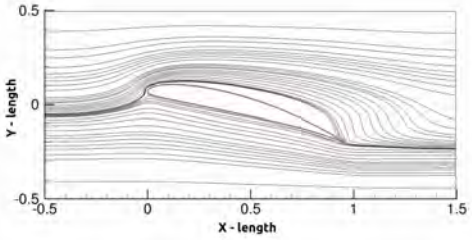

(f) Streamlines at 16°

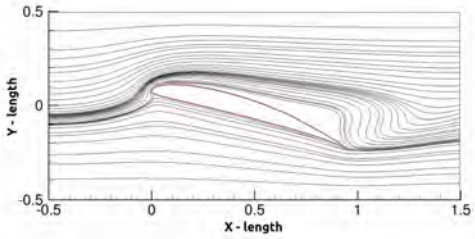

(g) Streamlines at 18°

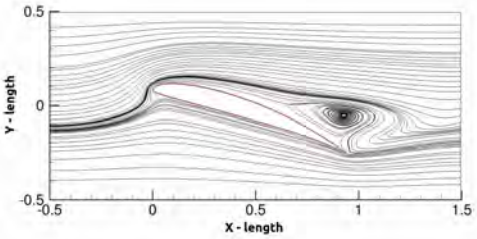

(h) Streamlines at 20°

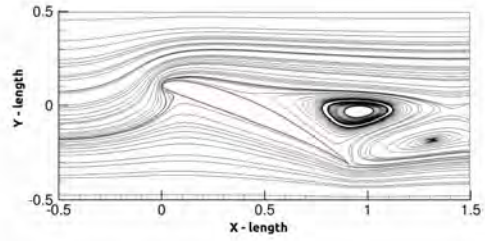

(i) Streamlines at 25°

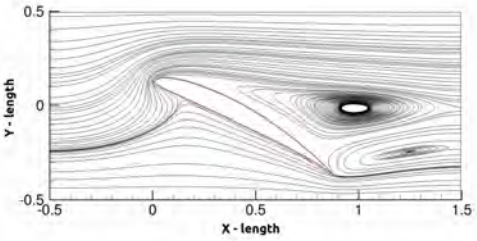

(j) Streamlines at 30°

Figure 3.26. Streamlines at Re=100 for the present work.

and analysis of subsonic isolated airfoils. It consists of a collection of menu-driven routines which perform various useful functions such as viscous or inviscid analysis of an existing airfoil among other capabilities. Given the coordinates specifying the shape of a 2D airfoil, Reynolds and Mach numbers, XFOIL can calculate the pressure distribution on the airfoil and hence lift and drag characteristics. The program also allows inverse design - it will vary an airfoil shape to achieve the desired parameters. It is released under the GNU GPL.

Table 3.4. Results for NACA 4412 run in XFOIL. Inputs for NACA 4412 XFOIL runs are: Mach=subsonic, Viscous=yes, $\alpha = 5.0°$ and $N_{cr} = 9.0$.

Re	100	1000	2000
C_L	–	0.3084	0.3089
C_M	–	−0.0342	−0.0360
C_D	–	0.13607	0.1074
L/D	–	2.27	2.8700

XFOIL is a firsthand tool, one of the most used for analyzing airfoils because the accuracy of their results and the versatility for reading data bases. XFOIL generates results and displays in graphic pressure coefficient (viscous and inviscid) distributions and pressure fields around the profile as well as in polar plots. To achieve this, we must enter as input a single data or a sequence, e.g. a sequence of angles of attack or lift coefficients, leaving other parameters fixed. Another useful result is the thickness of the boundary layer.

Now we present two scenarios: $Re = 1000$ and $Re = 2000$, then we perform the runs in XFOIL software obtaining the results presented in table 3.9. In figures 3.27 *a* and *c* pressure coefficient plots are presented, in figures 3.27 *b* and *d* pressure distribution vectors are shown for both scenarios.

3.3.2 Inputs for our code.

In order to do the comparison with the results reported, the same runs will be performed with our code. The reason of the selected values is that, in any case, our code might be valid for laminar flows. Flow transition to turbulent flow begins from $Re = 2000$, so, no larger Reynolds can be used. XFOIL software becomes less precise as we decrease Re below 10^4, moreover, for many profiles, results may not be obtained for such Reynolds values. In summary, the window between $Re = 1000$ and $Re = 2000$ might be the only valid range -with a certain confidence level- that we can use to compare results.

Default inputs are shown in tables 3.5, 3.6 and 3.7 for three different scenarios: $Re = 100$, $Re = 1000$ and $Re = 2000$. Here are listed domain and time parameters, as well as numeric

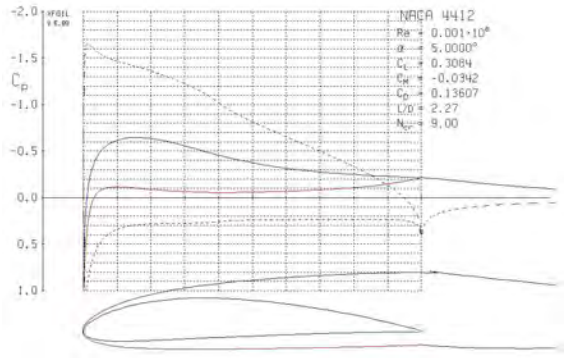

(a) C_P for Re=1000.

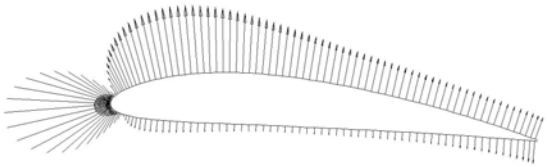

(b) Pressure vector distribution for Re=1000.

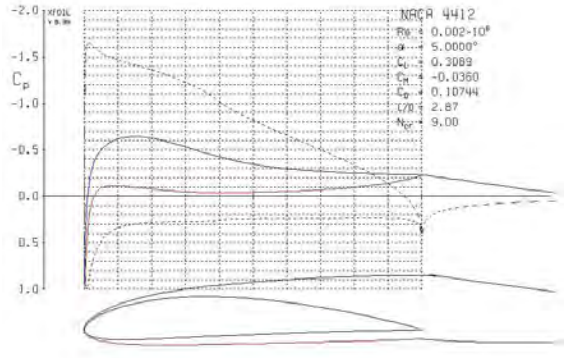

(c) C_P for Re=2000

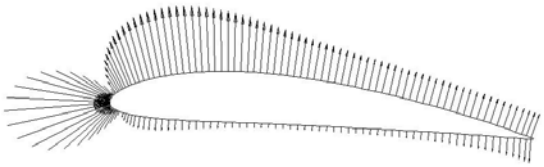

(d) Pressure vector distribution for Re=2000.

Figure 3.27. XFOIL results at $\alpha = 5.0°$ for NACA 4412.

schemes, initial and boundary conditions. All these values will be default used, unless any other declared input is explicitly specified. Table 3.8 shows aerodynamic inputs.

Table 3.5. Domain sizes and characteristics for all Re scenarios.

Input	Description
Grid type	Cartesian, structured
dx, dy	0.010×0.010
nx, ny,	800,100
Total cv	$80,000$

Table 3.6. Input time parameters for all Re scenarios.

Scenario	Description/value
Time units	120
Time step, dt	0.0020
Itmax	$60,000$
Maxiter	100

Table 3.7. Schemes and conditions for run validation.

Item	Value
Scheme	Central difference
Boundary conditions	
on Top/Btm walls	Free-slip
Time scheme	Implicit
Formulation type	Simplec
Tolerance	1E-5

Table 3.8. Aerodynamic inputs and settings for NACA 4412 run validation.

Item	Value
Inlet velocity, $u(= w_r)$	1.0
AOA, α	5.0°
TSR, λ	5.0
Chord at tip, c_{tip}	1.0
Leading edge location	$x = 0.0$, $y = 0.0$
Rotation location	Aerodyn.ctr.

3.3.3 Results for NACA 4412 comparison.

For purposes of illustration, in the present section we compare the pressure coefficient distribution obtained with the code developed in the present investigation and that calculated with the XFOIL code. We chose the airfoil NACA 4412 as the airfoil profile for the benchmark. A pressure maximum is detected at the leading edge, as well as suction zones (i.e. $C_P < 0$) for both upper and lower face, standing out a prevalent suction on the upper side. Comparable order values are observed, mainly for $Re = 2000$ curve.

Looking for the possible causes of the differences, we may cite many, as much as all inputs listed in Tables 3.5 to 3.7. It is important also to consider that our code is time dependent and shows snapshots of a transitory phenomenon, so we may not be observing the closest scenario to XFOIL steady-state results, though we might increment the total elapsed time to close the gap. Also is worth to say that trend difference was expected considering XFOIL uses x-axis location plotting, and our code plots over the normalized whole surface development, which might not be the best comparative point of view. At last, we notice a non monotonic behaviour of the pressure obtained with our code, this effect is originated due the squared-element shaped airfoil.

Table 3.9 shows a comparative result summary between both methods: XFOIL and the present work results, obtained for the Re scenarios expressed in terms of C_L, C_D and L/D. Errors are also computed and shown in last columns.

As it can be appreciated, quantitative errors are less than 30 % which are tolerable for an order of magnitude study. Larger errors are found for L/D and this variable is not recommended to be used as a comparison parameter.

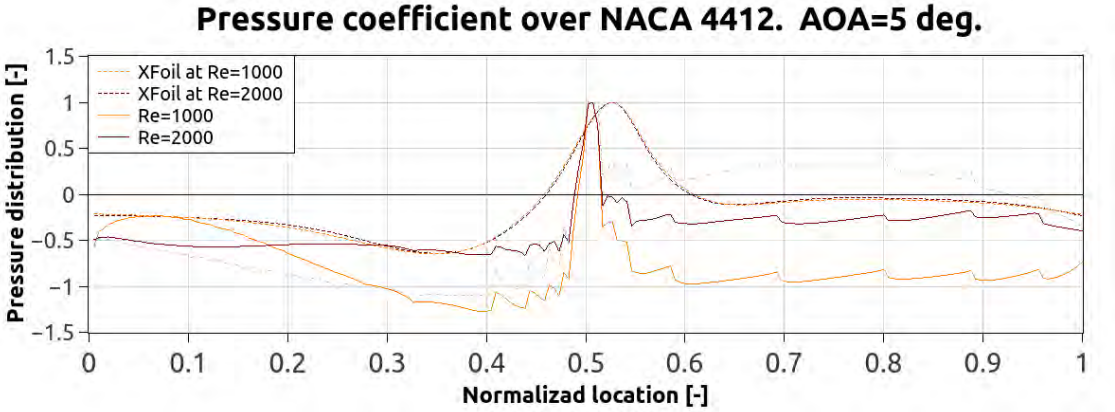

Figure 3.28. Pressure distribution comparison. Present work results are shown in continuous line. $Re = 100$ scenario is also plotted in light gray as reference.

Table 3.9. Comparative table summary for NACA 4412, at $\alpha = 5.0°$. $Re = 100$ showed as a reference.

	XFOIL		Present work			Errors	
Re	1000	2000	100	1000	2000	$error$ $Re = 1000$	$error$ $Re = 2000$
C_L	0.3084	0.3089	0.4438	0.3699	0.3200	19.94 %	3.59 %
C_D	0.13607	0.1074	0.3103	0.0966	0.0750	28.97 %	29.91 %
L/D	2.27	2.8700	1.43	3.83	4.27	68.72 %	61.67 %

3.3.4 Flow description.

A somewhat more detailed description of the dynamic properties of the flow for $\alpha = 5.0°$ and Re =100, 1000, and 2000 is presented in this section. Graphical results are shown in the set of figures from 3.29 to 3.31. The results shown are: (a) Pressure distribution around airfoil displaying normal vectors representing magnitude, (b) pressure field around airfoil plotted by coloured contours, (c) velocity field around airfoil are plotted by coloured vectors representing magnitude, and (d) streamlines overlapped on a z-vorticity field plot with a colour scale. Valuable information may be observed. We may complete the visualization of pressure behaviour around airfoil comparing to figure 3.27, where distribution over the profile may be appreciated. The pressure distribution as a function of the normalized position is shown in figure 3.28 although there are obvious differences between the two sets of results, it is important to highlight that the qualitative trend coincides.

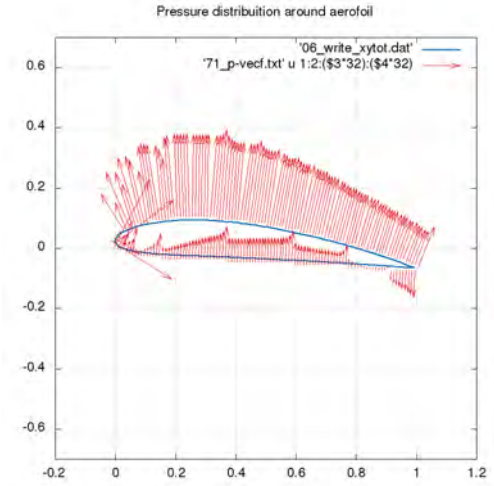

(a) Pressure around aerofoil (normal vectors shows magnitude).

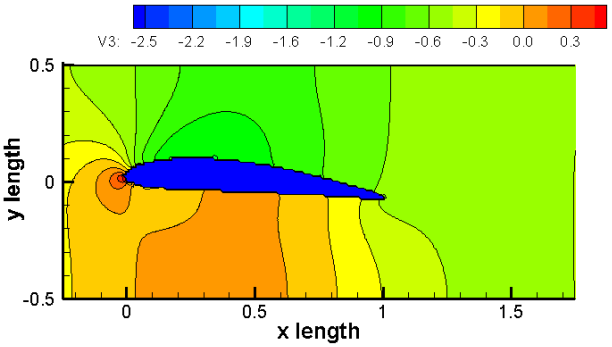

(b) Pressure field around aerofoil (contour plot).

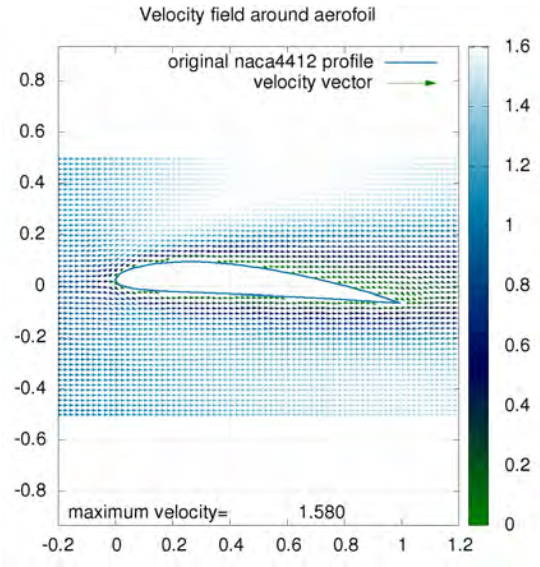

(c) Velocity field around aerofoil (coloured vectors shows magnitude).

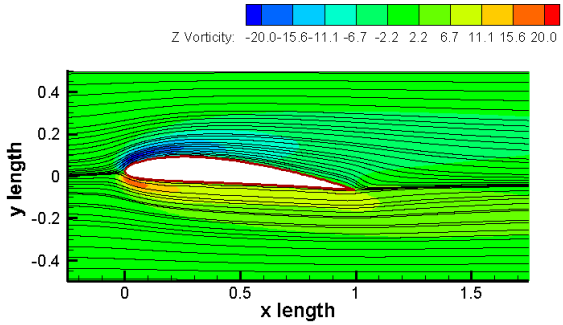

(d) Streamlines and z vorticity field.

Figure 3.29. Results around aerofoil for NACA 4412, at $\alpha = 5°$, at $Re = 100$ for the present work.

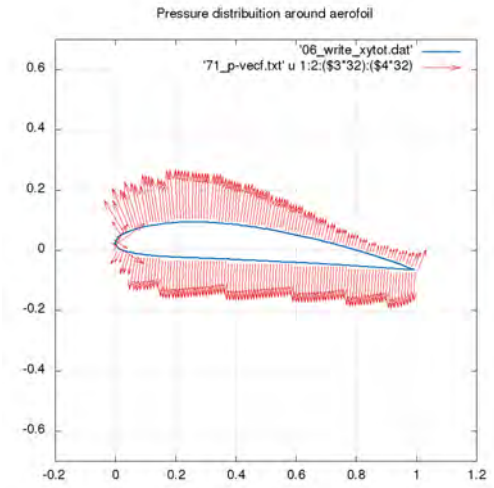

(a) Pressure around aerofoil (normal vectors shows magnitude).

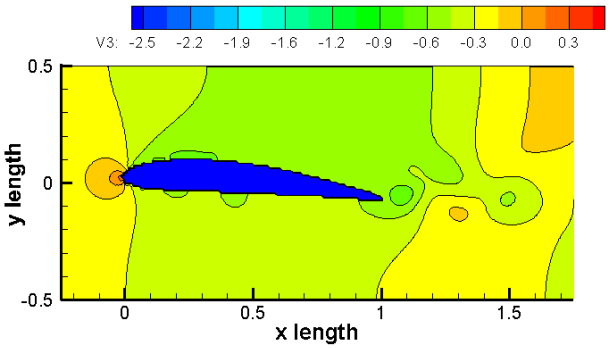

(b) Pressure field around aerofoil (contour plot).

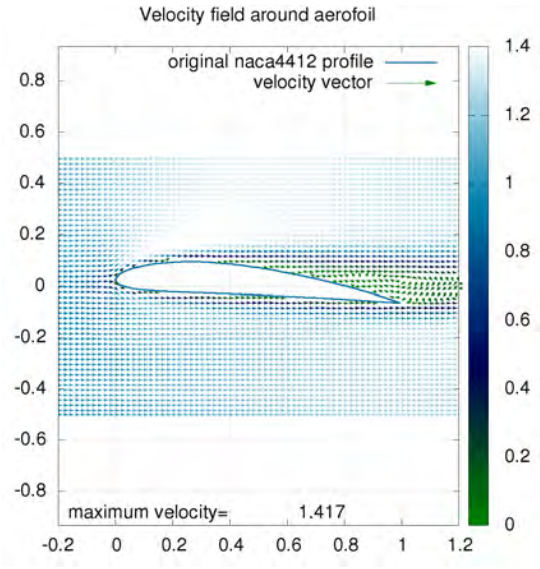

(c) Velocity field around aerofoil (coloured vectors shows magnitude).

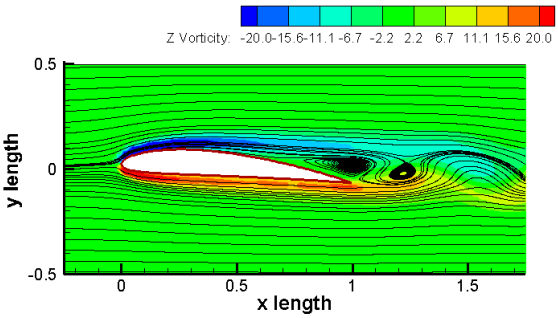

(d) Streamlines and z vorticity field.

Figure 3.30. Results around aerofoil for NACA 4412, at $\alpha = 5°$, at $Re = 1000$ for the present work.

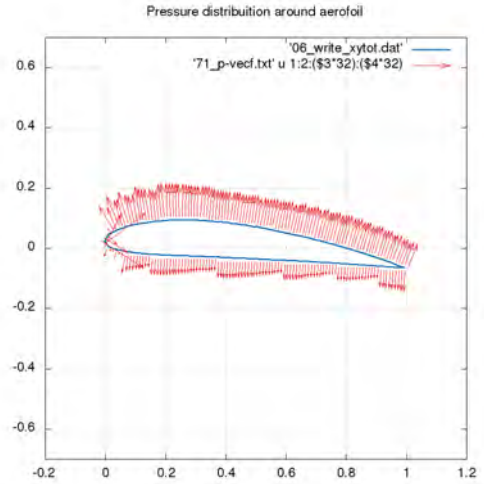

(a) Pressure around aerofoil (normal vectors shows magnitude).

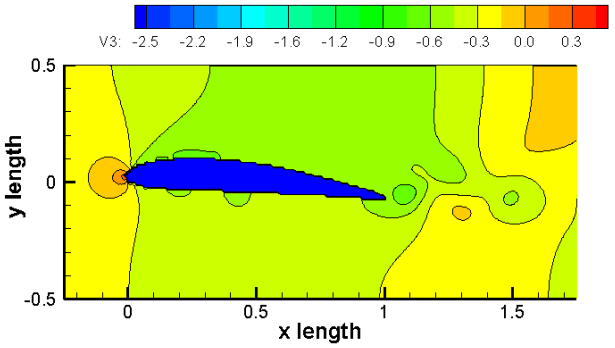

(b) Pressure field around aerofoil (contour plot).

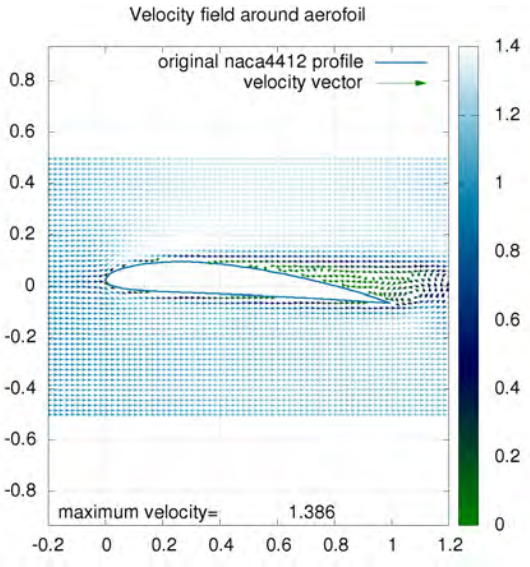

(c) Velocity field around aerofoil (coloured vectors shows magnitude).

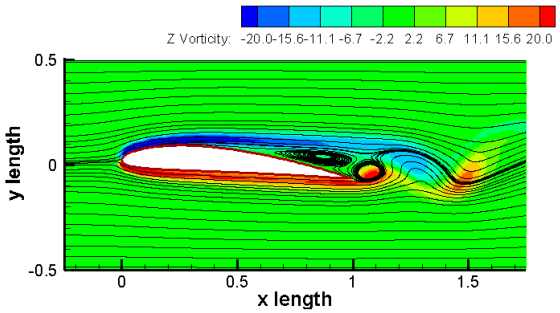

(d) Streamlines and z vorticity field.

Figure 3.31. Results around aerofoil for NACA 4412, at $\alpha = 5°$, at $Re = 2000$ for the present work.

Chapter 4

Results

4.1 HAWT blade case for study: NACA 0012.

Once the validation of our code of a flow over over an immersed streamlined body, we will proceed to consider a case of study using a NACA *0012* at $Re = 100$ as an exercise. In this case the low speed NACA *0012* symmetric aerofoil has been chosen as an object of study because it has been widely analysed. This simple geometry provides an excellent 2D validation case.

4.1.1 Computation of sections at a distance r from the rest.

For this case of study, eight cross-sections equally spaced along blade's length will be analysed, all of them using NACA 0012 airfoil but varying scale and the pitch angle β. The following parameters are required to completely define the study: First, the chord at the tip is defined as c_{tip} which has a normalized dimension of 1.0, as well an initial velocity of 1.0. The second fixed parameter is R, which is the total length. Then, the variables will be r, defined as $r = n \times c_{tip}$, where n is a required number of the times in order to distribute sections along R. See figure 4.1.

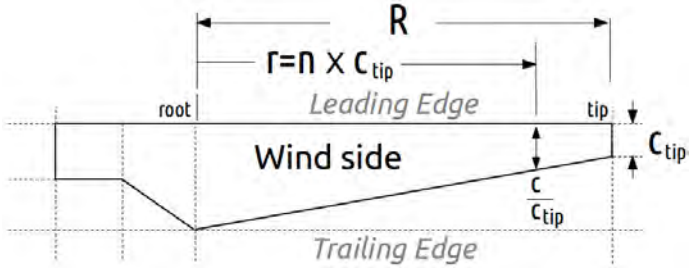

Figure 4.1. Default parameters of a theoretical blade used as inputs: $c_{tip} = 1.0$ and $R = 9.5$.

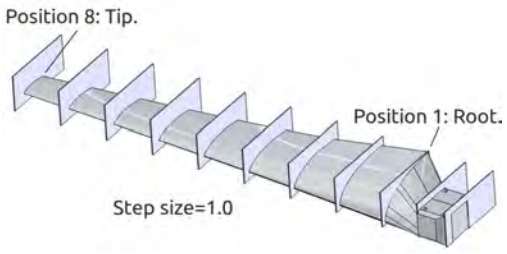

Figure 4.2. Selected blade sections for analysis. $Step\ size = 1.0$.

The chord at any location r will be given by $c_r = n \times c_{tip}$ (*i.e.* n times the tip chord. In the present work, we use the normalized chord, defined as $c_r = c/c_{tip}$ as a normalized dimension

ratio of an actual blade. Figure 4.1 shows each variable on a not to scale diagram. In figure 4.2 we show an illustration of the uniform distribution of eight selected sections, equally separated, along the blade span, going from 1 to 8 positions.

As explained in Chapter 1, the code requires input values that includes the twist angle and the chord length. For a better visualization and understanding of how geometry varies along blade span for each section computation, a collection of graphs are presented using $\alpha_D = 15°$ as an example. See figures 4.3 to 4.6 where the chosen non-dimensional geometric parameters are plotted as functionss of r/R, which is the normalized location along the blade, with a maximum value of 1.0 at the tip.

Figure 4.3 shows the non-dimensional chord c/c_{tip} which gives the typical planform shape. In this example c/c_{tip} reduces to 1.0 at the tip. Figure (4.4) shows the ratio between total radius R and the local chord $c(r)$: $R/c(r)$ which is the span times the local chord. We get the smallest value of this parameter at the root. The total span of the variable is from ~ 2.3 to 9.5.

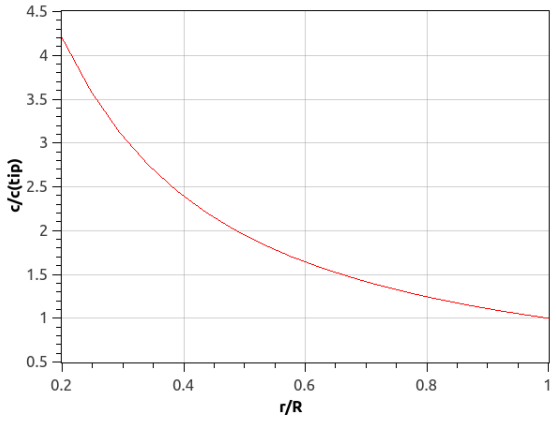

Figure 4.3. The normalized chord $(c(r)/c(R))$ as a function of the normalized span (r/R).

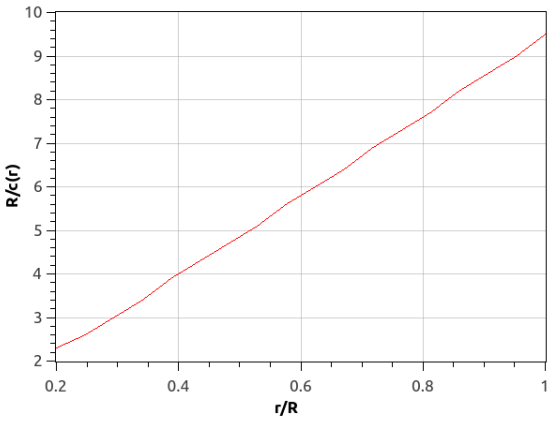

Figure 4.4. The normalized ratio $(R/c(r))$ as a function of the normalized span (r/R).

Figure 4.5 describes γ, ϕ and β as functions of the length of the blade using $\alpha_D = 15°$. From root to tip, $\gamma(r)$ that increases monotonically can be appreciated, while $\phi(r)$, and $\beta(r)$ decrease monotonically. Observe that are related by an offset $\beta(r)$ and $\phi(r)$. See figure 1.3 in chapter 1 for the description of these angles. In figure 4.6, the local velocity vectors $u(r)$ and $w(r)$, are plotted as functions of r/R. Notice the maximum value of $u(r)$, and $w(r) \approx 1.0$ at the tip of the blade, while $v(r)$ and v_w are kept constant. In a other words, inlet velocity value will vary for each section to solve.

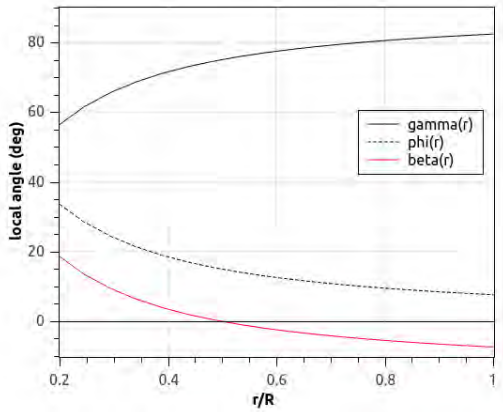

Figure 4.5. Local angle as a function of the normalized span (r/R) which is the twist along span. $\alpha_D = 15.0°$.

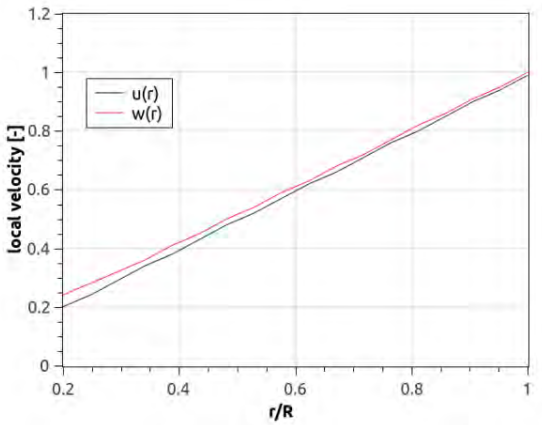

Figure 4.6. Local velocities ($u(r)$ and $w(r)$) as a function of the normalized span (r/R). $V_w = 0.1982$ and $V = 0.1321$.

It is important to clarify that inputs are not the same for all sections even for the same blade. See table 4.1 for the values used in the present study. We will compute each section at equally spaced r locations using consistent inputs.

Table 4.1. Parameters related to r locations.

Position	r	r/R	c/c_{tip}	$scale^a$	Domain size	dx, dy	dt	$itmax$	$u_x\ (= w_r)$
1.	2.5	0.263	3.420	3.4	6.80×5.10	0.034	0.0170	5882	0.292
2.	3.5	0.368	2.575	2.5	5.20×3.90	0.026	0.0130	7692	0.388
3.	4.5	0.474	2.050	2.0	4.00×3.00	0.020	0.0100	10000	0.488
4.	5.5	0.579	1.698	1.7	3.40×2.55	0.017	0.0085	11765	0.589
5.	6.5	0.684	1.447	1.4	2.80×2.10	0.014	0.0070	14286	0.691
6.	7.5	0.789	1.260	1.2	2.40×1.80	0.012	0.0060	16667	0.793
7.	8.5	0.895	1.115	1.1	2.20×1.65	0.011	0.0055	18182	0.897
8.	9.5	1.000	1.000	1.0	2.00×1.50	0.010	0.0050	20000	1.000

[a]Rounded value of c/c_{tip} for use as input in the code.

The total radius R is set to $R = 9.5 \times c_{tip}$, then r set goes from 2.5 at the root of the blade to 9.5 at the tip. In the present example, the chord goes from 3.420 at the root to 1.000 at the tip.

In order to calculate all eight scenarios, chord sizes were scaled, as well as domain sizes, in such a manner that total number of control volumes (ncv) were kept constant ($ncvx = 200$,

$ncvy = 150$), as well as the total time ($time = 100$). Scaling factors are listed in Table 4.1.

Figure 4.7 depicts the domain and airfoil at position 1 at the root overlaid upon position 8 at the tip, showing a size comparison between them. Input parameters will be set according to table 4.1 and obtained as described in subsection 4.1.1.

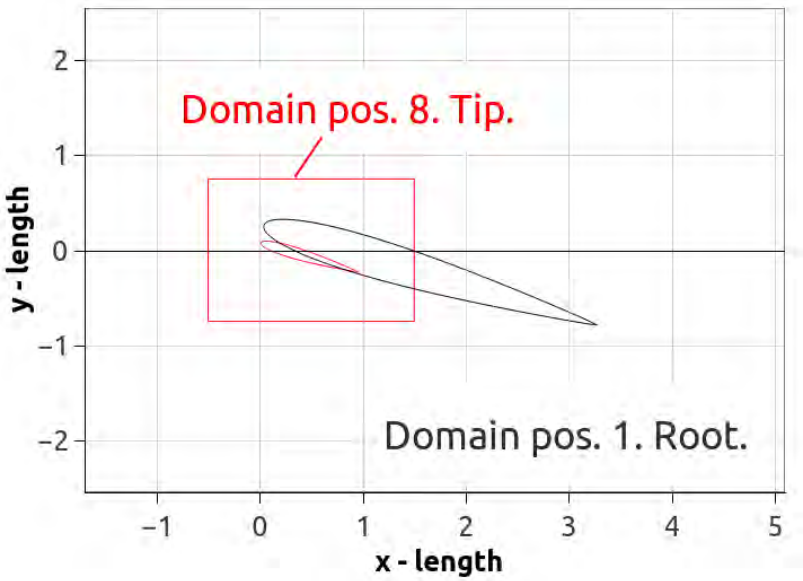

Figure 4.7. Domain size comparison between root position (1) and tip position (8).

Also, a ratio between control volume size and time step was kept constant, i.e. $dx/dt =$ constant. This is a factor used for the CLF condition as explained in Chapter 3, $u_x \frac{\Delta t}{\Delta x} \leq \mathrm{C}_{max}$, if $u_y = 0$. As expressed in Table 4.1, u_x must vary for each section.

Another consideration to keep in mind is that sections must twist with respect to the rotation plane of the HAWT, depending on β variation. Figure 4.8 illustrates this graphically for the present set of scenarios from a fixed point of view, showing the twist of the section along blade's length. This is just an explanatory diagram, not the one used in the computations.

4.1.2 Selection of C_L for L/D_{max}

Before the computation of selected sections is made, a previous step must be taken, since an adequate C_L must be found for L/D_{max}, while varying α (AOA) at the tip, i.e. at $r = R$. This value for C_L will be used for further computations. The selected value of α will be called α_D or design angle of attack.

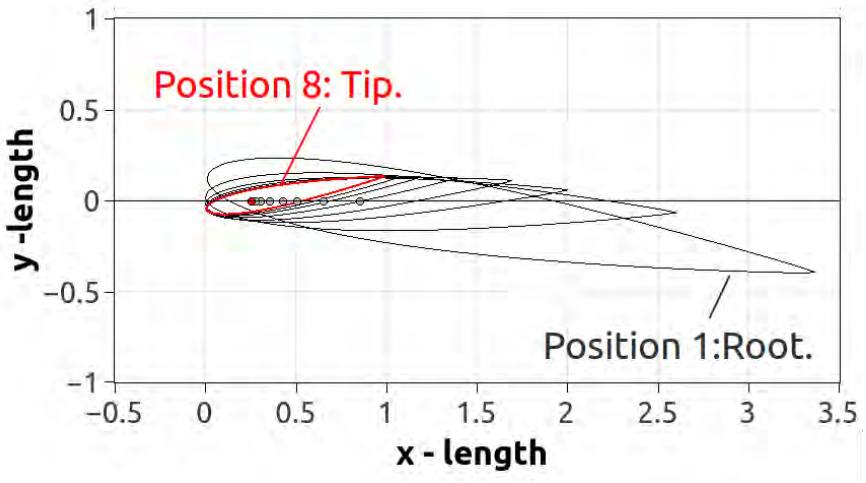

Figure 4.8. Aerofoil rotation according β angle.

Default inputs for running the code are shown in the following tables. In Table 4.2, the basic blade dimensions at the tip are shown and the computed velocities are presented in table 4.3 as inputs for the code.

Table 4.2. Input values for the study case.

Variable	Value
c_{tip}, (Chord at tip)	1.0
R, (Total radius)=	9.5
λ, (TSR at tip)=	5.0
B, (number of blades)=	3
Aerofoil name	NACA 0012

Table 4.3. Computed variables.

Variable	Value
$v_w = v_1 =$	0.1982
$v = v_2 =$	0.1321
$u_{tip} =$	0.991
$w_{tip} =$	1.000
$\alpha_D =$	at L/D_{max}

Default inputs are shown in Tables 4.4, 4.5 and 4.6 for the domain and time parameters at the tip, as well as numerical schemes, initial and boundary conditions. All these values will be used as default, unless other inputs are explicitly declared or specified.

Domain sizes are given in Table 4.7. The results trends are very similar for these selected scenarios, results are sensitive to domain size as shown in graphs 4.9 - 4.12. Recall that in the square-cylinder validation presented in Chapter 2, solution is sensitive to domain size. We confirm that this is a influential parameter to establish. In order to obtain several qualitative results we will use the small domain sizes due resource saving, thus presented results may differ from quantitative real solution.

Table 4.4. Domain and time inputs for run validation

Item	Input
Grid type	Cartesian/structured
Control volume size, $dx \times dy$	0.010×0.010
Domain size, $x \times y, y-$centered	20×5
Number of control volumes, $nx \times ny$	400×100
Time step, dt	0.005
Number of time iterations, $itmax$	20,000
Iteration tolerance	1E-4
Total elapsed time units, $time$	100
Maximum number of iterations, $maxiter$	100

Table 4.5. Values for NACA 0012 run validation.

Item	Value
Re	100
Inlet velocity, $U(= w_{tip})$	~ 1.0
Chord at tip, c_{tip}	1.0
Leading edge location	x=0.0, y=0.0
Rotation location	Aerodynamic center

Table 4.6. Schemes and conditions for run validation.

Item	Value
Scheme	Central Diff.
Boundary conditions on Top/Btm walls	Free-slip
Time scheme	Implicit
Formulation type	Simplec

We use graphs shown in figure 1.14 to compare the behaviour and trends of main results: Notice that as expected, C_D tends to grow as AOA increase. See figure 4.9. However, same behaviour for C_L is not found: As shown in figure 4.10, C_L increases up to the last value of the AOA, while a sudden drop expected at $\sim 15° - 20°$ does not occur.

Table 4.7. Domain size scenarios

Domain	Size $x \times y$	x dim	y dim	cv
Domain 1 size,	2.0×1.5	$-0.5, 1.5$	$-0.75, 0.075$	200×150
Domain 2 size,	2.0×1.5	$-0.5, 1.5$	$-1.00, 0.050$	200×150
Domain 3 size,	2.5×1.5	$-0.5, 2.0$	$-1.00, 0.050$	250×150

The plot of figure 4.11 shows a typical behaviour of the relation between C_L-C_D. Figure 4.12 shows how L/D_{max} ratio is reached at $\sim 18 - 20°$ in the $AOA - L/D$ graph. It should be

remembered that the used Re number is very low, which may be a reason for the discrepancy.

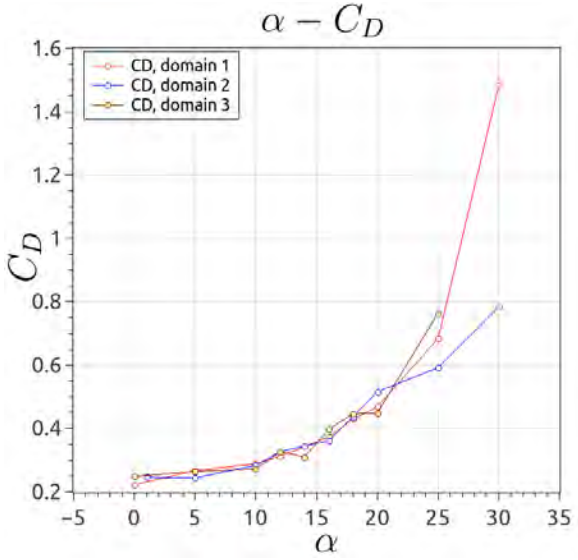

Figure 4.9. Drag coefficient (C_D) as a function of the angle of attack (α) for different integration domains.

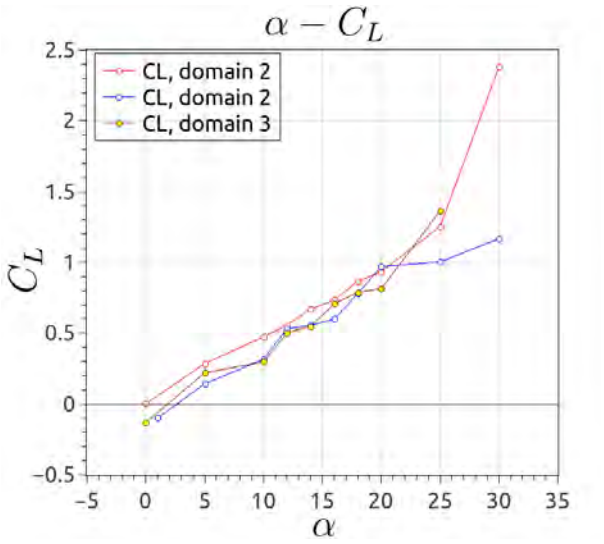

Figure 4.10. Lift coefficient (C_L) as a function of the angle of attack (α) for different integration domains.

The influence of the domain size on the pressure for the same input parameters and aerofoil features, is shown in figure 4.13. The pressure around airfoil comparative chart for various domain sizes shown in figure 4.13 helps in the visualization and selection of the different scenarios. Given the calculation results presented above, the integration domain selected for the presented study is Domain 1. Additionally, the AOA is chosen as $\alpha = 18°$ according to figure 4.12.

Results are quite different considering the problem is that the same (up to 87% in the farthest point at the normalized location around the airfoil of 0.8, see figure 4.13), and the only variable is just the domain size, which we may say is not strictly part of the problem. Therefore here we can conclude it is important to take care of this point as well as carefully considering all container boundaries conditions because of its determinant influence on the solution.

Once α_D is selected, it is important to take into account other considerations. As mentioned above, and as described in the table 4.1, there will be a domain scaling for each section, as the chord length of each profile will also change.

The following validation strategy which serves to display the change in response due to scaling, was done. The integration domain was scaled by a factor of two ($\times 2$) and four ($\times 4$), resizing both control volumes and the time step ($t = 0.005$, 0.010 and 0.020) while keeping

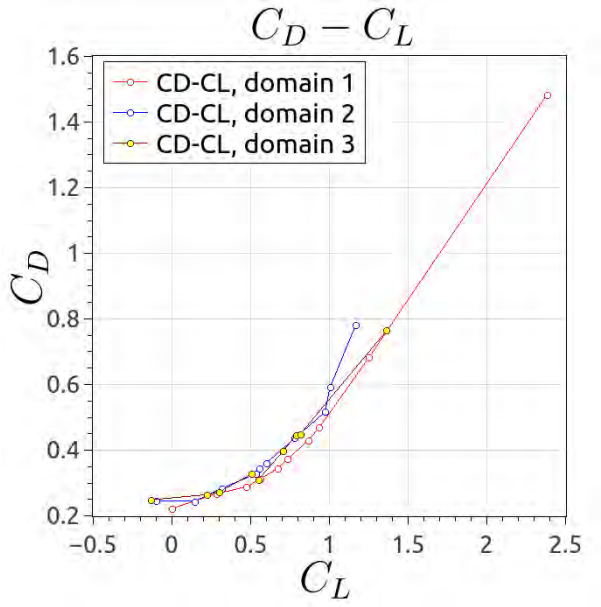

Figure 4.11. Drag coefficient (C_D) as a function of the lift coefficient (C_L) for different integration domains.

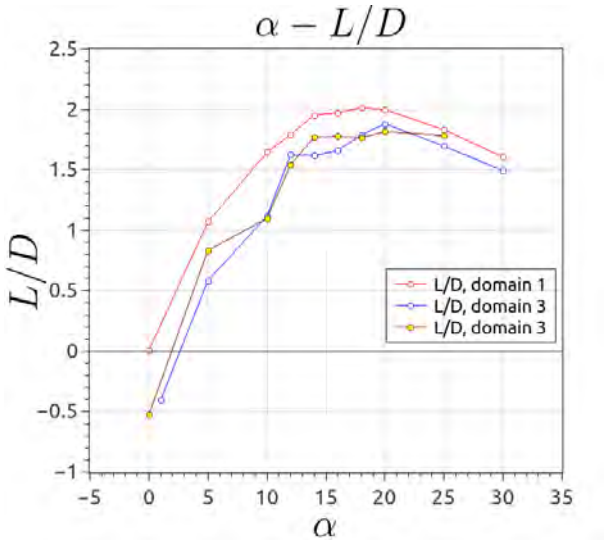

Figure 4.12. Lift-to-drag ratio coefficient (L/D) as a function of the angle of attack (α) for different integration domains.

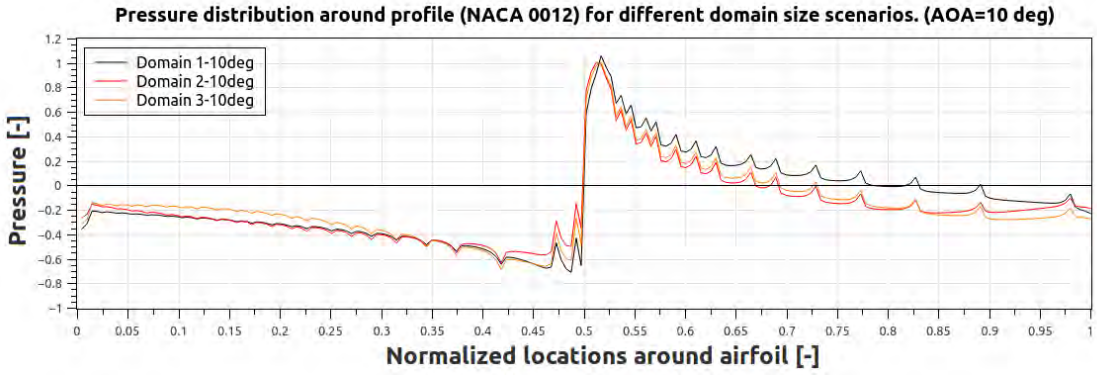

Figure 4.13. Pressure comparative around airfoil for different domain sizes.

udx/dt ratio fixed. The results are shown in Figure 4.14. Most of the pressure profiles are similar, but, in some cases the pressure shows an abnormal distribution on the upper surface, attributable mainly to the proximity of the upper and lower borders and at the eastern border (outflow), and which may warn us of possible errors.

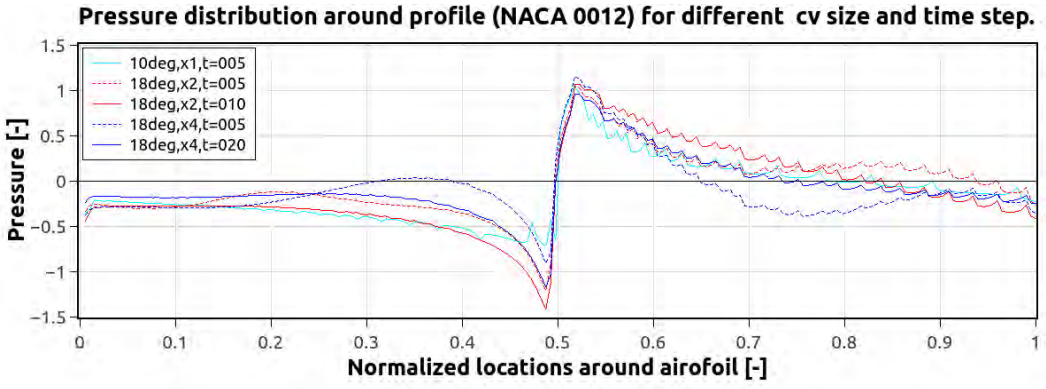

Figure 4.14. Pressure comparative around the airfoil for different cv size and time step.

4.1.3 Results at selected r locations along blade's length for NACA 0012.

The pressure, shear stress, velocity and streamlines are shown in the following sets of figures from 4.16 to 4.23 computed for each section. Each set shows figures with the following format:

(a) The box placed at the left of the upper row contains the basic parameters required for the calculation. Information is given for the velocities triangle and their angles, also C_L, C_D and L/D are shown. Notice that AOA, rotor plane and rotor axis are plotted along with the profile, and vary its position while $w(r)$ direction remains fixed.

(b) Pressure field around aerofoil. Pressure field is shown using a contour plot. Maximum and minimum values are displayed.

(c) Pressure normal distribution around aerofoil. Normal force vectorial components derived from pressure acting over the solid are displayed. The length of the vectors denotes magnitude, and the direction denotes positive or negative pressure as the case may be.

(d) Tangential velocity (Shear stress) around aerofoil. Tangential velocities are plotted at the boundary of the airfoil. The length of the vectors denotes magnitude. Also direction confirms a correct computation.

(e) Velocity field around aerofoil. Vector field is shown representing the velocities within the flow. A color code is used to denote magnitude.

(f) Streamlines around aerofoil. The streamlines are shown for a clear visualization of the air motion pattern.

A reference diagram is shown in figure 4.15 as a helping key, useful to visualize graphical results further on. The relative frame is rotated in such a manner that the apparent velocity $w(r)$ direction keeps fixed, staying parallel to horizontal $x-$ axis and is a reference for defining α_D; therefore, lift force (C_L) will acquire $y-$ direction. Rotation plane and rotation axis of the HAWT are plotted as relative references that may vary depending upon pitch angle β. The scheme shows the velocities and the angles at a given distance r from the rotor axis. To design the rotor we have to define the pitch angle $\beta(r)$ and the chord length $c(r)$ at each r location, thus both of them depend on the given radius.

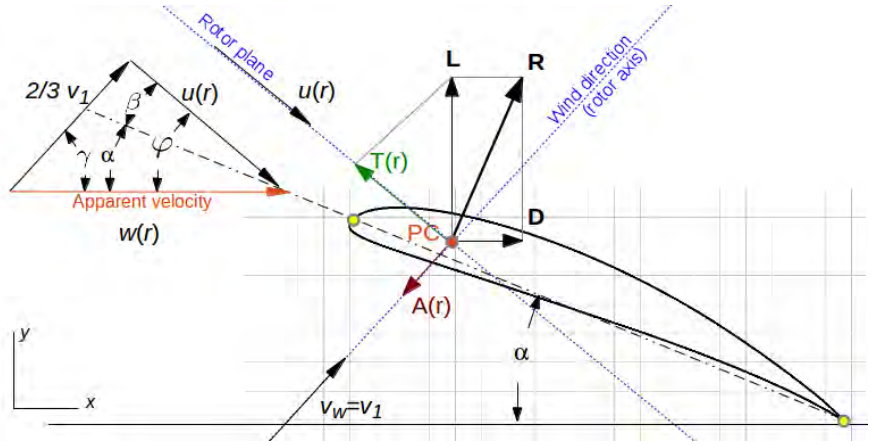

Figure 4.15. Scheme showing plot reference point of view. (Explanatory picture). A general airfoil profile is used for illustration.

The blade is moving upwards, but in figure 4.15, it moves in the $T(r)$ (Torque) direction, relative to the rotation reference plane and against $u(r)$ velocity. It is also pertinent to remind that we are following Betz theory which does not include rotation of the wind.

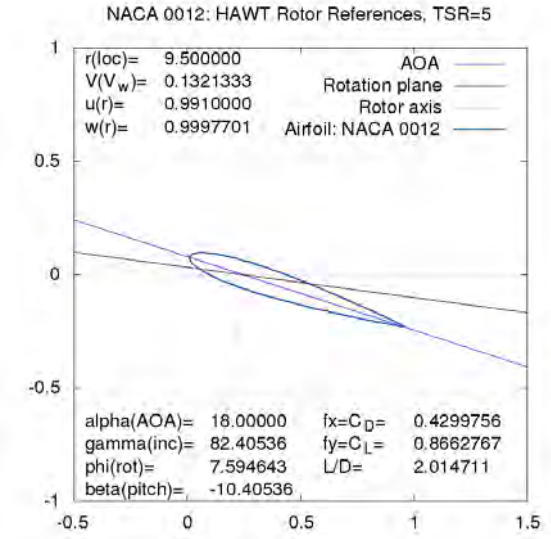

(a) Results summary

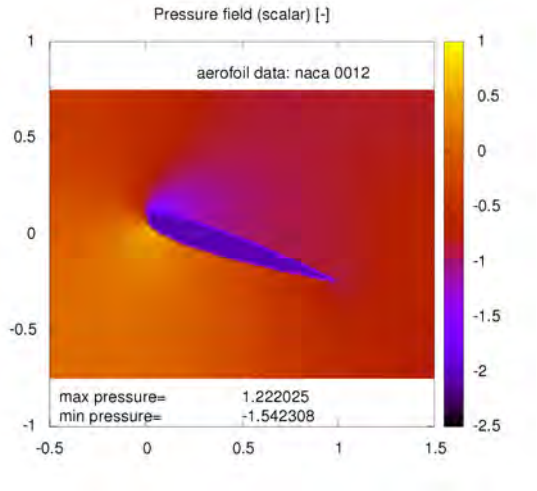

(b) Pressure field around aerofoil

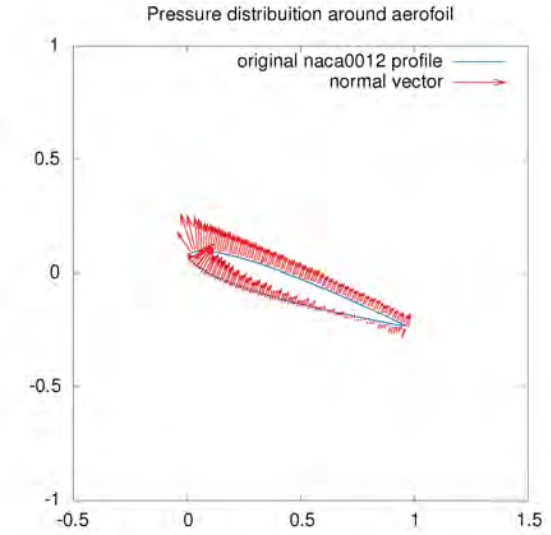

(c) Pressure distribution around aerofoil

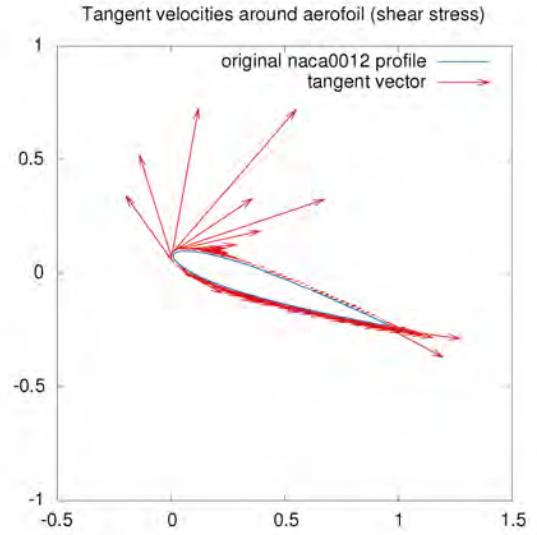

(d) Tangential velocity (Shear stress)

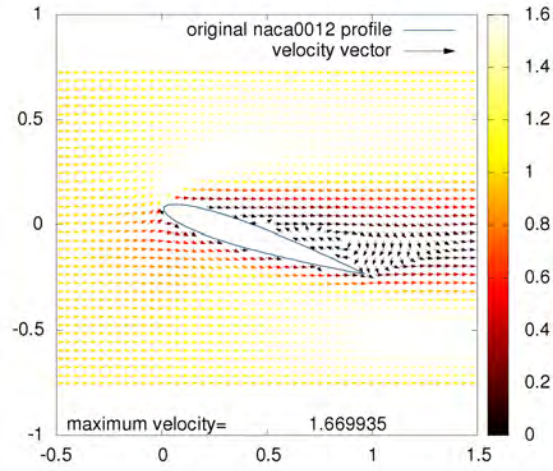

(e) Velocity field around aerofoil

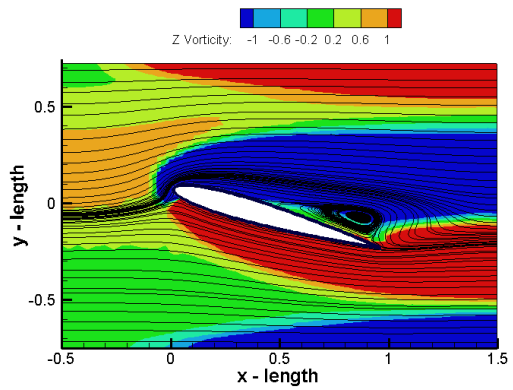

(f) Streamlines-vorticity around aerofoil

Figure 4.16. Outputs around aerofoil at $r = 9.5$ location.

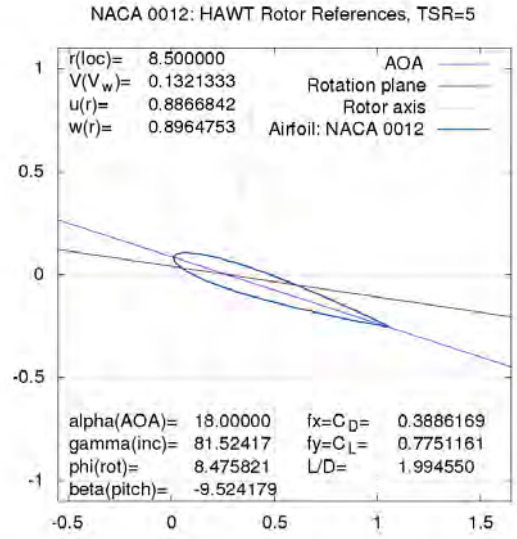

(a) Results summary

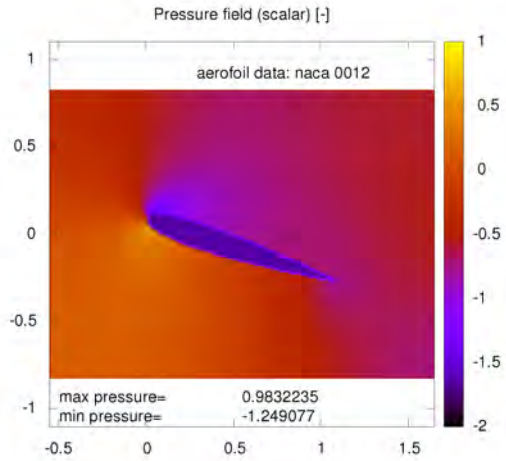

(b) Pressure field around aerofoil

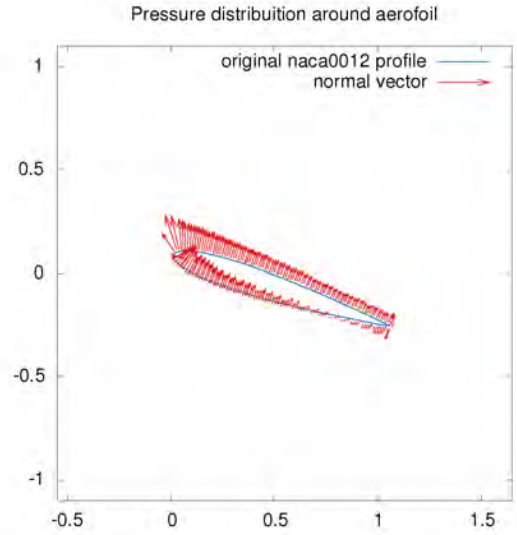

(c) Pressure distribution around aerofoil

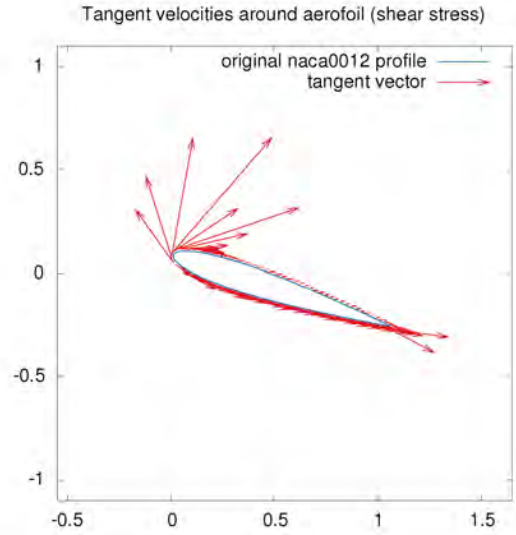

(d) Tangential velocity (Shear stress)

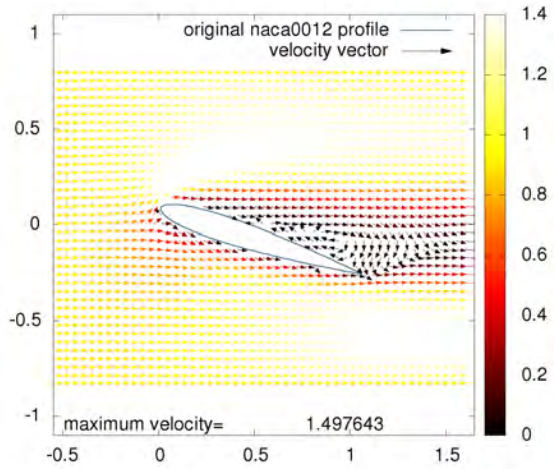

(e) Velocity field around aerofoil

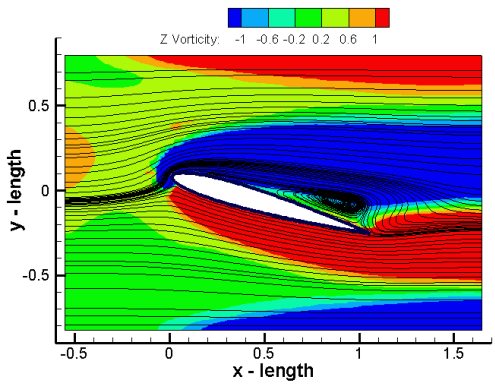

(f) Streamlines-vorticity around aerofoil

Figure 4.17. Outputs around aerofoil at $r = 8.5$ location.

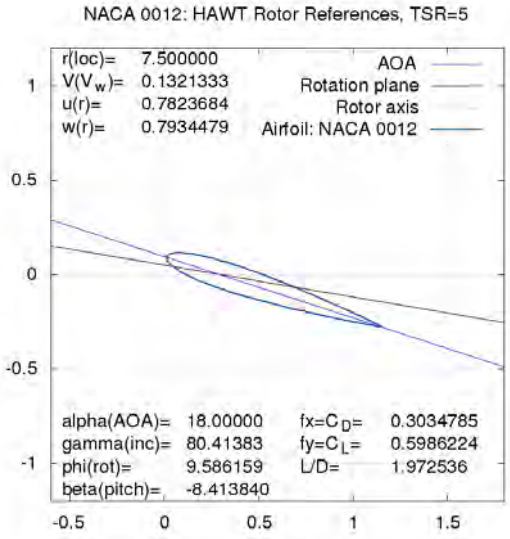

(a) Results summary

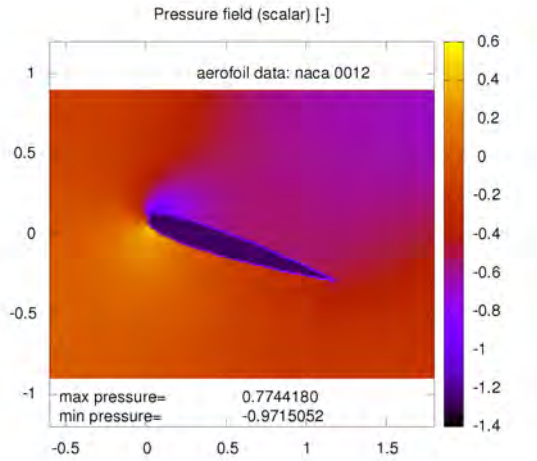

(b) Pressure field around aerofoil

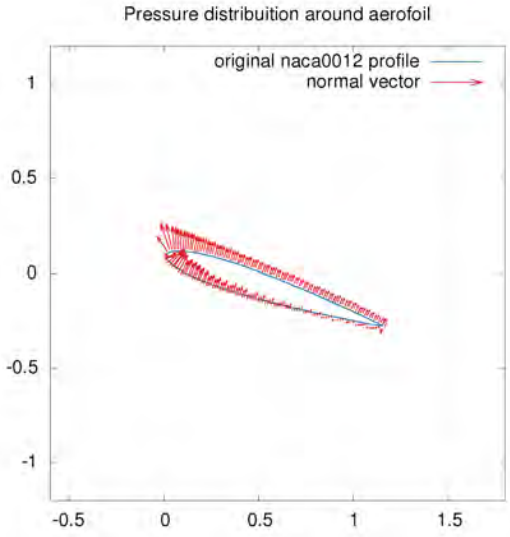

(c) Pressure distribution around aerofoil

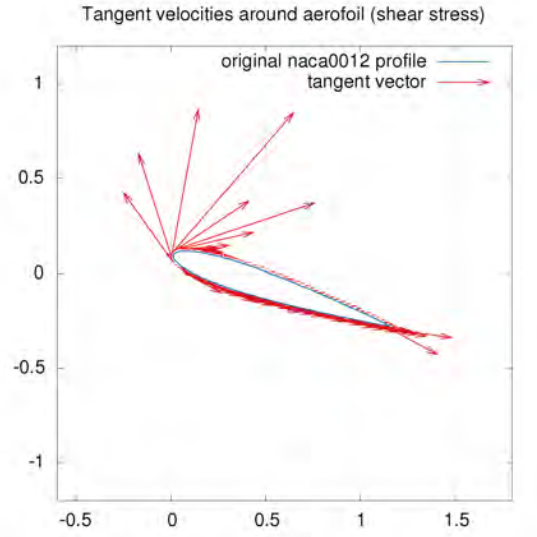

(d) Tangential velocity (Shear stress)

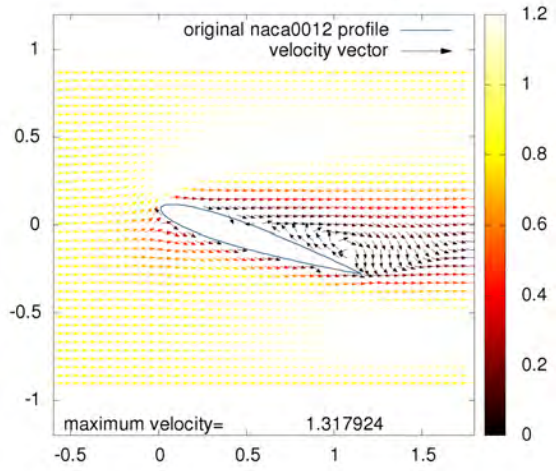

(e) Velocity field around aerofoil

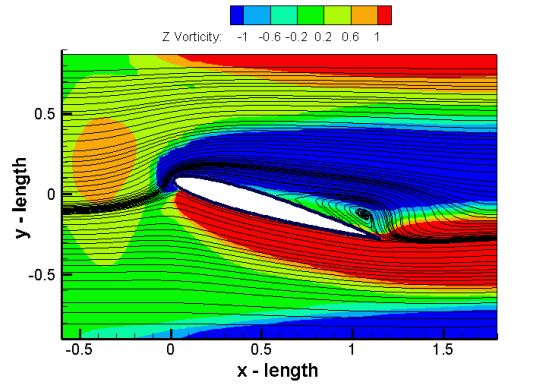

(f) Streamlines-vorticity around aerofoil

Figure 4.18. Outputs around aerofoil at $r = 7.5$ location.

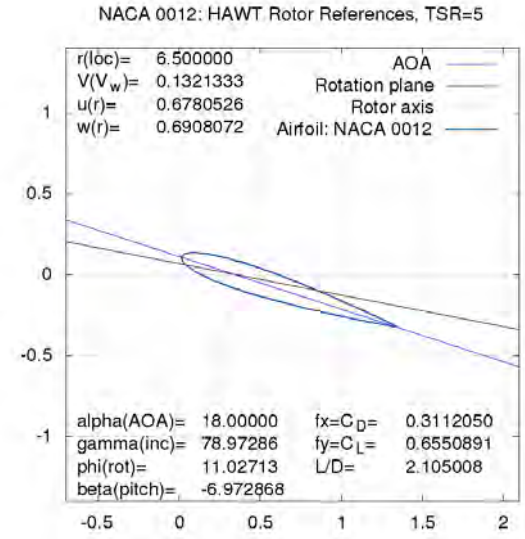

(a) Results summary

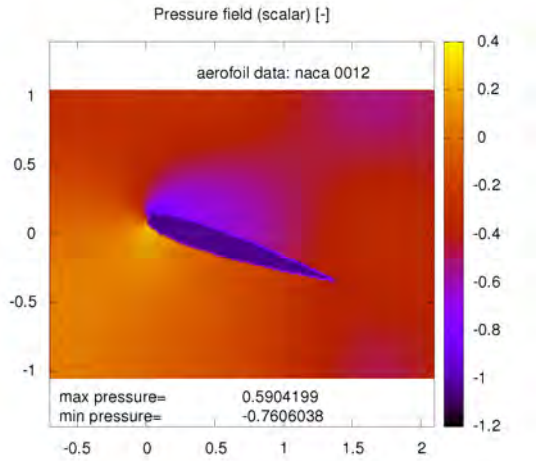

(b) Pressure field around aerofoil

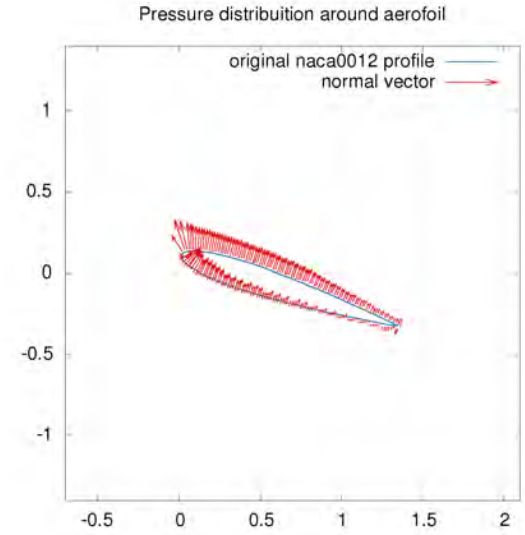

(c) Pressure distribution around aerofoil

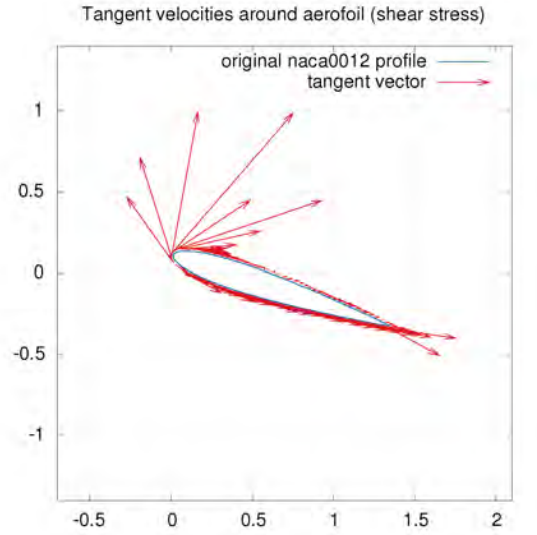

(d) Tangential velocity (Shear stress)

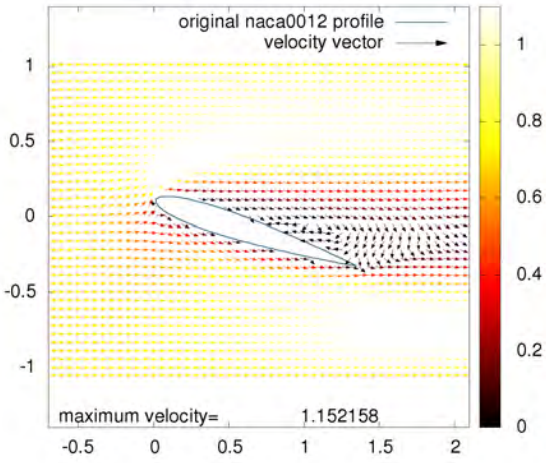

(e) Velocity field around aerofoil

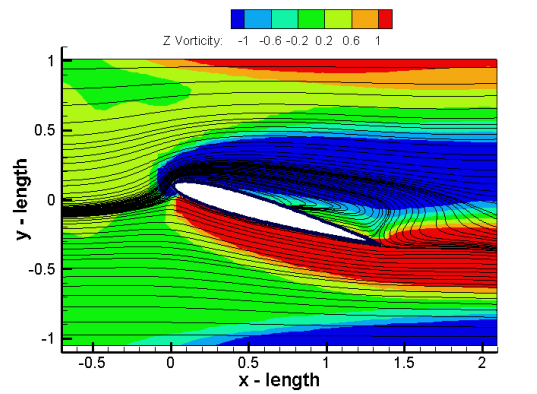

(f) Streamlines-vorticity around aerofoil

Figure 4.19. Outputs around aerofoil at $r = 6.5$ location.

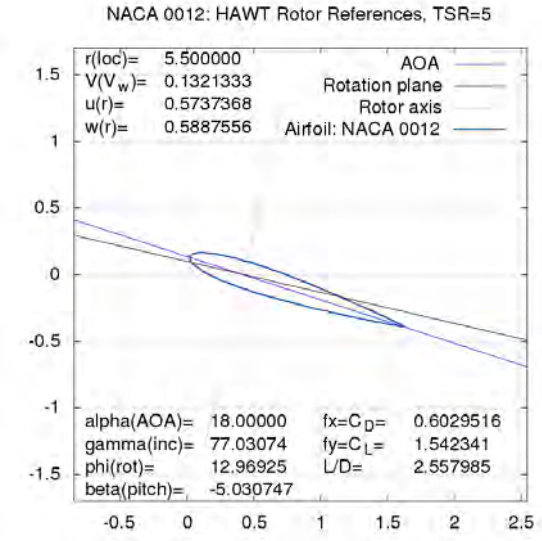

(a) Results summary

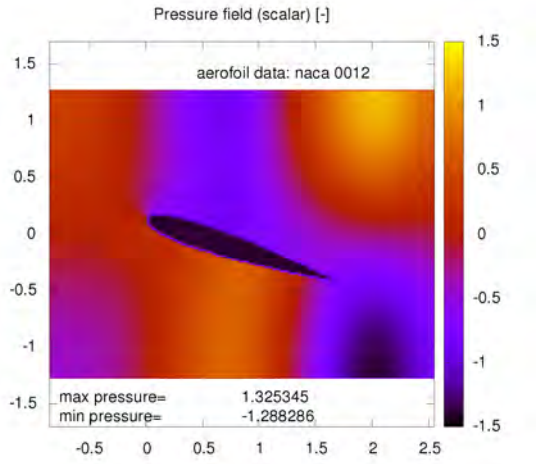

(b) Pressure field around aerofoil

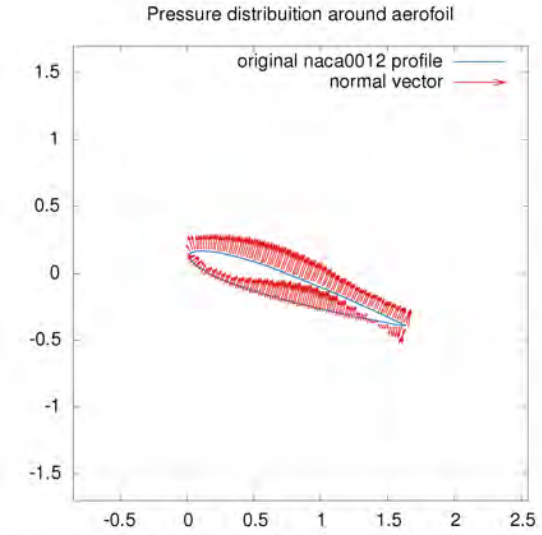

(c) Pressure distribution around aerofoil

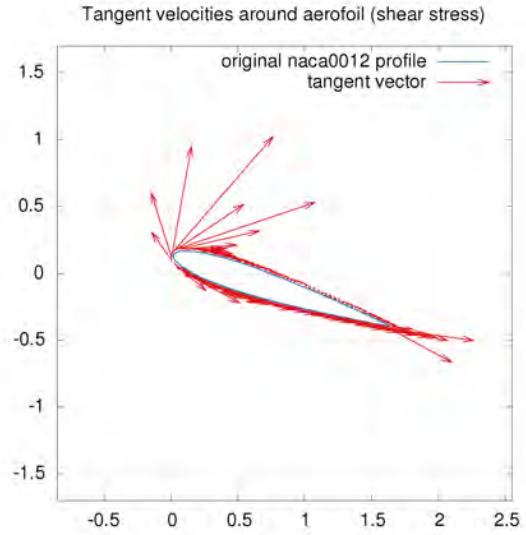

(d) Tangential velocity (Shear stress)

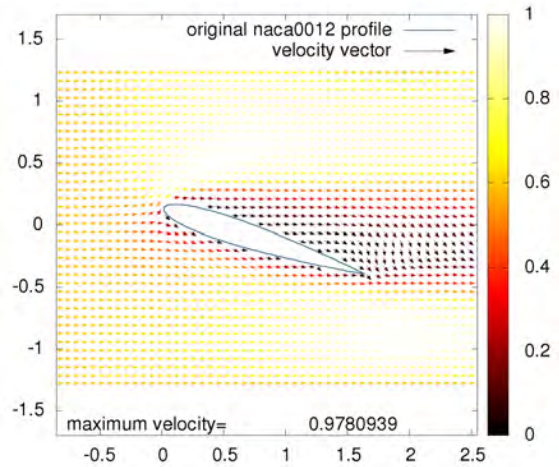

(e) Velocity field around aerofoil

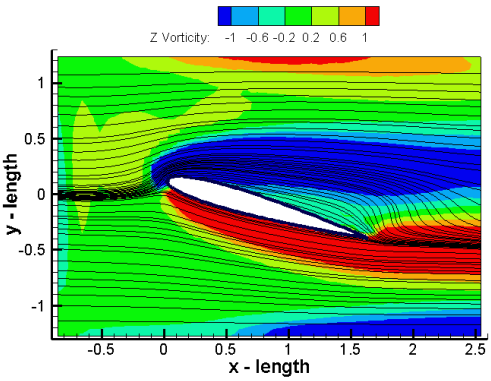

(f) Streamlines-vorticity around aerofoil

Figure 4.20. Outputs around aerofoil at $r = 5.5$ location.

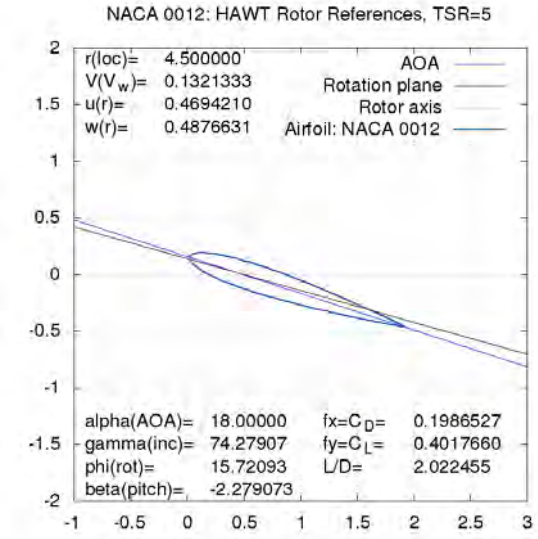

(a) Results summary

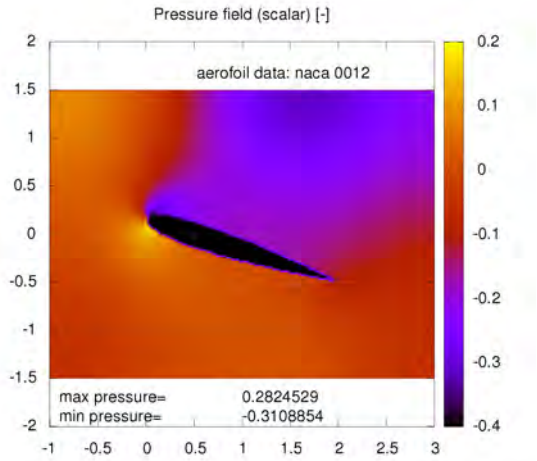

(b) Pressure field around aerofoil

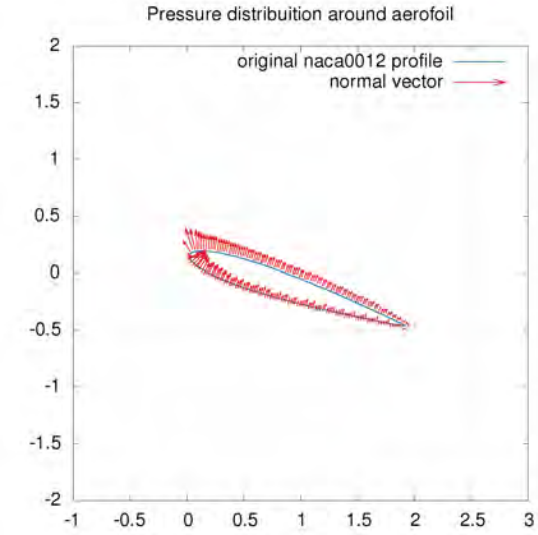

(c) Pressure distribution around aerofoil

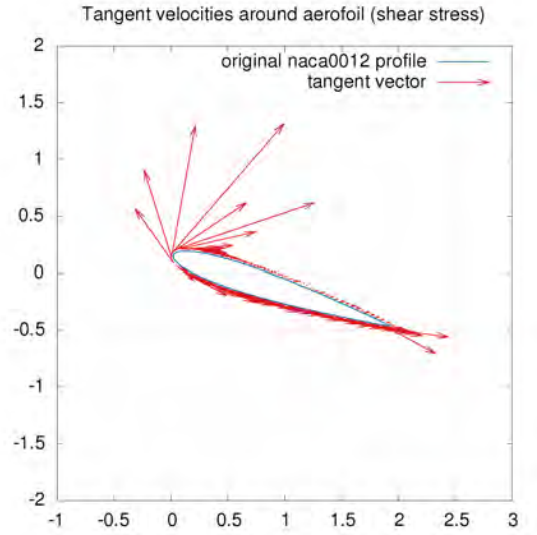

(d) Tangential velocity (Shear stress)

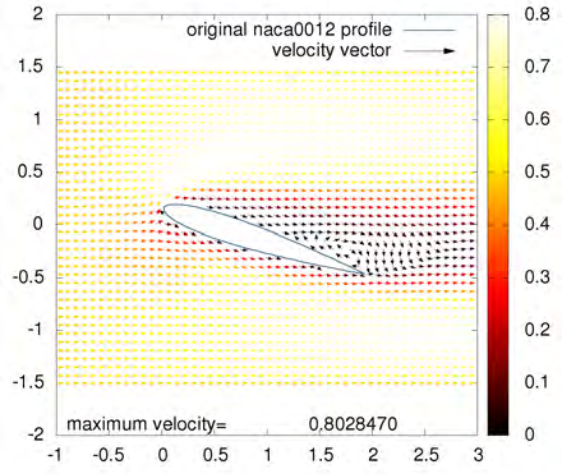

(e) Velocity field around aerofoil

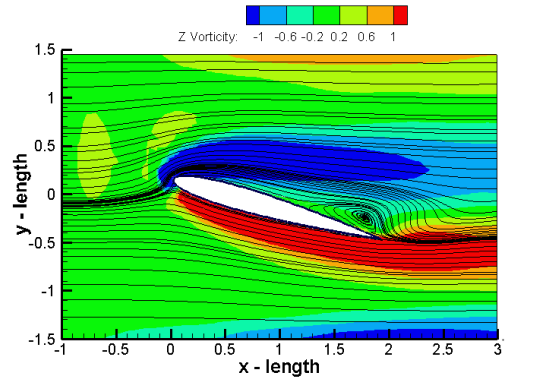

(f) Streamlines-vorticity around aerofoil

Figure 4.21. Outputs around aerofoil at $r = 4.5$ location.

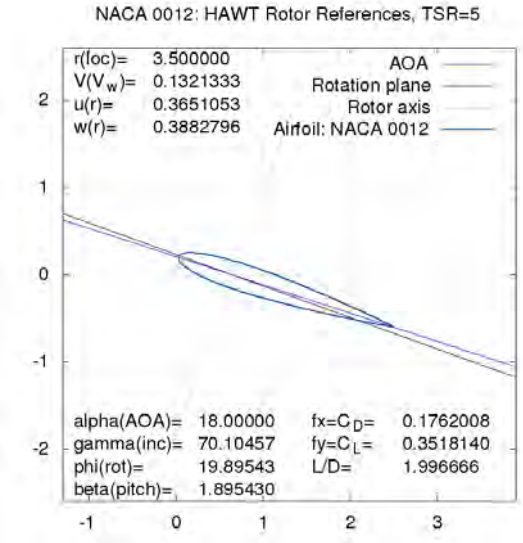

(a) Results summary

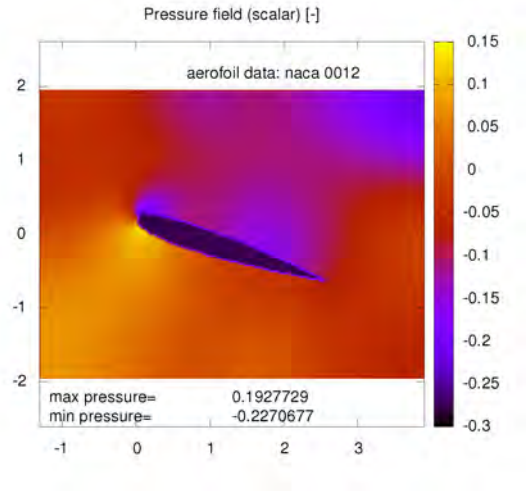

(b) Pressure field around aerofoil

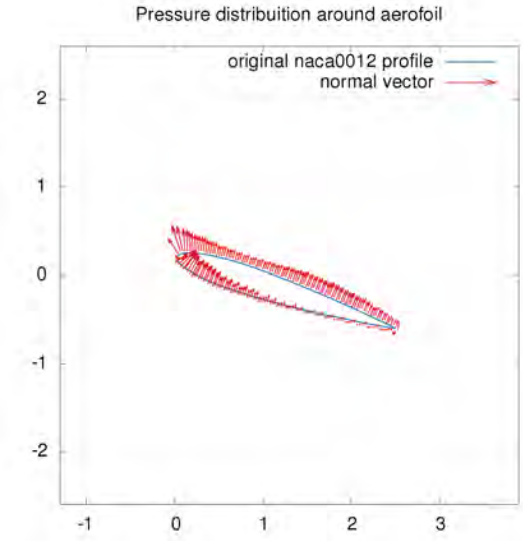

(c) Pressure distribution around aerofoil

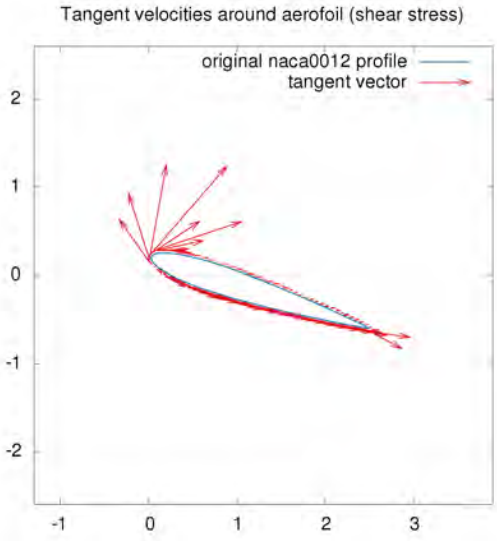

(d) Tangential velocity (Shear stress)

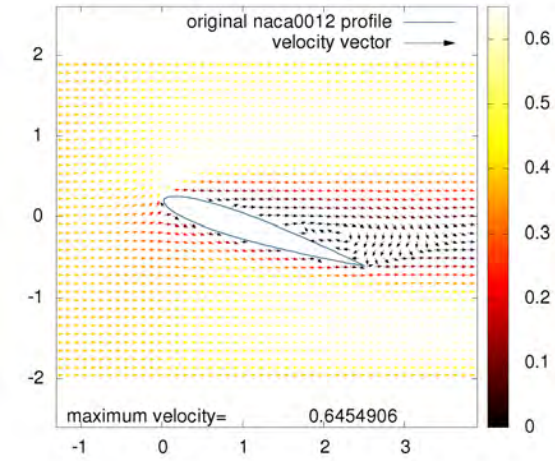

(e) Velocity field around aerofoil

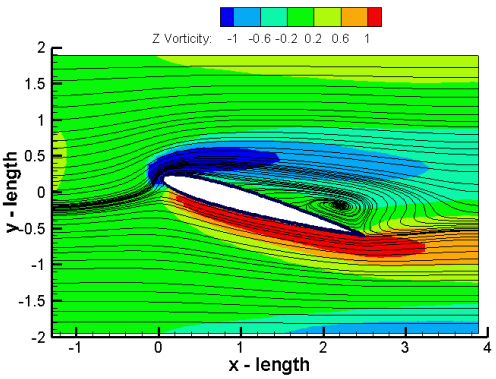

(f) Streamlines-vorticity around aerofoil

Figure 4.22. Outputs around aerofoil at $r = 3.5$ location.

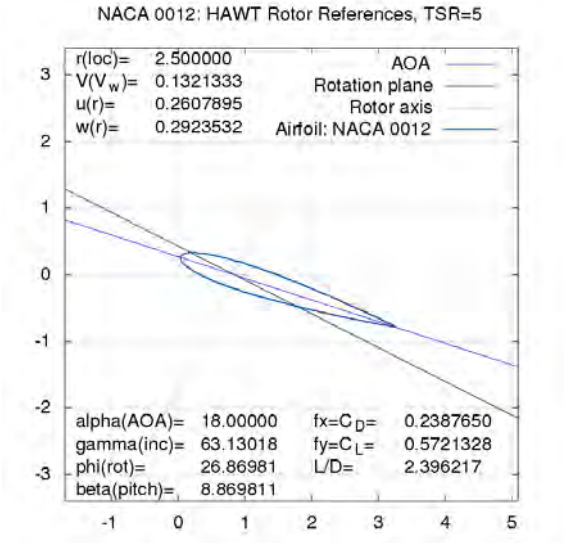

(a) Results summary

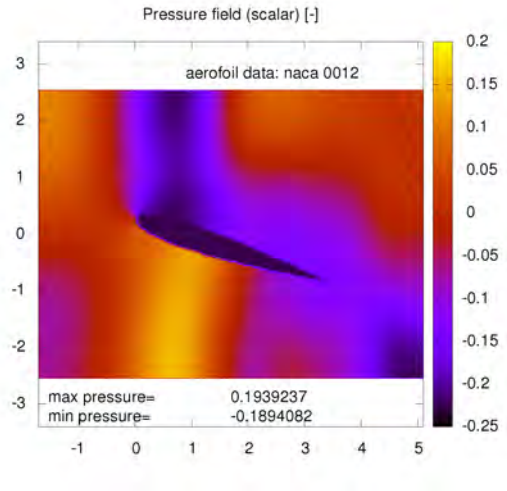

(b) Pressure field around aerofoil

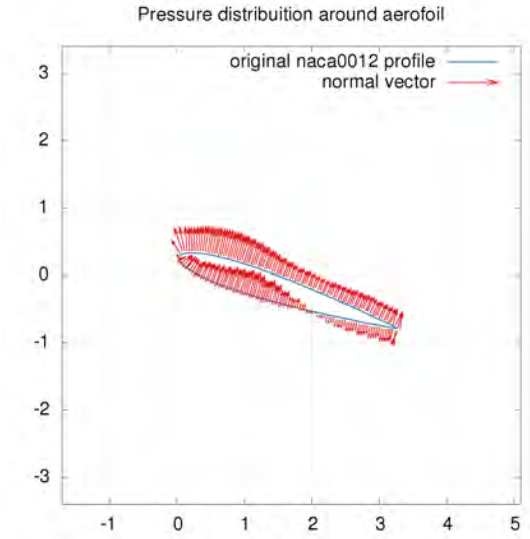

(c) Pressure distribution around aerofoil

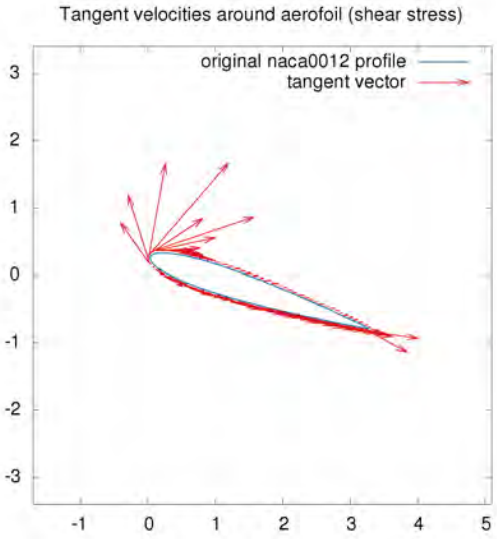

(d) Tangential velocity (Shear stress)

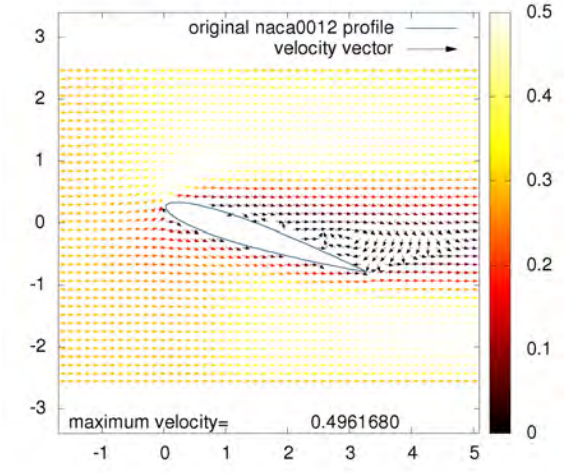

(e) Velocity field around aerofoil

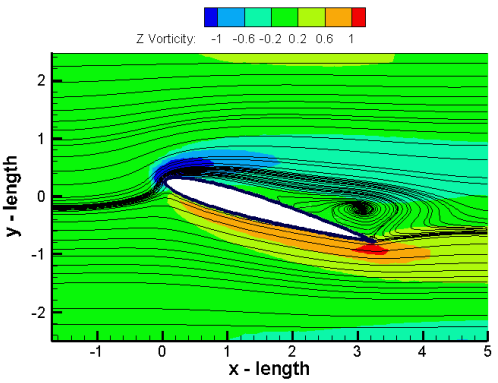

(f) Streamlines-vorticity around aerofoil

Figure 4.23. Outputs around aerofoil at $r = 2.5$ location.

4.1.4 Discussion.

The pressure field and surface distribution presented in panels (b) and (c) is conveniently interpreted in terms of the distribution shown in figure 4.24 where the pressure distribution around the aerofoil for each section. A decrease in pressure magnitude may be appreciated as the section approaches the root. This is due to a decrease in the velocity with respect to the tip where the velocity $w(r)$ reaches its highest value because $u(R) = u_{max}$. Total force is expected to increase for each section due to the area increment as described in table 4.1 (See chord size variation).

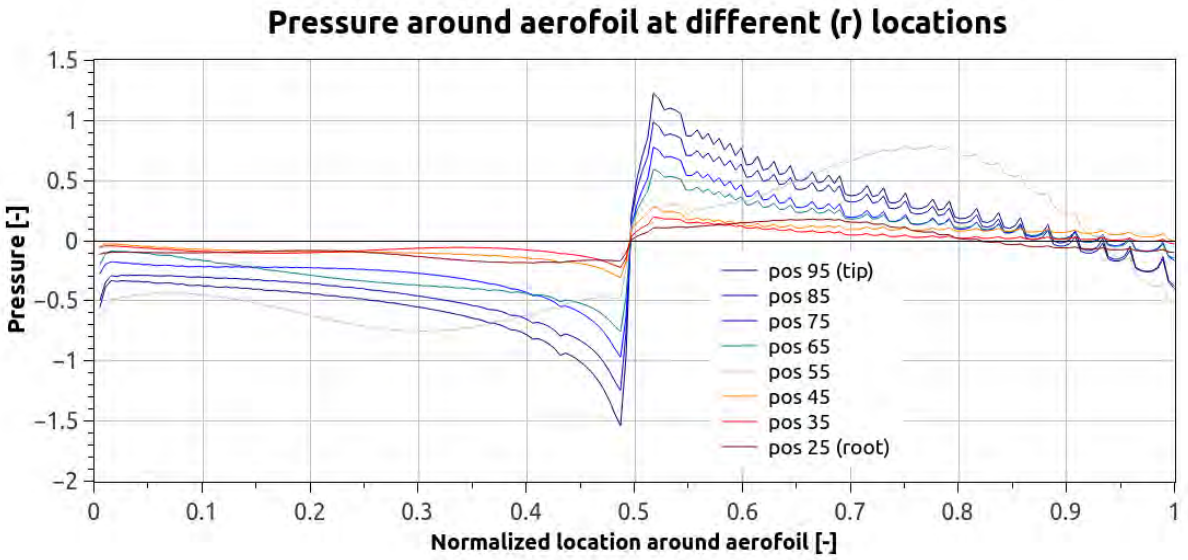

Figure 4.24. Pressure comparison around airfoil for different r locations.

As the sections get closer to the root, the forces increase and the structure may require a higher *thick/chord* ratio, mostly in high power wind turbines, clearly affecting the aerodynamic performance. For the aerodynamic comparison for the present work, the section profile remained the same, changing only the size of the section.

A comparison between $w^2\ c/c_{tip}$ (i.e. the product of the main variables that define the aerodynamic lift force), and the resulting force F_L $(= F_y)$ obtained numerically is shown in figure 4.25 where there is a clearly rising trend towards the tip, explaining why a maximum amount of energy is extracted from the region close to the tip.

Figure 4.26 shows $F_x - F_y$ where some points *(gray)* (out of the main trend *(red)*) are plotted independently due to an abnormal dispersion, probably because numerical errors show up

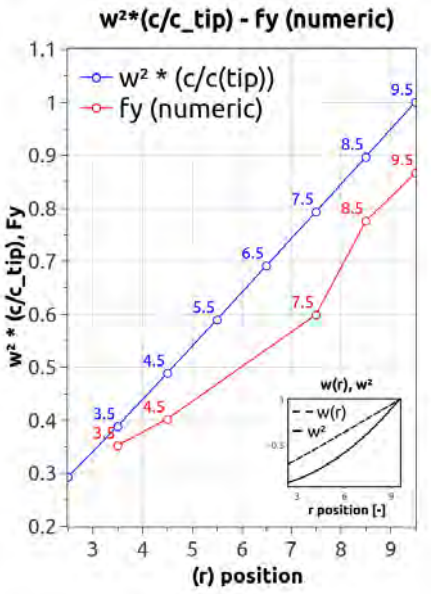

Figure 4.25. r locations - $w(r)$,w^2.

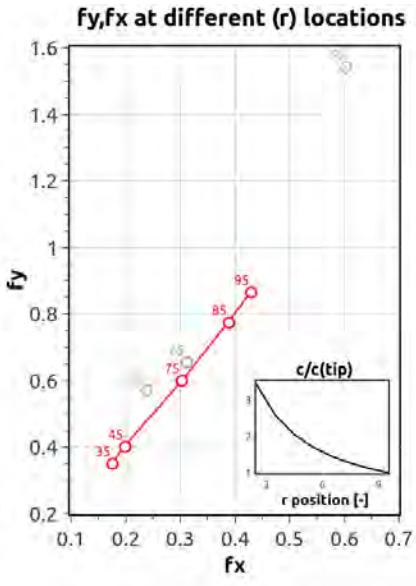

Figure 4.26. F_x - F_y.

after scaling the domain (See figure 4.7). Small boxes within the graphs show single variables w^2 and c/c_{tip} trending along r as a reminder. This proves that the torque distributions at blade the tip region will be larger than root region.

Due to the variations of tangent velocities at monitored control volumes near the solid boundary, a moving average filter was used. In order to reduce leaps in the magnitude of velocities caused by the staggerred topology of the solid domain, and for solving boundary equations in the fluid domain, Matlab's 1D digital filter function was applied. Figure 4.27 shows all shear-stress averages for all positions. In the small box at the right top corner, a comparative between the original data and the moving average is shown for the position at the tip (95).

The sum of forces exerted over each section is the total force exerted over the entire hypothetical blade. Before running all eight scenarios, we confirmed consistency at each preliminary result, such as scaling, domain size and the behaviour of polar curves.

4.2 Closing remarks.

Once the calculations of forces on the blade are done, the torque and power may be computed. Several methods may be used considering the results obtained but they shall not

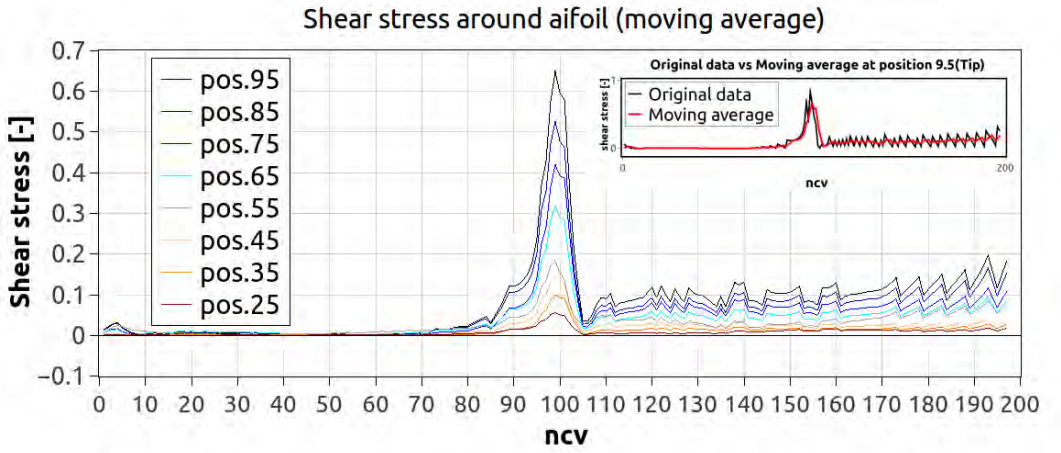

Figure 4.27. Shear stress comparative around airfoil for different r locations.

be described here. For example, the calculation of torque and power developed by a rotor requires knowledge of the flow induction factors, which are obtained by solving the BEM equations. The maximum power coefficient occurs at a tip speed ratio for which the axial flow induction factor a, which in general varies with radius, is closely approximated to the Betz limit value of 1/3.

At lower tip speed ratios the axial flow induction factor can be much less than one third and the aerofoil angles of attack are high, leading to stalled conditions. For most wind turbines, stalling is much more likely to occur at the blade root because of practical constraints; the built-in pitch angle β of a blade is not large enough in that region. Blade stalling causes a significant loss of power at low tip speed ratios.

At high tip speed ratios where the axial induction factor (a) is also high, the angles of attack are low and drag begins to predominate. Therefore, at both high and low tip speed ratios, the drag is high and the general level of the axial induction factor is not optimal, so the power coefficient lowers. Clearly, it would be best if a turbine can be operated at all wind speeds at a tip speed ratio close to that which gives the maximum power coefficient.

Conclusions

In the present work a simple and concise method for analysing a single horizontal axis wind turbine blade has been proposed by solving a set of 2D parallel equally spaced domains along the span. The code solves the discretised Navier-Stokes equations over a Cartesian domain via a Finite-volume numerical method. The main algorithm solves the discretised continuity and momentum coupled conservation equations simulating the fluid flow within a 2D domain built in a structured grid, with cancelled nodes that act like a solid immersed within the fluid. This solid can take any shape, including conventional airfoil profile geometries read from available data bases.

A fixed criteria on using central difference approximation for computing velocities and an implicit time integration scheme were developed in the study. The pressure coupling method used was the SIMPLE-Consistent algorithm. The scope is limited to a laminar compressible flow using low Reynolds numbers, so no turbulent situations are applicable, despite realistic Reynolds values for this kind of applications are clearly turbulent. An artificial interpolated boundary layer was proposed to solve specific boundary conditions at the frontier of the solid domain.

The code describes the velocities and pressure fields inside the fluid domain, which is of significance if the fluid behaviour past the airfoil. As mentioned before, outputs obtained at the monitor cells (control volumes adjacent to the immersed object) are first, tangential and normal vectors, therefore normal pressure and shear stress may be computed; obtaining finally lift and drag forces over the object. For this reason, despite the existence of different methods, the CFD model was used to calculate the effect on the blade airfoil. The blade sectioning method proposes a previous twist for its calculation, an optimal angle of attack computation and a domain size with a parameter selection.

Code validation was done by performing runs on internal and external flows over immersed basic geometry cylinders considering selected boundary and initial conditions. An essential aspect of the code was to include a measuring monitor that collects data outputs at the surface of the cylinder or airfoil of study. This monitor has two main functions, first to compute a vector information used later on to compute outputs such as aerodynamic forces and frequency patterns. A 3D blade may be analysed with some restrictions by sections along the blade span, and discarding interaction between them, throughout computing the aerodynamic forces exerted by the fluid motion over the surface of a 2D airfoil.

Our contribution consists on proposing a simple method to understand and analyse a rather complex problem. The most meritorious objectives achieved are: Properly located pressure distribution around the object, consistent flow separation points and an interpolated boundary layer near the object solid surface, although results are not as conclusive or definitive as we would hope since a number of conditions need to be fulfilled. The results are very sensitive to numerical parameters, like domain size and boundary conditions. We also found a large sensitivity to changes in profile and a dependency with respect to angles of attack, which result in changes in the coefficients of lift and drag as shown in the chapter 4. The profile NACA 0012 was analysed in somewhat further detail. Results show velocity and pressure for angles of attack from 0 to 30 degrees. A progressive increase of lift and drag coefficient at low Reynolds number $Re = 100$ were obtained, giving relatively high rates as a result, while maintaining a L/D ratio range reaching a peak before reaching 20 degrees and then reducing, as expected. The flow was validated with XFOIL results. We found a relatively good agreement between completely different methods. During analysis, constant wind speed and different Reynolds numbers were used, always under laminar regime. Optimum values for angles of attack were obtained, in which there was an increased lift coefficient and minimal drag, with a maximized L/D ratio.

In a general overview, results encourage further exploration and integration of further work to include other methods and formulations, but it is important to do so in a way that can be correlated with experimental results. It is very important in this context to obtain assessment and design tools for further airfoil evaluation in wind tunnels and real operating wind turbines. The following steps are recommended to incorporate turbulence models.

We may recommend future paths to follow in order to find a proper design or to confirm that the supplier's blades used at current wind turbine farms are correct:

- Apply improved and the most comprehensive numerical models to solve fluid problems over aerodynamic profiles considering turbulence effects.
- Build new codes to solve problems of flow around airfoils, using different approaches, like for instance panel or BEM.
- Build models to describe flow around three dimensional, rotating blades.
- Do experimental research to validate numerical models using prototypes.
- Close the gap in terms of design and analysis with current manufacturers and suppliers.

In any case we must keep in mind that the geometric design of the blade should be aimed to basic design parameters, including those mentioned in Chapter 1, and that the location of wind speed and the rotor diameter to airfoil geometry, angle of attack and tip speed ratio design. Likewise, the length of the chord and the twisting distribution must in order to achieve an optimal power performance be considered.

Bibliography

[1] Learn Engineering. http://www.learnengineering.org/2013/08/Wind-Turbine-Design.html. Accessed: 2014-02-04.

[2] cleantechnica. http://cleantechnica.com/2014/04/21/real-innovation-wind-energy/. Accessed: 2014-04-23.

[3] Gurit. Developer and innovator in the composites industry . http://www.gurit.com/wind-energy-handbook-1.aspx. Accessed: 2014-01-01.

[4] NASA Glenn Learning Technologies Project. http://www.grc.nasa.gov/WWW/k-12/airplane/ac.html.

[5] Pilotfriend. http://www.pilotfriend.com/. Accessed: 2014-04-21.

[6] UIUC Airfoil Data Site. http://illinois.edu/.

[7] Almohammadi, K., Ingham, D., Ma, L., and Pourkashan, M. Computational fluid dynamics (cfd) mesh independency techniques for a straight blade vertical axis wind turbine. *Energy*, –(58):483–493, July 2013. URL --.

[8] Almohammadi, K., Ingham, D., Ma, L., and Pourkashan, M. Modeling dynamic stall of a straight blade vertical axis. *Journal of fluids and structures*, –(57):144–158, July 2015. URL --.

[9] Anderson, J. D. *Fundamentals_of_Aerodynamics*. McGraw-Hill Higher Eduacation, third edition, 2001. ISBN 0-07-237335-0.

[10] Bai, C., Hsiao, F., Li, M., G.Y.Huang, and Chen, Y. Design of 10 kw hawt blade and aerodynamic investigation using numerical simulation. *Procedia Engineering*, –(67):8, – 2013. URL --.

[11] Bakker, A. Boundaty Layers and separation. Applied Computional Fluid Dynamics. Lecture 11. http://www.bakker.org/.

[12] Burton, T., Jenkins, N., Sharpe, D., and Bossanyi, E. *Wind Energy Handbook.* John Wiley and Sons, England, 2011.

[13] Chehouri, A., Younes, R., Ilinca, A., and Perron, J. Review of performance optimization techniques applied to wind turbines. *Applied Energy*, –(142):27, January 2015. URL --.

[14] Chowdhury, A., Akimoto, H., and Hara, Y. Vawt tilted condition cfd wake. *Renewable Energy*, –(85):327–337, July 2016. URL --.

[15] Drela, M. XFoil: Subsonic Airfoil Development System. MIT. http://web.mit.edu/drela/Public/web/xfoil/.

[16] Gera, B., Pavan, S. K., and Singh, R. Cfd analysis of 2d unsteady flow around a square cylinder. *International Journal of Applied Engineering Research, Dindigul*, 1(3): 602–610, ISSN-0976-4259 2010. URL --.

[17] Grasso, F. Usage of numerical optimization in wind turbine airfoil design. *Energy research Centre of the Netherlands at the 28th AIAA Applied Aerodynamics Conference*, –(AIAA-2010-4404):1–19, July 2010. URL --.

[18] Grasso, F. Hybrid optimization of wind turbine thick airfoils. *American Institute of Aeronautics and Astronautics, Inc at the 53rd AIAA/ASME/ASCE/AHS/ASC Structures, Structural Dynamics and Materials Conference*, –(AIAA-2012-1354):1–13, April 2012. URL --.

[19] Gundtoft, S. Wind turbines (design of an optimal rotor). *Fluid Dynamics (MIFLD1), Department of Mechanical Engineering at the University College of Arhus*, –(2nd Edition):1–31, May June 2009. URL `http://staff.iha.dk/sgt/Downloads/Turbines%20May4_2009_1.pdf`.

[20] Hansen, M. O. L. *Aerodynamics of Wind Turbines*. Earthscan, London, UK, 2008.

[21] Hau, E. *Wind Turbines. Fundamentals, Technolgies, Application, Economics*. Springer, Germany, 2006.

[22] Hoerner, S. Base drag and thick trailing edges. *Journal of the Aeronautical Sciences*, 17(10):622–628, – 1950. URL --.

[23] Houghton, E. L. and Carruthers, N. *Aerodynamics for Engineering students*. Edward Arnold Publishers Ltd, 41 Bedford square, London WCIB 3DQ, 1982.

[24] Ju, Y. and Zhang, C. Multi-point robust design optimization of wind turbine airfoil under geometric uncertainty. *Journal of Power and Energy*, –(–):–, – 2011. URL --.

[25] Kroo, I. and Alonso, J. AA 241 Aircraft Design: Synthesis and Analysis. http://adg.stanford.edu/aa241/airfoils/airfoilpressures.html.

[26] Kundu, P. and Cohen, I. *Fluid Mechanics*. Academic Press, edition, second edition, 2002. ISBN 0121782514. doi: 2001086884.

[27] Lanzafame, R., Mauro, S., and Messina, M. 2d cfd modeling of h-diarreus wind turbines using a transition turbulence model. *Energy Procedia*, –(45):131–140, – 2014. URL --.

[28] Lanzafame, R., Mauro, S., and Messina, M. 2d cfd modeling of h-diarreus wind turbines using a transition turbulence model. *Energy Procedia*, –(45):131–140, – 2014. URL --.

[29] Leveque, R. J. *Finite-Volume Methods for Hyperbolic Problems*. Cambridge University Press, The Pitt Building, Trumpington Street, Cambridge, United Kingdom, 2004.

[30] Li, Y., Paik, K., Xing, T., and Carrica, P. Dynamic overset cfd simulations of wind turbine aerodynamics. *Rewable energy*, –(37):285–298, – 2012. URL --.

[31] Lozano(MIT Professor), P. Fluid Mechanics and Aerodynamics, Lecture 3 Notes. http://web.mit.edu/16.unified/www/FALL/fluids/Lectures/f03.pdf.

[32] Manwell, J., McGowan, J., and Rogers, A. *Wind Energy Explained. Theory, Design and Application*. John Wiley and Sons Ltd,, England, 2002, 2003, 2008.

[33] M.Salinas-Vázquez, Vicente-Rodríguez, W., Chol-Orea, E., and García, V. L. Simulación de la turbulencia de un flujo que pasea alrededor de un cilindro de sección cuadrada a partir de la utilización de grandes escalas y de fronteras inmersas. *Revista Mexicana de Física*, 53(6):461–469, December 2007. URL `http://www.redalyc.org/articulo.oa?id=57053606`.

[34] M.Salinas-Vázquez, de la Lama, M. A., Vicente, W., and Martínez, E. Large eddy simulation of a flow through circular tube bundle. *Applied Mathematical Modelling*, 35 (4393-4406):4393–4406, March 2011. URL `www.elsevier.com/locate/apm`.

[35] Najar, F. and Harmain, G. A. Blade design and performance analysis of wind turbine. *International Journal of ChemTech Research*, 5(2):1054–1061, April-June 2013. URL `http://sphinxsai.com/2013/conf/PDFS%20ICGSEE%202013/CT=73%281054-1061%29ICGSEE.pdf`.

[36] Perumal, D. A., Kumar, G. V., and Dass, A. K. Numerical simulation of viscous flow over a square cylinder using lattice boltzmann method. *ISRN Mathematical Physics. International Scholarly Research Network*, 2012(Article ID 630801):1 – 16, Sept 2012. URL `http://www.hindawi.com/journals/isrn/2012/630801/ref/`.

[37] Prandtl, L. and Tietjens, O. G. *Fundamentals of Hydro- and Aerodynamics*. Cover Publications, Inc., 180 Varick St. New York, N.Y. 10014, 1934-1957.

[38] Schubel, P. J. and Crosley, R. J. Wind turbine blade design. *Energies*, 1073(3425–3449): 3425–3449, September 2012. URL `www.mdpi.com/journal/energies`.

[39] Silva, A. L. E., Silveira-Neto, A., and Damasceno, J. Numerical simulation of two-dimensional flows over a circular cylinder using the immersed boundary method. *Journal of Computational Physics*, 189(351–370):351–370, March 2003.

[40] Tangler, J. and Somers, D. *NREL Airfoil Families for HAWts.* National Renewable Energy Laboratory, 1617 Cole Boulevard, Godlen, Colorado, U.S.A., 1995.

[41] Timmer, W. and van Rooij, R. Summary of the delft university wind turbine dedicated airfoils. *American Institute of Aeronautics and Astronautics, Inc. and the American Society of MEchanical Engineers*, –(AIAA-2003-0352):1–11, – 2003. URL `--`.

[42] T.M.Lin, Soe, M., and Myo, W. Design and performance analysis on the airfoil shape of horizontal axis wind turbine. *International Journal of scientific engineering and technology research*, 03(11):1–6, June 2014. URL `--`.

[43] Versteeg, H. and Malalasekera, M. *An introduction to Computational Fluid Dynamics. The finite volume method.* Longman Scientific and Technical, England, 1995.

[44] Williamson, C. Vortex Dynamics in the Cylinder Wake. *Annual Review of Fluid Mechanics*, 28(1):477–539, 1996.

[45] Zhu, W., Shen, W., and Sørensen, J. Integrated airfoil and blade design method for large wind turbines. *Renewable Energy*, –(70):172–183, April 2014. URL `--`.